공학박사학위논문

돌풍을 고려한 유연항공기 비행역학에 관한 연구

A Study on Flexible Aircraft Flight Dynamics considering Gust

2017 년 8 월

서울대학교 대학원

기계항공공학부

김 시 호

Abstract

In recent years, staying aloft for extended periods of time, aircraft wing has become slender to meet the needs to be light and increase aerodynamic efficiency. Due to the wing with large aspect ratio, the flexible wings might be deformed even at trim. The aircraft flight dynamics and structure response is more affected by the gust which might occur during flight. In order to consider the coupled effect of flight dynamics and aircraft structure flexibility, floating frame of reference formulation is used to compose the flexible aircraft equations of motion. This aircraft structure model is combined with finite-state unsteady subsonic aerodynamics considering the control surfaces. The discrete gust model is incorporated into aerodynamic model.

The gust load is one of the unexpected natural phenomena that affects the aircraft flight dynamics. The gust load analysis is important process to evaluate aircraft flight performance and structure integrity. The quasi-static approach of the gust loads analysis is well established for the conventional aircraft to evaluate the increased load factor due to the gust. This approach is based on the assumptions and empirical data such as rigid-aircraft, level-flight, constant flight condition and critical gust length, so on. This approach enables low-fidelity calculations of the increased load factor without solving the equations of motion. In recent years, the aircraft wing has become slender to increase the aerodynamics efficiency. If the aircraft has slender wing, which can be deformed, the flight dynamics and the structure responses are more affected by the gust. Due to the aircraft flexibility, the quasi-static approach is not appropriate to evaluate gust load. To evaluate high-

fidelity calculation of the gust effect, the transient analysis might be performed. In this study, the transient analysis of the gust load using the six-degrees-of-freedom flexible aircraft is proposed and compared with the quasi-static approach. From the comparisons, it can be seen that the gust loads of transient approach is more precision than quasi-static approach. Moreover, the gust load under aircraft maneuvering, which cannot be analyzed quasi-static approach, can be evaluated through the proposed approach.

To evaluate the aircraft structure reliability and flight performance, the flight test simulations are performed. The flight test data is analyzed for the force estimations to improve the aircraft characteristics. The gust effect is one of the important sources in the force estimation. Therefore, gust effect needs to be considered along with the aerodynamic force, gravity and thrust. The gust generates the unexpected force which changes the flight path and structure responses from the nominal flight path. Two more aspects should be considered in the force estimation using the flight test data. First, the limitations on the equipment installation due to its location and weight restrict the amount of response data. Secondly, as the aircraft wing gets slender to increase the aerodynamic efficiency, the gust effect becomes complicated because of the coupled effect of flight dynamics and aircraft structure flexibility. In this study, we focus on the force estimation for the flexible aircraft by using optimization methods. Flexible aircraft analyses are performed with an aircraft model based on flexible multibody dynamics where a gust model is incorporated into the aerodynamic model. The limitations on the flight data are also considered in the model construction. The gust parameters, which generate the same response to the reference data, are identified in the optimization process.

For considering the many case of flight conditions, the computation time should be efficiency. Reduced order modeling (ROM) techniques have also been adapted to increase computational efficiency. The ROM based on proper orthogonal decomposition (POD) is presented. The computation time, on the other hand, might be reduced to 40~50% comparing to the full model analysis because reduced degrees-of-freedom (d.o.f) iteratively should be recovered to full d.o.f. The ROM which is based on POD is improved by using artificial neural network (NN). By constructing surrogate model, the iteratively recover process to calculate force matrix can be removed. The ROM with NN computation time is reduced to under 10% comparing the full analysis.

Key words: Flexible aircraft, Gust, Flexible multibody system dynamics, Optimization method, Reduced order model, Neural network

Student Number: 2014-31035

TABLE OF CONTENTS

LIST OF TABLES

LIST OF FIGURES

1. INTRODUCTION

The aircraft configuration is dependent upon the flight mission profile. One of the main features is wing aspect ratio. For the long endurance requirement of aircraft reads that aircraft is more light weight and wing is slender. These features not only improve the stability and endurance ability but also increase the demand of multidisciplinary analysis of the aircraft. During the flight, aircraft slender wing can be deformed by the aerodynamic forces and these phenomenon effect the aircraft trajectory which can change the flight trajectory and also the wing deformation sequentially. Which leads that the aircraft flexibility should be considered if the aircraft aspect ratio is high.

The unexpected load due to the gust is one of the important forces, because the gust can affect angle of attack, the wing deformation simultaneously. As aircraft wing is slender and the gross weight is lower, the gust effect is greater [1]. The gust load evaluation is important to investigate the aircraft structure integrity, controller design and so on. As they do in conventional aircraft design, gust response and maneuver loads drive the design of flexible aircraft structures, otherwise, conventional gust analysis is not suitable for slender wing aircraft. As the aircraft deformed configuration affects the flight state that may not be sufficiently analysis with quasi-static methods. For evaluating the gust effect during the flexible aircraft flight, first of all, the simulation model should be set up. This model might be contained the coupled effect of flight dynamics and aircraft structure flexibility and unsteady aerodynamic with control surface.

The force estimation is important to evaluate the aircraft structure reliability, flight performance and aircraft stability, etc. The flight test is the one of the way to evaluate these aircraft characteristics. The flight tests are planned to obtain operational intelligence data and evaluate the aerodynamic aircraft flight characteristics to validate the design, including safety aspects. Through the flight test, any design problems are found and fixed. If the force can be known during the flight, the aircraft design improvement can be achieved more suitably.

There are many cases of flight conditions such as aircraft velocity, altitude, attitude, maneuver, gust cases so on. For increasing analysis efficiency, the computation time should be reduced. Reduced order modeling techniques, which are well developed, have also been adapted for linear and nonlinear systems. Recently, an approximation or surrogate model is used for reduced computational time. Artificial neural networks (NNs) are a surrogate modeling approach and are trained to infer a nonlinear mapping from system input to system response, or output. In this study, the reduced order model is coupled with NN to increase the computation efficiency. Detail reviews of the flexible aircraft flight dynamics, force estimation based on invers problem theory and surrogate model are discussed in the following section.

1.1. Previous Work

1.1.1. Flexible Aircraft Flight Dynamics

The flexible aircraft flight dynamics can be categorized two field. One is the floating frame approach, the other is inertial frame approach. The floating frame

approach basis is rigid-body equations of motion and small deformation is considered. The Coriolis and centrifugal inertia force are included equations of motion. The floating frame approach has been widely applied to flexible structure analysis such as fluid–structure coupling, maneuvering flexible aircraft analysis and analyzing static aeroelasticity [2-5]. The inertial frame approach starts at continuum mechanics which can be considered large deformation. The inertia force is updated using intermediate frame. There has been increasing interest in the analysis of the flexible aircraft. Drela [6] developed an integrated model for aerodynamic, structural, control-law design and gust input. Cesnik et al. [7-14] introduced the nonlinear aeroelastic analysis based on the strain-based structural modeling with the finite state two-dimensional strip theory. They presented fully coupled six-degrees-of-freedom dynamics and trajectory control considering with the discrete gust and the skin winkling. Patil and Hodges [15] presented the nonlinear aeroelastic trim and stability for high-altitude long-endurance aircraft using geometrically exact intrinsic beam structural model [16, 17] with aerodynamic model [10]. Pedro and Bigg [18] presented the development and testing of a flexible aircraft and control system simulation facility in the MATLAB/SIMULINK.

All of these studies have contributed in different ways toward the understanding of the flight dynamics considering the aircraft flexibility, unsteady aerodynamics, control surface and/or gust. While these parallel efforts can be found in the attempt to analyze the response of the flexible aircraft, we present the integrated framework based on floating frame approach which is widely used for ground and space vehicles, mechanisms, robotics, space structures, and precision machines [19]. In

this study, the integrated approach is proposed which is based on the floating frame of reference formulation (FFRF) considering geometrically exact intrinsic beam structural analysis. The aerodynamics is the finite inflow theory considering control surface and '1-cosine' gust.

1.1.2. Force Identification based on Inverse Problem Theory

The force estimation through the response data is one of the inverse problem. Based on the response data, the force can be estimated directly or indirectly. There are some researches about the direct force estimation using force transduces for the dynamic force such as wind force, seismic action, impact force, and so on [20-23]. It is difficult to apply to aircraft because direct force estimation using force transducers can be inaccurate for force prediction due to the greatly change the structural characteristics. In the past decades, researchers were pursuing force reconstructed methods to accurately estimate dynamic loads because they could be derived from a relatively easy measurement of structural dynamic response.

Another method is indirect force estimation which use displacement, velocity or acceleration transducers to measure the structural response [24-26]. In the past decades, researchers were pursuing force reconstructed methods to accurately estimate dynamic loads because they could be derived from a relatively easy measurement of structural dynamic response. Kammer [27] presented a time domain method for reconstructing the discrete structural input force based on the measured structural response. Huang [28] applied the conjugate gradient method to estimate the time-dependent external forces in non-linear lumped-mass system using the displacement measuring system. Ma and Ho [29] developed an inverse

method, which is capable of identifying input forces for non-linear structural systems based on the extended Kalman filter and a recursive least-squares estimator. Especially, identifying aircraft aerodynamic loads by using strain data is proposed [30-33]. In those studies, by defining aerodynamic loads as specific function, the aerodynamic loads are estimated by determining the function coefficients. A lot of strain data is measured, yet there are measuring devices installation problem due to the location and weight limitations for flight test. The only limited device can be attached that leads the structure responses are insufficient.

The forces acting on the aircraft are aerodynamic force, gravity, thrust and unexpected force due to the gust. The gust changes the flight path and structure responses from the nominal flight path. To increase the aircraft endurance ability and flight stability, the aircraft wing becomes slender. This wing is deformed during the flight even at trim and increased the influence of the gust [34]. To estimate the force of the flexible aircraft considering the gust, firstly, the flight dynamic analysis for the flexible aircraft should be set up because the inverse method is based on the forward analysis [35].

1.1.3. Surrogate Model based on Neural Network

There are many application of neural network for various field [36]. Various types of NNs have been applied extensively for damage detection and, to a much lesser extent, for damage assessment [37-39]. Optimization based on surrogate-modeling have been studied[40, 41]. Real-time deformation of structure using finite element and neural networks in virtual reality applications [42].

NN application for aircraft is as follow. Pidaparti et al. [43] employed a NN to predict residual strength and corrosion rate of aging aircraft panels with collinear multisite damage by training with experimental results and validating with both experimental results and analytical solutions. Spear et al. [44] A surrogate-model methodology is described for real-time prediction of the residual strength of flight structures with discrete-source damage. Recent advances in neural network, direct adaptive flight control provide a foundation for much of this research [45-47]. Singh and Willcox [48] presented that on the setting of onboard measurements coupled with offline vehicle analysis information for the next generation of self-aware unmanned aerospace vehicles through together with machine learning and big data techniques.

The first step in this type of surrogate model development is typically referred to as design of experiment which is the sampling plan in design variable space[40]. The obtaining data points should be involved that will be used to train and test the NN. The design of experiment should be based on the intended application of the NN. Each data point includes sampled input variable(s) and corresponding known system response(s), called target output. Once the NN has been trained to map given input to target output, it becomes a useful tool for predicting system response when presented with new input that is within the training range, on the other hand, it does not necessarily correspond to data points used for training. In particular, a supervised NN is considered due to rapid prediction capabilities amenable to real-time applications.

1.2. Thesis Outline

The dissertation is organized as follows. Flexible aircraft six-degrees-of-freedom flight dynamics under gust are presented in chapter 2. The trim analysis and flight dynamics during maneuver are presented and compared to rigid aircraft. The uniform gust is modeled as discrete type which is based on Federal Aviation Regulations (FAR). The non-uniform gust is based uniform gust, the parameters which represent gust position, spatial shape and radius of gust are added. The gust effect is compared to flexible aircraft and rigid aircraft.

In chapter 3, evaluation of gust loads based on flexible aircraft transient analysis are compared to the quasi-static method which is basis for Federal Aviation Regulation Part 23. The quasi-static method is based on the assumptions such that aircraft is rigid, constant forward speed and cannot pitch during the gust range. This method provides low-fidelity results, but the computation time is small because those results can be obtained without solving the equation of motion. The quasi-static analysis results are compared to the presented flexible aircraft analysis results.

Chapter 4 presents the flight load reconstruction through the gust identification which is based on inverse problem theory. To evaluate aircraft structure integrity, the flight test are performed. From the flight, the limited structure responses can be obtained. In this chapter, the flight loads are reconstructed through the gust identified. The gust is identified using these limited responses based on the optimization process.

Chapter 5 introduces reduced order model using proper orthogonal decomposition (POD) method combined with surrogate model constructed by

neural network (NN). The analysis results based on POD are used to train the NN. The inputs are reduced structure responses and gust velocity for nodes. The outputs are forces which contains gravity, aerodynamics, thrust, gravity and the quadratic velocity vector. The NN is trained which activate function is sigmoid function. Finally, conclusions are provided in chapter 7.

Some applications based on this flexible aircraft analysis are presented in appendix. The flexible aircraft analysis is used for damaged aircraft and bomb loading. Due to the damage or bomb, the aircraft becomes asymmetric configuration. The responses are observed for these configurations.

2. FLEXIBLE AIRCRAFT FLIGHT DYNAMICS CONSIDERING GUST

The interaction between flight dynamics and aircraft flexibility, the flexible aircraft equations of motion include for six rigid-body motions and multiple flexible degrees of freedom. For modeling the aircraft, the floating frame of reference formulation (FFRF) is used which is the most widely used method in flexible multibody dynamics. The finite-state inflow theory is coupled with the aircraft equations of motion considering with the control surface. The discrete gust model which is mandated by the Federal Aviation Regulations is mounted to the aerodynamic model due to the simplicity and easiness of parameterization. The integrated framework is shown as Fig. 2.1. The overview of the formulations are described as follow including description of aircraft model.

2.1. Aircraft Model Description

A representative aircraft model is shown as Fig. 2.2. The three dimensional aircraft wings are converted to equivalent beam model by using commercial code VABS which is cross section analysis program for composite beam [49-51], and fuselage and tail wing are assumed as rigid body. The aircraft reference point is defined at between left and right wing which is near to the aircraft center of gravity. The main wing properties and aircraft properties are as shown in Table 2.1 and Table 2.2, respectively.

2.2. Formulation of Equations of Motion

2.2.1. Floating Frame of Reference Formulation

The flexible aircraft can be modeled as deformable body whose motion includes large displacement and rotation whether the wing deformation is not extremely large. The floating frame approach is a natural extension of existing rigid-body dynamics formulation to account for the effect of flexibility by superposition of the body structural dynamics on its possibly large overall motion [19]. The FFRF method is based on two sets of coordinates to describe the deformable bodies—body reference coordinate is used for the location and orientation of the deformable body and nodal elastic coordinates represent each the elements displacements. As body i is deformed Fig. 2.3, the global position vector of an arbitrary point P_i can be written as

$$\mathbf{r}_p^i = \mathbf{R}^i + \mathbf{A}^i\left(\overline{\mathbf{u}}_o^i + \overline{\mathbf{u}}_f^i\right) = \mathbf{R}^i + \mathbf{A}^i\left(\overline{\mathbf{u}}_o^i + \mathbf{S}^i\mathbf{q}_f^i\right) \tag{2.1}$$

where $\mathbf{R}^i$ is the translation of the body reference coordinate system with respect to the global coordinate system, and $\mathbf{A}^i$ is the transformation matrix, which is expressed here in terms of the Euler angle that is widely used in aerospace community. $\overline{\mathbf{u}}_o^i$ is the position of point P_i in the undeformed state, $\overline{\mathbf{u}}_f^i$ is the deformation vector. $\overline{\mathbf{u}}_f^i$ can be expressed in terms of shape function $\mathbf{S}^i$ and the vector of elastic coordinate $\mathbf{q}_f^i$.

Differentiating Eq. (2.1) with respect to time yields the velocity vector as follows,

$$\dot{\mathbf{r}}_p^i = \dot{\mathbf{R}}^i + \dot{\mathbf{A}}^i\overline{\mathbf{u}}^i + \mathbf{A}^i\mathbf{S}^i\dot{\mathbf{q}}_f^i \tag{2.2}$$

$$\dot{\mathbf{A}}^i\bar{\mathbf{u}}^i = \frac{\partial \mathbf{A}^i}{\partial \boldsymbol{\theta}}\frac{\partial \boldsymbol{\theta}}{\partial t}\bar{\mathbf{u}}^i = \frac{\partial\left(\mathbf{A}^i\bar{\mathbf{u}}^i\right)}{\partial \boldsymbol{\theta}}\frac{\partial \boldsymbol{\theta}}{\partial t} = \mathbf{B}\dot{\boldsymbol{\theta}} \tag{2.3}$$

$$\dot{\mathbf{r}}_p^i = \begin{bmatrix}\mathbf{I} & \mathbf{B} & \mathbf{AS}\end{bmatrix}\begin{bmatrix}\dot{\mathbf{R}}^i \\ \dot{\boldsymbol{\theta}}^i \\ \dot{\mathbf{q}}_f^i\end{bmatrix} = \mathbf{L}^i\dot{\mathbf{q}}^i \tag{2.4}$$

where $\dot{\boldsymbol{\theta}}^i$ is the first time-derivative of the Euler angle, and $\mathbf{q}^i$ is the total vector of the generalized coordinates of body i.

The following definition of the kinetic energy T^i and the mass matrix $\mathbf{M}^i$ is given as,

$$T^i = \frac{1}{2}\int_{V^i}\rho^i\dot{\mathbf{r}}^{iT}\dot{\mathbf{r}}^i dV^i = \frac{1}{2}\dot{\mathbf{q}}^{iT}\left[\int_{V^i}\rho^i\mathbf{L}^{iT}\mathbf{L}^i dV^i\right]\dot{\mathbf{q}}^i \tag{2.5}$$

$$\mathbf{M}^i = \int_{V^i}\rho^i\mathbf{L}^{iT}\mathbf{L}^i dV^i = \begin{bmatrix} m_{rr}^i & m_{r\theta}^i & m_{rf}^i \\ & m_{\theta\theta}^i & m_{\theta f}^i \\ sym. & & m_{ff}^i\end{bmatrix} \tag{2.6}$$

with

$$\begin{aligned} &m_{rr}^i = \mathbf{I}\int_{V^i}\rho^i dV^i; \quad m_{r\theta}^i = -\mathbf{A}^i\left[\int_{V^i}\rho^i\tilde{\bar{\mathbf{u}}}^i dV^i\right]\bar{\mathbf{G}}; \quad m_{rf}^i = \mathbf{A}^i\int_{V^i}\rho^i\mathbf{S}^i dV^i \\ &m_{r\theta}^i = \bar{\mathbf{G}}^{iT}\left[\int_{V^i}\rho^i\tilde{\bar{\mathbf{u}}}^{iT}\tilde{\bar{\mathbf{u}}}^i dV^i\right]\bar{\mathbf{G}}^i; \quad m_{\theta f}^i = \bar{\mathbf{G}}^{iT}\int_{V^i}\rho^i\tilde{\bar{\mathbf{u}}}^i\mathbf{S}^i dV^i; \quad m_{ff}^i = \int_{V^i}\rho^i\mathbf{S}^{iT}\mathbf{S}^i dV^i \end{aligned} \tag{2.7}$$

The generalized forces are associated with the elastic forces arising from the body deformation and externally applied forces. The virtual work due to the elastic forces can be written as

$$\delta W_s^i = -\int_{V^i}\boldsymbol{\sigma}^{iT}\delta\boldsymbol{\varepsilon}^i dV^i = -\mathbf{q}_f^{iT}\mathbf{K}_{ff}^i\delta\mathbf{q}_f^i \tag{2.8}$$

$$\mathbf{K}_{ff}^i = \int_{V^i}\left(\mathbf{D}^i\mathbf{S}^i\right)^T\mathbf{E}^i\left(\mathbf{D}^i\mathbf{S}^i\right)dV^i \tag{2.9}$$

where $\boldsymbol{\sigma}^i$ and $\boldsymbol{\varepsilon}^i$ are, respectively, the stress and strain vector. $\mathbf{D}^i$ is a differential operator, $\mathbf{E}^i$ is the matrix of elastic coefficients, and $\mathbf{K}_{ff}^i$ is the

stiffness matrix. From the above equations, we can rewrite the equation for generalized coordinates

$$\delta W_s^i = -\mathbf{q}^{i^T} \mathbf{K}^i \delta \dot{\mathbf{q}}^i \tag{2.10}$$

The virtual work due to the external forces can be written as,

$$\delta W_e^i = \mathbf{F}^{i^T} \delta \mathbf{r}_p^i = \mathbf{Q}_e^{i^T} \delta \mathbf{q}^i \tag{2.11}$$

$$\mathbf{Q}_e^i = \mathbf{F}^{i^T} \mathbf{L}^i \tag{2.12}$$

where $\mathbf{Q}_e^i$ is the vector of the generalized forces associated with the *i*-th body generalized coordinates. This term contains gravity, thrust and aerodynamics.

We write the virtual work of the forces acting on body *i* as

$$\delta W^i = \delta W_s^i + \delta W_e^i = -\mathbf{q}^{i^T} \mathbf{K}^i \delta \dot{\mathbf{q}}^i + \mathbf{Q}_e^{i^T} \delta \mathbf{q}^i \tag{2.13}$$

$$\mathbf{Q}^i = -\mathbf{K}^i \mathbf{q}^i + \mathbf{Q}_e^i \tag{2.14}$$

The Lagrange's equation takes the form using Eq. (2.5) and Eq. (2.14)

$$\frac{d}{dt}\left(\frac{\partial T^i}{\partial \dot{\mathbf{q}}^i}\right)^T - \left(\frac{\partial T^i}{\partial \mathbf{q}^i}\right)^T = \mathbf{Q}^i \tag{2.15}$$

$$\mathbf{M}^i \ddot{\mathbf{q}}^i + \mathbf{K}^i \mathbf{q}^i = \mathbf{Q}_e^i + \mathbf{Q}_v^i \tag{2.16}$$

$$\mathbf{Q}_v^i = -\dot{\mathbf{M}}^i \dot{\mathbf{q}}^i + \left[\frac{\partial}{\partial \mathbf{q}^i}\left(\frac{1}{2}\dot{\mathbf{q}}^{i^T} \mathbf{M}^i \dot{\mathbf{q}}^i\right)\right]^T \tag{2.17}$$

where $\mathbf{Q}_v^i$ is a quadratic velocity vector resulting from partial derivatives of the kinetic energy of the body. This term represents the gyroscopic and Coriolis force. The more details about $\mathbf{Q}_v^i$ are presented Appendix. A. We do not consider the specific displacement constraints because the flexible aircraft flight is in the free-free condition and it has no storage attached. If some storage—fuel tank, armor and so on—is mounted, the constraint can be introduced through Lagrange multipliers.

2.2.2. Aerodynamics

The aerodynamic loads in this study are based on the finite state aerodynamic theory [9-11]. The theory calculate loads on a thin airfoil section undergoing in inviscid and incompressible subsonic flow. Although flexible aircraft might have the potential to flight at high altitude in which compressibility and Reynolds number are important, those effects are not considered in this work. The lift and moment about the beam reference line are expressed as,

$$L^{aero} = 2\pi\rho b\left(-\dot{y}\dot{z} + (b-d)\dot{y}\dot{\alpha} - \dot{y}\lambda_0 - \frac{1}{2}b\ddot{z} - \frac{1}{2}bd\ddot{\alpha} \right) \tag{2.17}$$

$$D^{aero} = 2\pi\rho b\left(\dot{z}^2 + d^2\dot{\alpha}^2 + \lambda_0^2 + 2d\dot{\alpha}\dot{z} + 2\lambda_0\dot{z} + 2d\dot{\alpha}\lambda_0 \right) \tag{2.18}$$

$$M^{aero} = dL^{aero} + 2\pi\rho b^2\left(-\frac{1}{2}\dot{y}\dot{z} - \frac{1}{2}d\dot{y}\dot{\alpha} - \frac{1}{2}\dot{y}\lambda_0 - \frac{1}{16}b^2\ddot{\alpha} \right) \tag{2.19}$$

where b is the semi-chord, d is the distance of the mid-chord in front of the reference axis, and λ_0 is the induced flow due to free velocity. α is the local angle of attack and $\dot{y}$, $\dot{z}$ are the velocity vector component along the chord, respectively.

Additional aerodynamic lift ad moment are calculated by discrete trailing-edge surface deflection.

$$L^{\delta} = 2\pi\rho b\left(c_1\dot{y}^2\delta_u + c_2\dot{y}\dot{\delta}_u + c_3\ddot{\delta}_u \right) \tag{2.20}$$

$$D^{\delta} = 2\pi\rho b\left(c_1\beta\dot{y}\dot{z} + (dc_1 + bg_2)\beta\dot{y}\dot{\alpha} + c_1\beta\dot{y}\lambda_0 + \frac{1}{2}bg_2\beta\ddot{z} + \left(\frac{1}{2}bdg_2 - \frac{1}{4}b^2g_3\right)\beta\ddot{\alpha} \right) \tag{2.21}$$

$$M^{\delta} = 2\pi\rho b\left(d\left(c_1\dot{y}^2\delta_u + c_2\dot{y}\dot{\delta}_u + c_3\ddot{\delta}_u\right) + b\left(c_4\dot{y}^2\delta_u + c_5\dot{y}\dot{\delta}_u + c_6\ddot{\delta}_u\right)\right) \tag{2.22}$$

The coefficients c_1 through c_6 are based on the geometry and the details are given in [9, 11]. In this work, only the deflection term δ_u is considered because the deflection rate terms $\dot{\delta}_u$ and $\ddot{\delta}_u$ are much smaller than the magnitude of the deflection term. Further details on the aerodynamics can be found in [9-11]. The aerodynamic center will be transferred to the reference frame for the solution of equations of motion.

2.2.3. Discrete Gust Model

The discrete gust is based on the '1-cosine' gust model [34, 52] whose shape is symmetric. The equation of the discrete uniform gust velocity is given as,

$$U = \frac{U_{ds}}{2}\left[1-\cos\left(\frac{\pi s}{H}\right)\right] \qquad for\ \ 0 \le s \le 2H \tag{2.23}$$

where U is a gust velocity, U_{ds} is the design gust velocity in equivalent air speed, s is the distance penetrated into the gust and H is the gust gradient which is the peak gust velocity, respectively. The design gust velocity is expressed as

$$U_{ds} = U_{ref} F_g \left(H/350\right)^{1/6} \tag{2.24}$$

where U_{ref} is the reference gust velocity which depends on the altitude and F_g is the flight profile alleviation factor. We model the gust by using the gust gradient H and the flight profile alleviation factor F_g. Fig. 2.4 is the gust profile, the gust velocity is a function of distance. As the flight speed is higher, flight time under the gust is shorter. In this work, we call the gust gradient H and the flight profile alleviation factor F_g as discrete uniform gust parameters.

One of the non-uniform discrete gust model which is dependent of both space and time is presented [14]. The non-uniform discrete gust center velocity is defined using the '1-cosine' gust. The center velocity is as same as the uniform gust velocity. The gust shape is defined by using gust range, chord-wise (north direction) and span-wise (east direction) directional amplitude parameters. So, the shape of non-uniform discrete gust region is defined as a circular one and the gust center velocity reaches the maximum and reduces to zero at the boundary. The equation of the non-uniform discrete gust are

$$A(r,\eta,s)=\frac{U_{ds}}{2}\left[1-\cos\left(\frac{\pi s}{H}\right)\right]\sqrt{\left(A_E\cos\eta\right)^2+\left(A_N\sin\eta\right)^2} \tag{2.25}$$

$$\begin{aligned} A_E(r)&=\sin\left(\frac{\pi}{2}\left[1-\left(\frac{r}{r_0}\right)^{n_E}\right]\right), \quad 0<r\le r_0 \\ A_N(r)&=\sin\left(\frac{\pi}{2}\left[1-\left(\frac{r}{r_0}\right)^{n_N}\right]\right), \quad 0<r\le r_0 \end{aligned} \tag{2.26}$$

where U_{ds} is the gust velocity at the center which is defined as previous eq. (2.24). The footnotes E and N are east and north directions, respectively. r_0 is the radius of the gust region. n_E and n_N are adjusting the gust spatial distribution parameters along the east and north direction, respectively. η is the orientation angle of the specific point with respect to the east direction and r is the distance from the gust center to the specific point. The gust velocity can be defined numerously at same location. So, in this work, we modified this model using only span-wise velocity. This modified model velocity at center is same as that of the original model and the other location gust velocity is as same as the original model maximum gust velocity at each location. The gust velocity at each

point is defined as specific value. We defined one more parameter related on the gust position from the aircraft center. The gust center position parameter G_p is used to define the non-uniform gust center position from aircraft center shown as Fig. 2.5.

In this study, we use five parameters as non-uniform gust parameters as the gust gradient H and the flight profile alleviation factor F_g which are same as uniform gust. The radius of the gust region r_0, span-wise adjusting gust spatial distribution parameters n_E and the gust center position parameter G_p. Fig. 2.6. shows the example of non-uniform discrete gust profile and modified one of which parameters are $U_{ds} = 10\,\text{m/s}$, $r_0 = 10\,\text{m}$, $n_E = 1$, $n_N = 2$, $H = 50m$, $G_p = 10m$.

2.3. Flexible Aircraft Trim Analysis

One of the Pratt method assumptions is that the aircraft enters into the gust at steady level flight. We determined the trim parameters considering the wing flexibility by using the optimization method. Trim analysis is performed using optimization process as described Fig. 2.7., based upon the method outlined in [53, 54]. We optimized the three trim parameters—the ruddervator angle d_e, throttle setting d_T, and the body angle f which is related on angle of attack.

We defined the cost function as

$$J_{trim} = \sum_{i=1}^{3} \left(F_i^2 + M_i^2 \right), \quad \text{(at reference point)} \tag{2.27}$$

The cost function J_{trim} is minimized using three trim parameters. The trim parameter optimization problem is described below:

$$
\begin{aligned}
&\text{minimize} && J_{trim} \\
&\text{with respect to} && \delta_e,\ \delta_T,\ \phi \\
&\text{subject to} && -45° \le \delta_e \le 45° \\
& && 0 \le \delta_T \le 1 \\
& && -30° \le \phi \le 30°
\end{aligned}
\tag{2.28}
$$

The cost function is also affected by the wing deformation which generates the aerodynamic force change and gravity. We conducted this process twice at each step using bisection method. First, we obtained trim parameter at the previous deformed shape. Using this parameter, the force and moment is applied to the aircraft structure to calculate the deformation which change the force and moment again. By considering the deformation, we conducted second trim parameter optimization process using the deformed aircraft shape. This process is conducted until the cost function J_{trim} is minimized under the tolerance. The flight conditions are that the aircraft velocities are 70, 75 and 80 m/s and the altitude is 10,000m. The optimized trim parameters for rigid aircraft and flexible aircraft are shown Table 2.3. As the aircraft velocity is increased, the parameters are decreased because the gravity is same otherwise the aerodynamic force due to the velocity is increased. That leads to decrease the body angle and ruddervator angle. The flexible aircraft body angle and the ruddervator angle are less than those of rigid aircraft it because the deformation leads to increase aerodynamic force. Fig.2.8. shows the wing tip deformation for each aircraft velocity. As increase the aircraft velocity affect the aerodynamic force that leads the affection of the aerodynamic force due to the deformation is decreased which leads that the wing deformation is decreased.

2.4. Flight Dynamics during Maneuver

When the control surface is operated, the additional load is generated which changes the aircraft flight state. Fig.2.9. shows the trajectory the trim, pitch-up and pitch-down varying ruddervator control surface for flexible and rigid aircraft. The aircraft flight altitude is 10,000m and velocity is 75m/s. Control surface is operated trim state ± 0.5 degree. During the flight the thrust is maintained as initial value. As the aircraft is pitch-up, the altitude and attitude are increasing, the velocity is decreasing. As apex is reached and the aircraft begins a dive because of the loss of life from insufficient airspeed. As the aircraft is pitch-down, otherwise, the altitude and attitude is decreased and velocity is increased. However, flexible aircraft and rigid aircraft have different structural responses. Flexible aircraft change altitude more than rigid aircraft. This is due to the aerodynamic changes caused by the deformation of the flexible aircraft. R/H wing tip deflection is changed as flight condition varying. When the aircraft is pitch-up, the aircraft is affected more lift due to the angle of attack increasing. The wing tip deflection is increased more than trim state. When the aircraft is pitch-down, the angle of attack is decreased and the wing tip deflection is decreased. Fig.2.10. shows the trajectory the trim and left turn varying aileron ±0.5 degree. Left and right aileron gear ratio is one to minus one. Flexible aircraft have different left and right wing deformation, and due to the difference in aerodynamics, they have different structural response from rigid aircraft. The altitude change of a flexible aircraft is larger than that of a rigid aircraft, while lateral movement is less.

2.5. Flight Dynamics under Discrete Gust

Three types of uniform gusts were applied as shown in Fig.2.11 for flexible aircraft flight dynamics depending on the magnitude of gust gradient. The aircraft is flying at 75 m/s in a trim state, and gusts are acting vertically. As the larger the size of the gust, the greater the effect on the aircraft flight path and the displacement of the right wing tip is less changed. On contrast, the smaller the magnitude of the gust, the less the altitude change is, but the instantaneous load is applied to the wing and the displacement is large. For flexible aircraft flight dynamics with respect to the same gust, the aircraft velocities are 70, 75 and 80 m/s as Fig.2.12. For the same gusts, the lower the aircraft speed, the greater the altitude change, and the larger the aircraft speed, the greater the instantaneous load on the wing and the greater the displacement of the right wing tip.

As mentioned in the previous section, the modified non-uniform discrete gust is modeled using five parameters. To compare the flight dynamics with gust between flexible and rigid aircraft, the gust is modeled with the following parameters: $H = 50\text{m},\ F_g = 0.8,\ r_0 = 12\text{m},\ n_E = 2,\ G_p = 10\text{m}$. The gust is located at the right side of the aircraft as shown in Fig. 2.13. The maximum gust velocity is about 3.74m/s and the aircraft enters into the gust at the trim condition. Fig.2.14 the trajectory of flexible and rigid aircraft. The both aircrafts turn to the left due to the increased lift at right wing, yet the flexible aircraft trajectory change is less than the rigid aircraft. The flexible aircraft goes less to the left than that of rigid aircraft. Fig.2.15 shows the structural response at the reference axis shown Fig.2.2. The flexible and rigid aircraft turn left due to the increased local lift at the right wing that generates the roll and yaw moment. The flexible aircraft position and altitude are lower than

those of the rigid aircraft because the deformable wing of the flexible aircraft generates more aerodynamic force than rigid aircraft which affect the aircraft stability. The flexible aircraft R/H wing is affected by the gust, and the wing tip is deformed as the lift increased. Comparing the trim condition, the flexible aircraft attitude varies less than the rigid aircraft. To evaluate the non-uniform gust maximum velocity effect for the flexible aircraft, the gust is modeled as three case using the alleviation factor of 1.0, 0.8 and 0.6, respectively. The other gust parameter is same as following: $H = 50\text{m},\ r_0 = 12\text{m},\ n_E = 2,\ G_p = 10\text{m}$. On the other hand, the gust model location is same. The gust shape is as Fig.2.16. The maximum gust velocity is 4.68m/s, 3.74m/s and 2.09m/s, respectively. Fig.2.17. and Fig.2.18. show the flight path and dynamic response. As the gust maximum velocity increased, the aircraft goes turn left due to the increased lift at right wing which generates roll and yaw moment. Fig.2.19 shows the flight dynamic results with three gust positions which have the identical shape. The gust parameters are as following: $H = 50\text{m},\ F_g = 0.8,\ r_0 = 12\text{m},\ n_E = 2$. The gust positions from the center of the aircraft are three cases of 5m, 10m and 15m. As shown Fig.2.20 and 2.21, if the gust position is at 5m, gust affects both wing more than the other cases, so that the altitude is varying higher than the other cases during the gust range. The gust affect to change the aircraft pitch while the tip deflection is less than the other cases. If the gust position is at 15m, the gust is located only at the right wing. This make the wing tip deformation become higher than the other case while the aircraft trajectory and attitude variations be smaller than the other cases. When the gust is located at 10m, the aircraft position variation is more than the other cases because the gust affects right wing deformation and the aircraft flight dynamics.

From these results, it should be noted that the flexible aircraft response is different from that of rigid aircraft due to the wing deformation. In addition, we observed the gust effect changing the gust parameters. The gust shape and position are important to evaluate the gust effect.

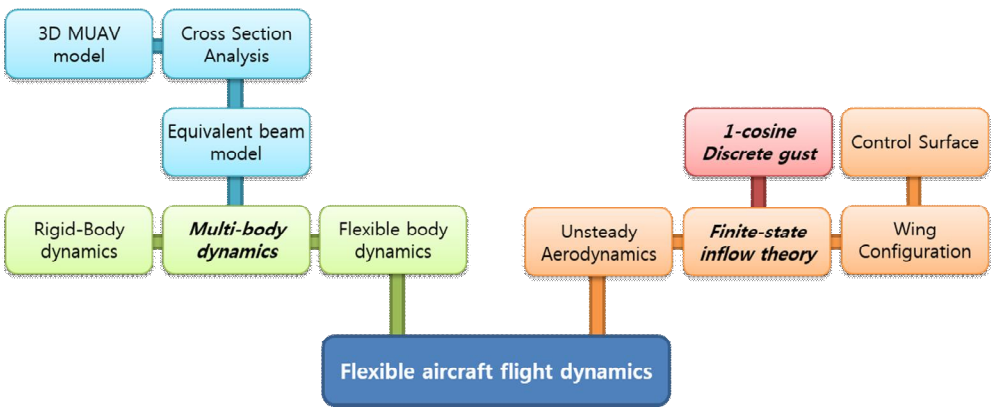

Figure 2.1. Integrated framework for flexible aircraft transient analysis

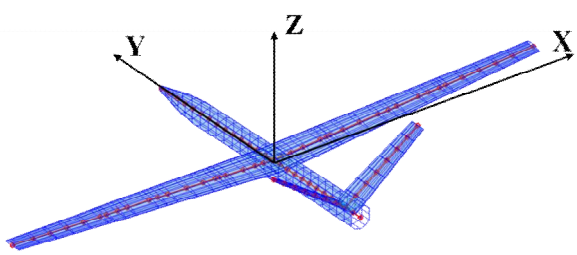

Figure 2.2. Equivalent aircraft model and defined reference axis

Table 2.1. Main wing stiffness properties

Property	Wing root	Wing tip	Units
EA	1.29×10^9	1.24×10^8	$N \cdot m^2$
GJ(torsional rigidity)	2.62×10^7	5.43×10^5	$N \cdot m^2$
EI_{22} (flatwise bending rigidity)	3.29×10^7	5.67×10^5	$N \cdot m^2$
EI_{33} (chordwise bending rigidity)	1.53×10^8	2.79×10^6	$N \cdot m^2$

Table 2.2. Representative flexible aircraft properties

property	Value	Units
Total mass	4.85×10^3	kg
Mass moment of inertia (torsional)	3.48×10^4	kg·m
Mass moment of inertia (flatwise bend.)	3.98×10^4	kg·m
Mass moment of inertia (chordwise bend.)	7.36×10^4	kg·m
Fuselage length	13.32	m
Wing span	25.3	m
Wing incidence angle	4	deg.
Tail wing span	2.92	m
Tail wing incidence angle	35	deg.
Aileron span location	6.4	m
Aileron length	5.86	m
Ruddervator span location	0.93	m
Ruddervator length	2.64	m
Element per wing	21	
Element per tail wing	8	
Element per fuselage	27	
Total number of element	80	

* The moment of inertia is based on the undeformed aircraft configuration.

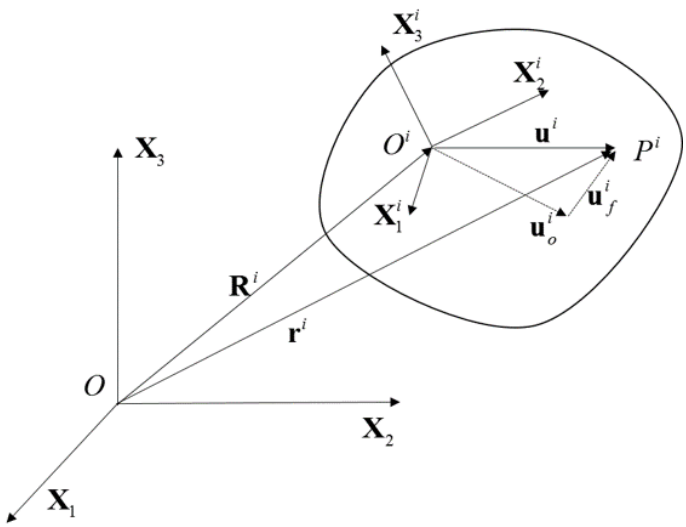

Figure 2.3. Coordinates of deformable bodies

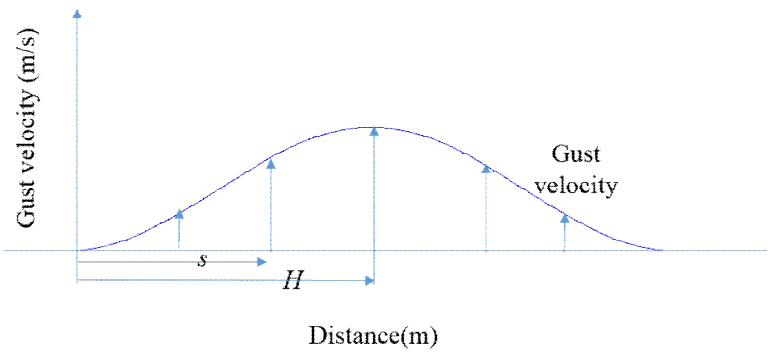

Figure 2.4. Discrete gust profile

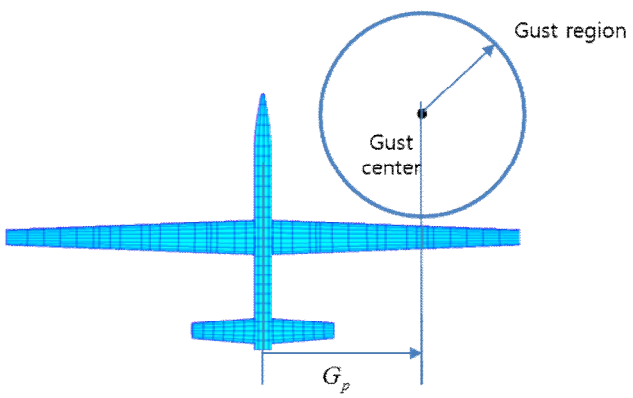

Figure 2.5. Non-uniform discrete gust center position

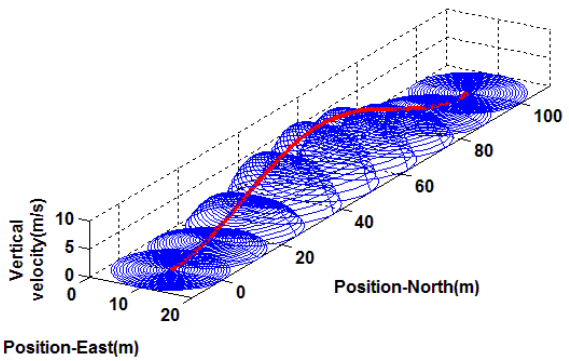

$U_{ds} = 10\,\text{m/s},\ r_0 = 10\,\text{m},\ n_E = 1,\ n_N = 2,\ H = 50m,\ G_p = 10m$

(a) Non-uniform gust profile

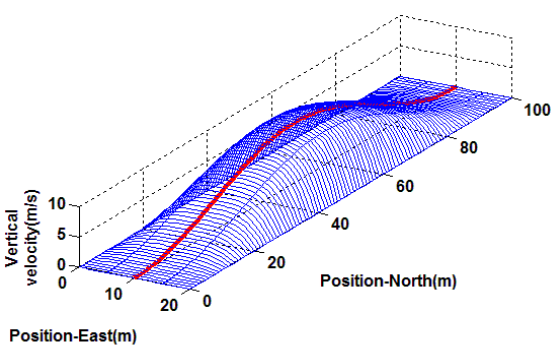

$U_{ds} = 10\,\text{m/s},\ r_0 = 10\,\text{m},\ n_E = 1,\ H = 50m,\ G_p = 10m$

(b) Modified non-uniform gust profile

Figure 2.6. Non-uniform discrete gust profile

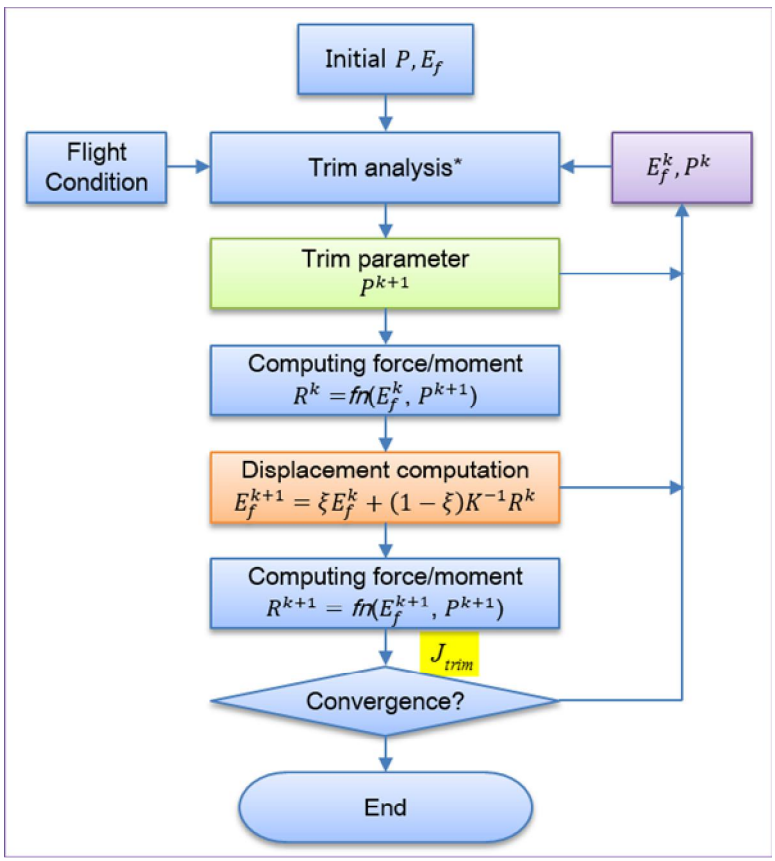

Figure 2.7. Flexible aircraft trim analysis process

Table 2.3. Optimized trim parameter

Parameter	Rigid aircraft (A)			Flexible aircraft (B)			Difference (A-B)		
	70m/s	75m/s	80m/s	70m/s	75m/s	80m/s	70m/s	75m/s	80m/s
ϕ (degree)	7.2356	5.3573	3.8190	7.2016	5.3324	3.8050	0.0341	0.0249	0.0141
δ_e (degree)	-2.6357	-1.8203	-1.1524	-2.4638	-1.6694	-1.0236	-0.1719	-0.1508	-0.1288
δ_T (N)	6543.9	4908.6	3532.7	6554.4	4905.0	3522.4	-10.5	3.6	10.3

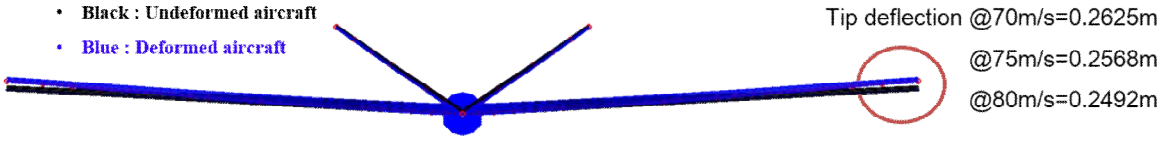

Figure 2.8. Trim state about rigid and flexible aircraft

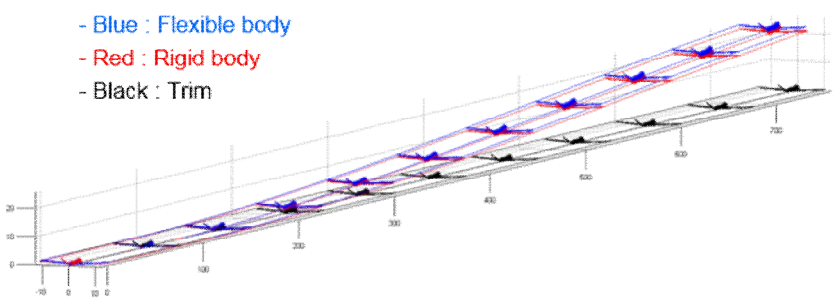

(a) Pitch-up trajectory

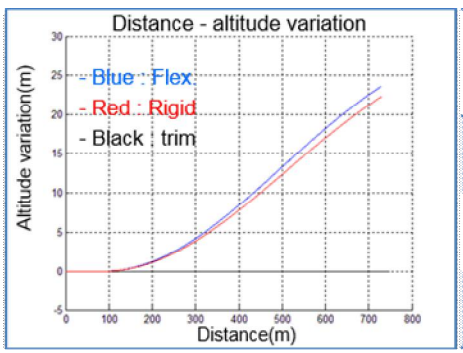

Flight condition	Altitude Variation(m)	Distance(m)
Flexible	23.6440	729.6961
Rigid	22.3710	731.0959
Trim	0	750.0000

(b) Pitch-up response

Figure 2.9. Flexible aircraft response under ruddervator control surface input (continued)

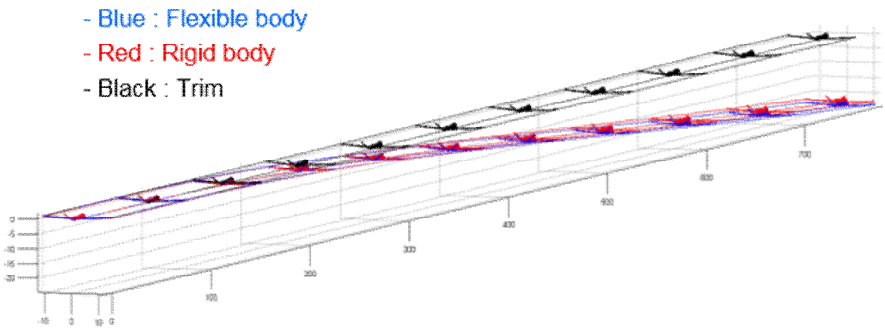

(c) Pitch-down trajectory

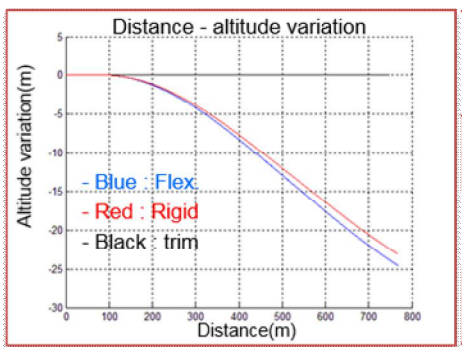

Flight condition	Altitude Variation(m)	Distance(m)
Flexible	-24.6163	769.8348
Rigid	-23.1063	768.4618
Trim	0	750.0000

(d) Pitch-down response

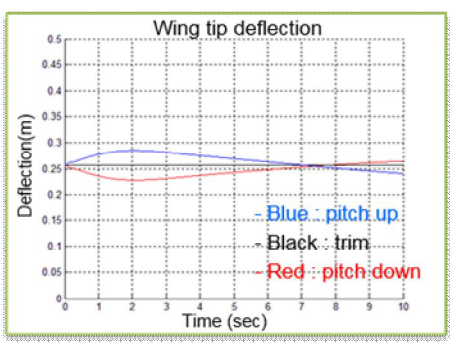

Flight condition	Max. Deflection(m)	Min. Deflection(m)
Pitch-up	0.2852	0.2406
Trim	0.2568	0.2568
Pitch-down	0.2645	0.2277

(e) R/H wing tip deflection

Figure 2.9. Flexible aircraft response under ruddervator control surface input

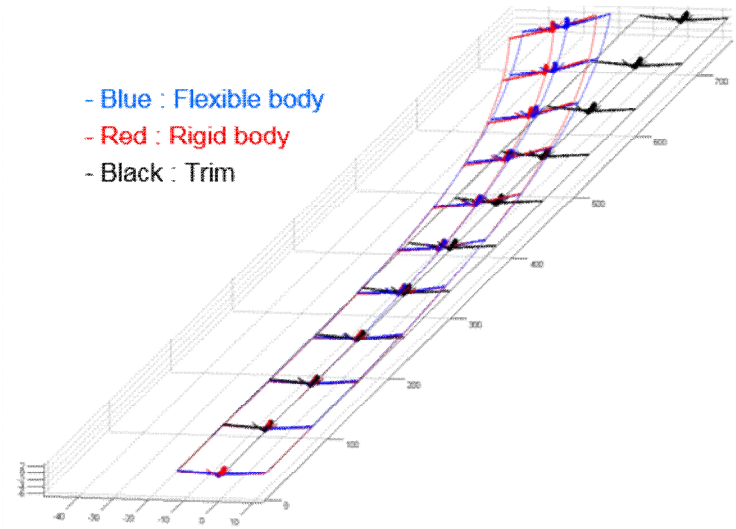

(a) Left-turn trajectory

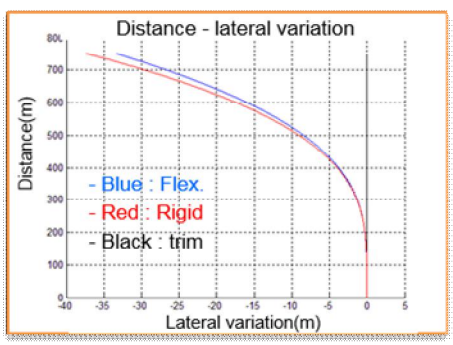

Flight condition	Lateral Variation(m)	Altitude Variation(m)
Flexible	-33.4444	-2.8156
Rigid	-37.4702	-2.6929
Trim	0	0

(b) Left-turn response

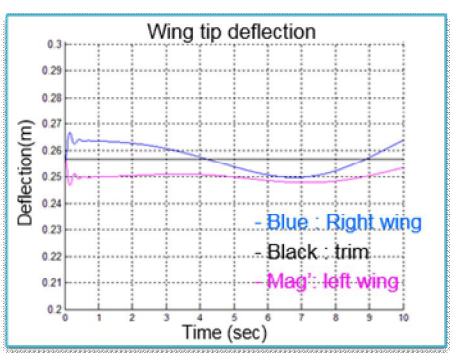

Flight condition	Max. Deflection(m)	Min. Deflection(m)
Right wing	0.2568	0.2467
Trim	0.2568	0.2568
Left wing	0.2669	0.2509

(c) Main wing tip deflection

Figure 2.10. Flexible aircraft response under aileron control surface input

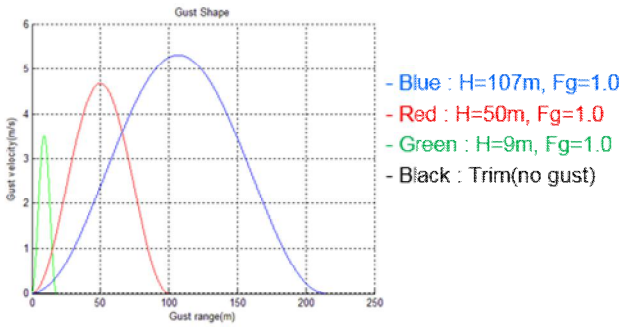

(a) Gust shape

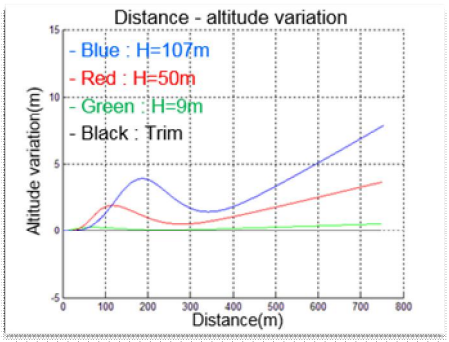

(b) Distance-altitude variation

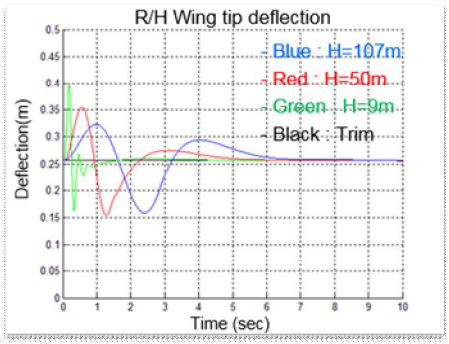

(c) R/H wing tip deflection

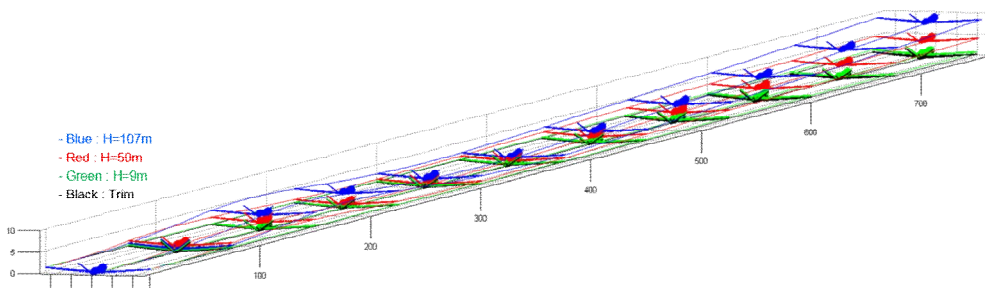

(d) Trajectory

Figure 2.11. Flexible aircraft response varying uniform gust gradient gust

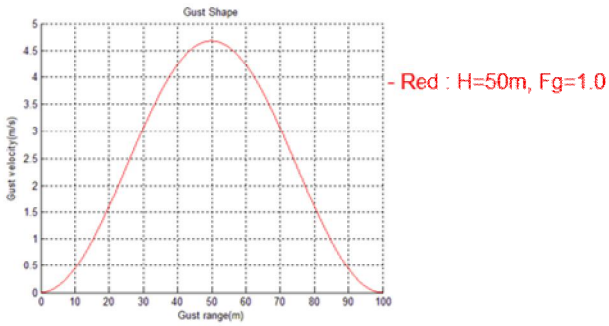

(a) Gust shape

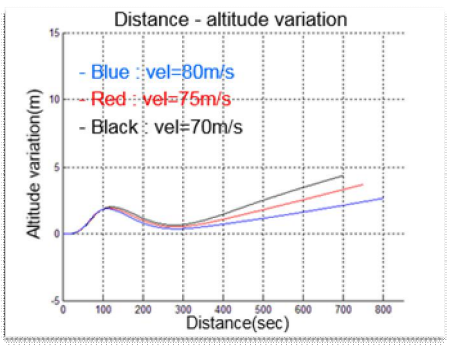

(b) Distance-altitude variation

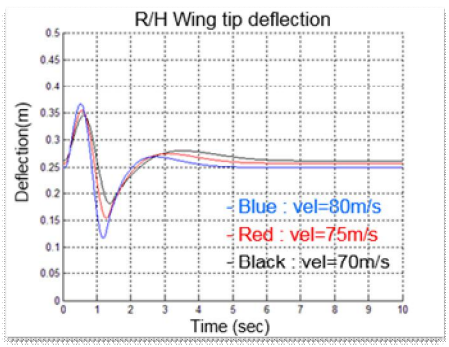

(c) R/H wing tip deflection

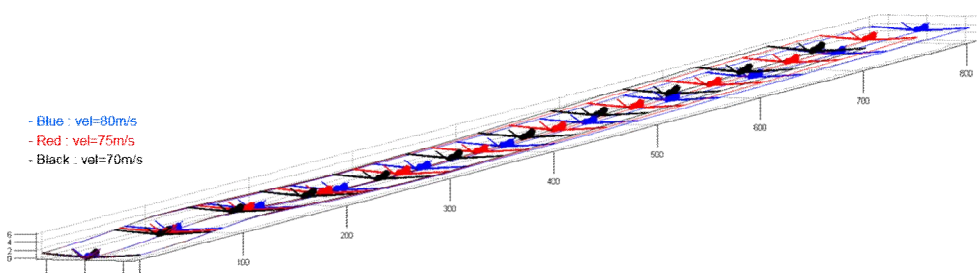

(d) Trajectory

Figure 2.12. Flexible aircraft response varying aircraft velocity

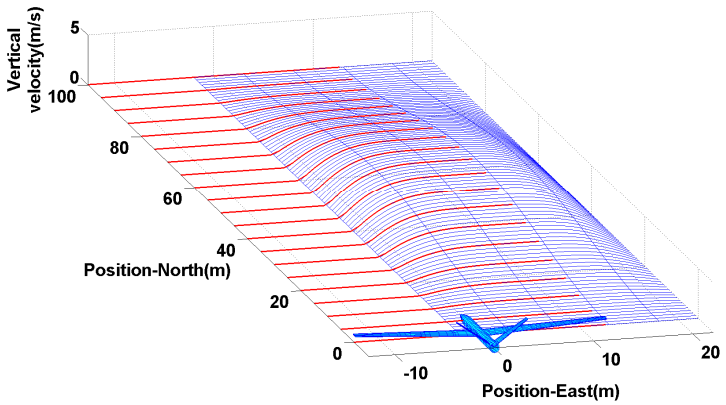

Figure 2.13. Non-uniform discrete gust distribution

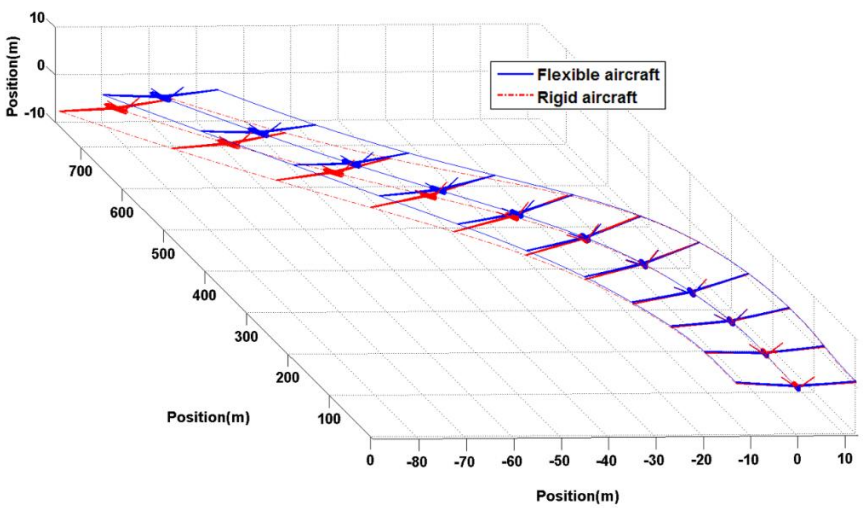

Figure 2.14. Trajectory of flexible and rigid aircraft

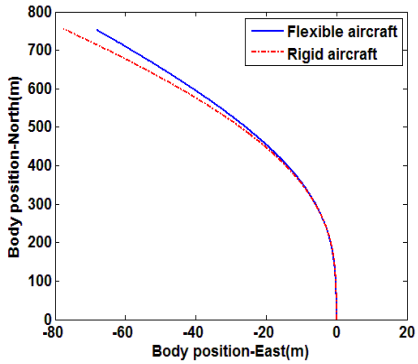

(a) Aircraft lateral and longitudinal position

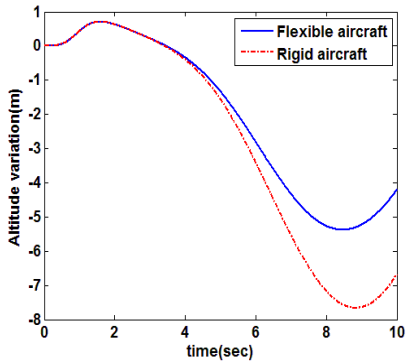

(b) Altitude variation

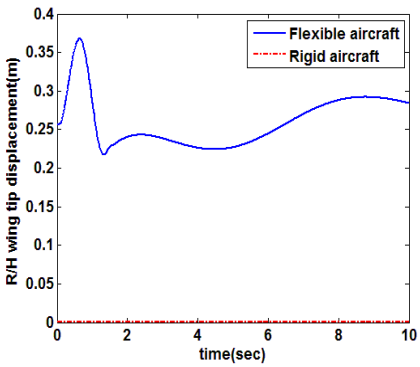

(c) R/H wing tip deflection

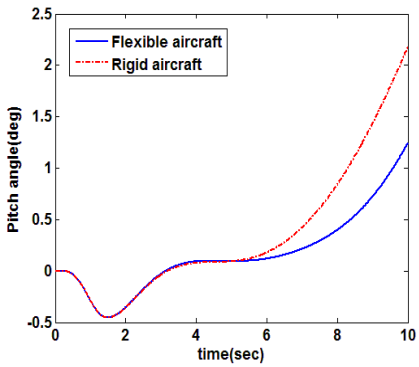

(d) Aircraft pitch angle variation

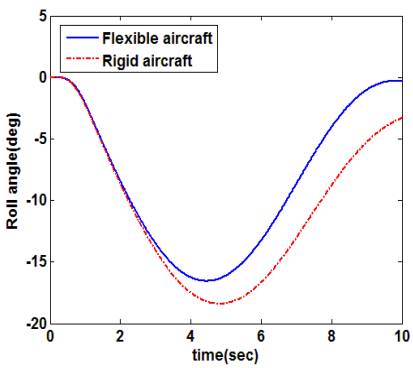

(e) Aircraft roll angle variation

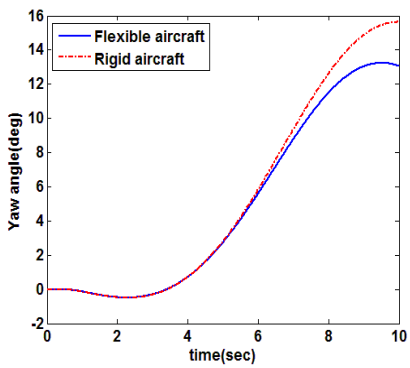

(f) Aircraft yaw angle variation

Figure 2.15. Flight dynamic response for flexible aircraft and rigid aircraft

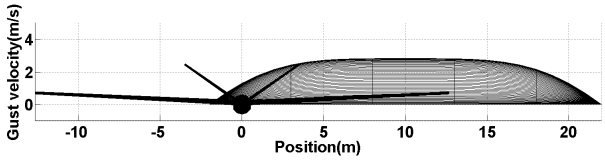

(a) Gust alleviation factor is 0.6

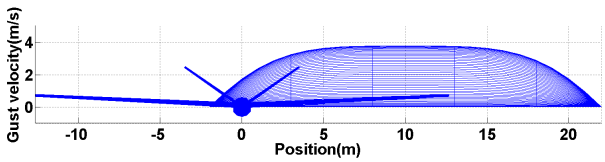

(b) Gust alleviation factor is 0.8

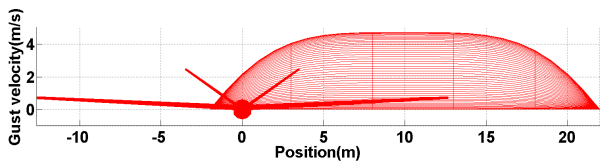

(c) Gust alleviation factor is 1.0

* $H = 50\text{m},\ r_0 = 12\text{m},\ n_E = 2,\ G_p = 10\text{m}$

Figure 2.16. Gust shape varying gust alleviation factor

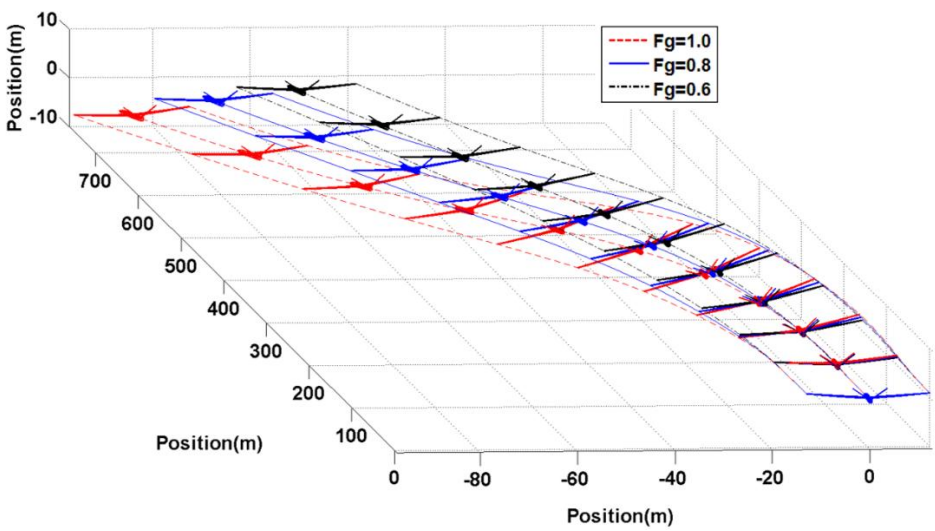

Figure 2.17. Trajectory of flexible aircraft varying gust alleviation factor

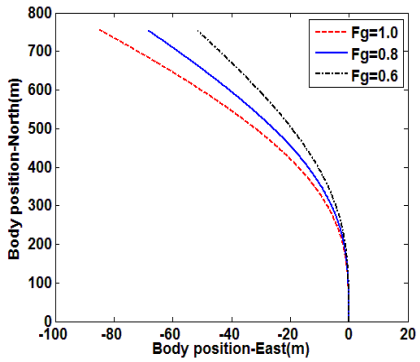

(a) Aircraft lateral and longitudinal position

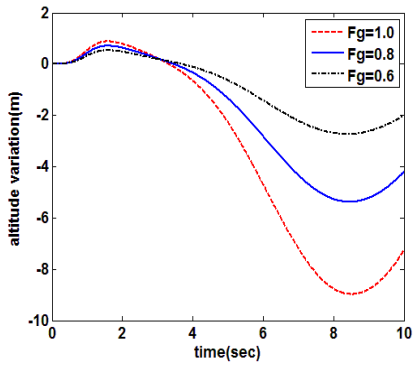

(b) Altitude variation

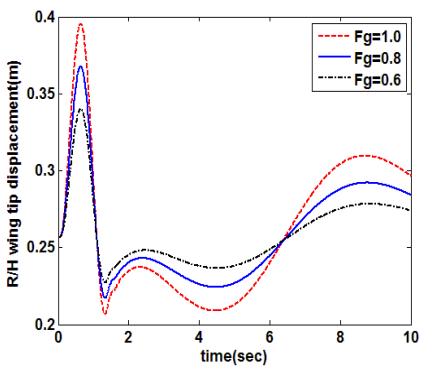

(c) R/H wing tip deflection

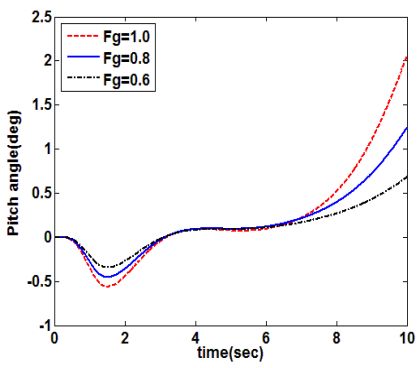

(d) Aircraft pitch angle variation

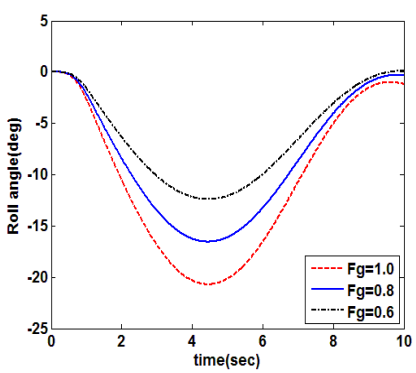

(e) Aircraft roll angle variation

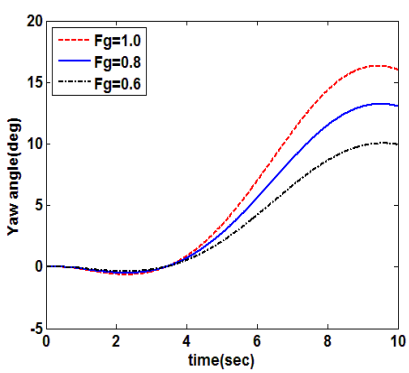

(f) Aircraft yaw angle variation

Figure 2.18. Flight dynamic response varying the gust alleviation factor

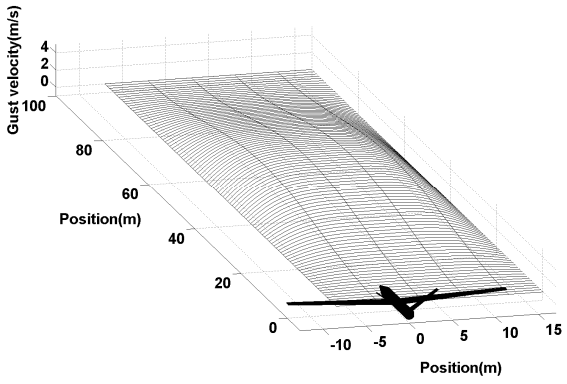

(a) Gust position is 5m

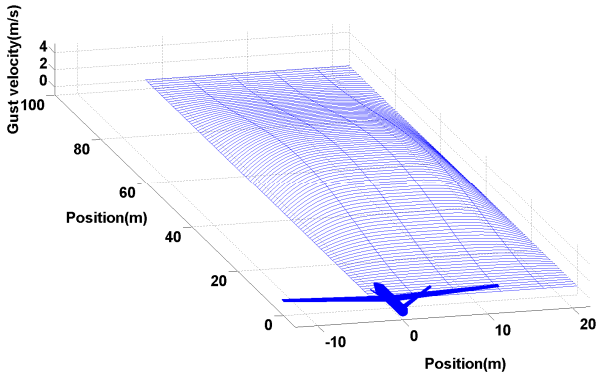

(b) Gust Position is 10m

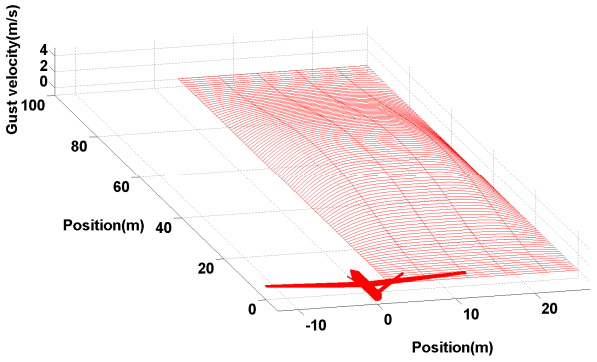

(c) Gust Position is 15m

$* H = 50\text{m},\ F_g = 0.8,\ r_0 = 12\text{m},\ n_E = 2$

Figure 2.19. Gust shape varying gust position

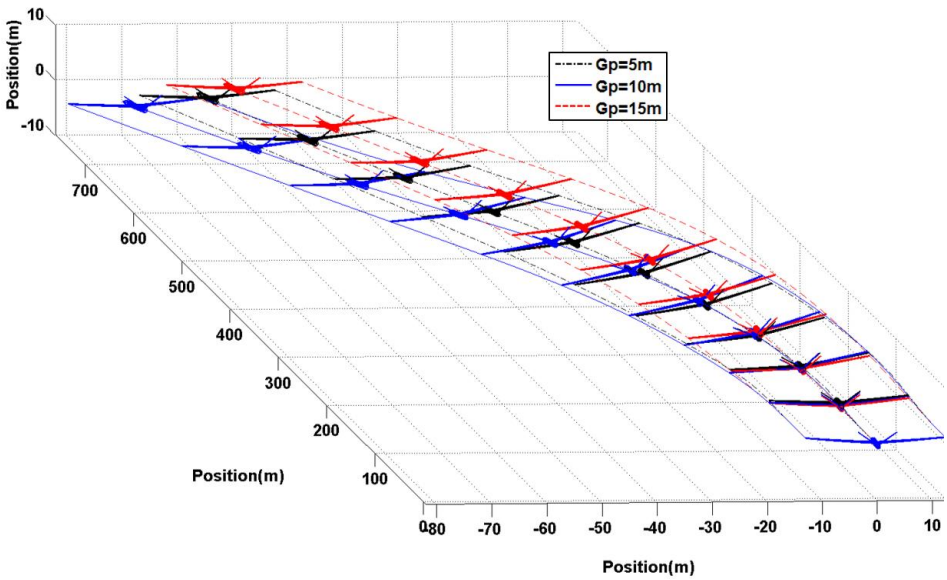

Figure 2.20. Trajectory of flexible aircraft varying gust position

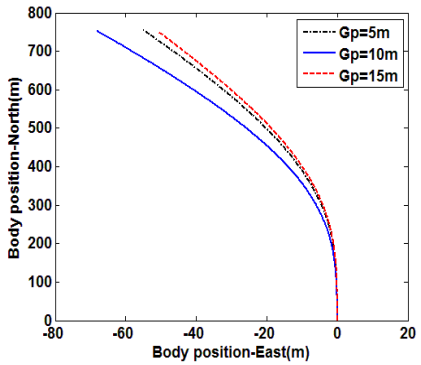

(a) Aircraft lateral and longitudinal position

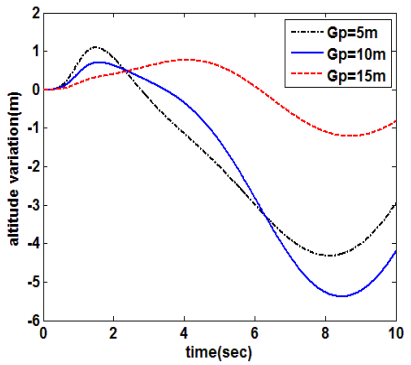

(b) Altitude variation

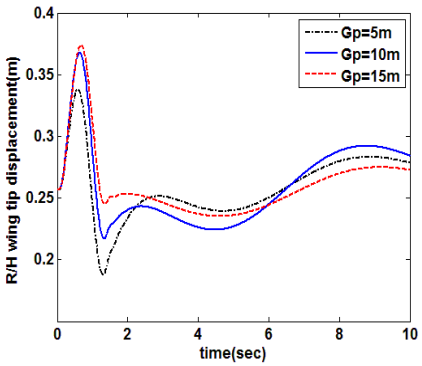

(c) R/H wing tip deflection

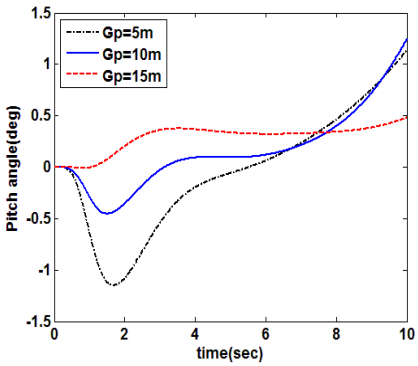

(d) Aircraft pitch angle variation

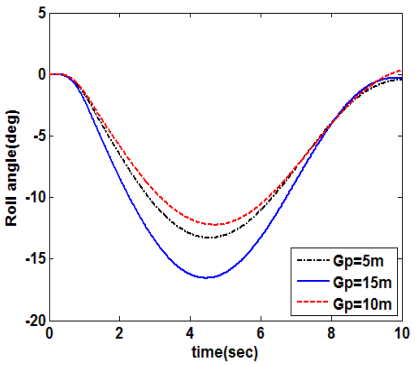

(e) Aircraft roll angle variation

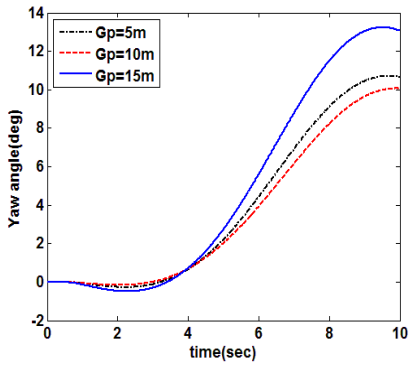

(f) Aircraft yaw angle variation

Figure 2.21. Flight dynamic response varying the gust position

3. EVALUATION OF GUST LOADS CERTIFICATION METHOD FOR FLEXIBLE AIRCRAFT

This chapter focuses on analyzing discrete gust loads estimation for flexible aircraft transient analysis and comparing the results with Pratt and Walker's method which is widely using for the quasi-static gust loads analysis—basis for FAR(Federal Aviation Regulation) Part 23 gust certification requirement.

3.1. Overview of Gust Loads Certification Method

As aircraft wing is slender and the gross weight is lower, the gust effect is greater. The gust load evaluation is important to investigate the aircraft structure integrity, controller design and so on. Methods for determining gust loads have been developed and used for design and certification have evolved over the years [34]. Gust loads analysis can be approached using quasi-static, transient, or continuous methodologies.

Firstly, quasi-static methods enable a static representation of gust encounters without solving equations of motion. This method reduces the computational expense of the analysis. Otherwise, quasi-static methods provide a lower-fidelity and lower-cost option. A great diversity of flight case can be considered. The most rational gust loads calculation is developed by Pratt and Walker [55] which is basis for gust load evaluation in the Federal Aviation Regulation (FAR) part 23 certification requirements. This method is based on rigid flight dynamic equations of motion and 1-cosine gust profile to determine the peak load factor. The

overview of this method will be presented in later sections. Transient methods are based on that the equations representing the system are solved with time as an independent variable. FAR Part 25 certification requires many 1-cosine profile gusts over a range of gust lengths be analyzed using transient analysis. However, a few codes are available for solving nonlinear transient gust response cases and the worst case gust profile is not a given. Continuous methods offer a robust representation of the atmosphere, because the atmosphere is continuous and random. This methods allow for a statistical representation of turbulence. On the other hand, it has not superseded transient analysis for design and certification because flight data recorders have shown that larger gusts often stand out as discrete events [56]. Transient analyses using discrete gust are better suited for predicting gust loads. For these reason, both transient and continuous method are required for FAR part 25 certification [57]. This study focuses on analyzing discrete gust loads evaluation for flexible aircraft transient analysis and comparing the results with quasi-static method.

3.2. Quasi-Static Gust Load Certification

Quasi-static methods are divided into two categories [58]. One is the sharp-edge gust profile and the other is sharped gust profile. The sharp-edge is derived based on the assumption that the aircraft vertical velocity is changed encountering the gust. The basic lift change can be expressed as

$$\Delta L = \frac{1}{2}\rho V^2 S C_{L_\alpha} \Delta\alpha \tag{3.1}$$

where L is lift, ρ is atmospheric density, V is airspeed, S is the wing

reference area, and C_{L_α} is the lift curve slope. $\Delta\alpha$ is the change in angle of attack. Using this equation and aircraft weight W, the load factor change can be obtained

$$\Delta n = \frac{\Delta L}{W} \tag{3.2}$$

This formula neglected unsteady aerodynamics and vertical motion of the aircraft. Thus, some method introduced account for these effects. One of the rational sharped gust profile is Pratt method which is dominant quasi-static method since its introduction [55]. Pratt method using the '1-cosine' gust profile and the empirical data to find the peak loads without solving the flight dynamic equations of motion and to determine the peak load factor. In Pratt method, there are some assumptions which are the aircraft is a rigid body, forward speed is constant. The aircraft is steady level flight and after entered into the gust aircraft rise without pitch. And fuselage and horizontal tail lift increment neglect. Gust velocity is uniform across the wing span and parallel to the vertical axis. The critical gust length was assumed to be 25 chords which is based on empirical data [58].

If there is no lag in buildup of the lift, equilibrium of vertical forces results as

$$M\ddot{z} + \frac{\rho}{2}V^2 S C_{L_\alpha}\frac{\dot{z}}{V} = \frac{\rho}{2}V^2 S C_{L_\alpha}\frac{U(t)}{V} \tag{3.3}$$

where M is aircraft mass, z is aircraft vertical displacement, and U is gust velocity which is varying with time. For generalized solution, dimensionless time s is used as

$$s = \frac{tV}{\bar{c}} \tag{3.4}$$

where $\bar{c}$ is the wing mean aerodynamic chord. For considering lift lag, two lag

functions are used. The Wagner function K_W is used which is the indicial function of the buildup of lift due to an instantaneous change in angle of attack. And the Küssner function K_G is used as the indicial function of the buildup of the lift due to a sharp-edge gust. Using dimensionless time and simplified these lift lag functions, the differential equation becomes

$$\frac{d^2z}{ds^2}+\frac{1}{\mu_g}\int_0^s K_W\left(s-s'\right)\frac{d^2z}{ds'^2}ds'=\frac{1}{\mu_g}\frac{\overline{c}U_0}{V}\int_0^s K_G\left(s-s'\right)\frac{d}{ds'}\left(\frac{U}{U_0}\right)ds' \quad (3.5)$$

where μ_g is dimensionless mass ratio and U/U_0 is normalized gust intensity '1-cosine' gust profile which is assumed the gust length as 25 chords shown as Fig.3.1. These terms are expressed as

$$\mu_g=\frac{2W}{\rho g S\overline{c}C_{L_\alpha}} \quad (3.6)$$

$$\frac{U}{U_0}=\frac{1}{2}\left(1-\cos\frac{2\pi s}{25}\right) \quad (3.7)$$

For each value of μ_g and the maximum acceleration d^2z/ds^2, the maximum load factor change can be solved as

$$\Delta n=\frac{\ddot{z}}{g}=\frac{1}{g}\frac{V^2}{\overline{c}^2}\frac{\overline{c}U_0}{V}\left(\frac{d^2z}{ds^2}\right)_{\frac{\overline{c}U_0}{V}=1} \quad (3.8)$$

This equation can be change into

$$\Delta n=\mu\left(\frac{d^2z}{ds^2}\right)_{\frac{\overline{c}U_0}{V}=1}\frac{\rho U_0 V C_{L_\alpha}}{2W/S}=K_g\Delta n_{sharp-edge\ gust} \quad (3.9)$$

The coefficient K_g is the knockdown factor which is approximated as

$$K_g=\frac{0.88\mu_g}{5.3+\mu_g} \quad (3.10)$$

This term includes not only the effect of the airplane motion, but also the lag in buildup of lift in response to gust entry and sudden changes in angle of attack.

Pratt method allows to calculate the gust load factor due to the discrete gust by a three-step process without solving the flight dynamic equations of motion, the aircraft load change due to the gust can be calculated.

Calculate the aircraft mass ratio: $\mu_g = \frac{2W}{\rho g S \bar{c} C_{L_\alpha}}$ (3.11)

Calculate the knockdown factor: $K_g = \frac{0.88\mu_g}{5.3 + \mu_g}$ (3.12)

Calculate the change in load factor: $\Delta n = K_g \left(\frac{\rho U_0 V C_{L_\alpha}}{2W/S} \right)$ (3.13)

We calculate the critical gust for three flight velocity conditions. The aircraft flight altitude is 10,000m and the flight velocity is 70, 75, and 80m/s, respectively. The gust intensity is about 5.3 m/s and the critical gust gradient is about 16.7m. First, using the aircraft mass ratio, we can obtained the knockdown factor is about 0.8 as show Fig. .2. Which means that the aircraft is one of the conventional aircraft type. The load changes due to the gust are 20.85%, 22.34% and 23.83%, respectively, shown as Fig.3.3 (a). Using this increased load factor, the R/H main wing root bending moment is obtained as Fig.3.3 (b). Although the gust gradient is same, the different gust entered aircraft velocity leads the different gust load.

3.3. Critical Gust for Flexible Aircraft based on Transient Analysis

Three types of uniform gusts were applied as shown in Fig.3.4. for flexible aircraft flight dynamics depending on the magnitude of gust gradient. The aircraft

is flying at 75 m/s in a trim state, and gusts are acting vertically. Fig.3.5 and Fig 3.6 shows the trajectory and structure responses for each gust cases. As the larger the size of the gust, the greater the effect on the aircraft flight path and the displacement of the right wing tip is less changed. On contrast, the smaller the magnitude of the gust, the less the altitude change is, but the instantaneous load is applied to the wing and the displacement is large.

As we mentioned that uniform gust can be expressed using the two gust parameters—the gust gradient H and the flight profile alleviation factor F_g. We performed simulation changing the gust parameter H ranged from 10 to 107m and F_g ranged from 0.1 to 1.0 to evaluate the gust effect including the Pratt method critical gust parameters. The thrust and ruddervator are same as trim parameters during the analysis. About three hundred cases are included for each aircraft velocity.

Fig.3.7. shows the maximum bending moment due to the gust parameters at aircraft velocity is 75m/s. As F_g is increased, the maximum bending moment is increased. Otherwise, gust gradient bound from 10 to 20m, the bending moment is higher than the other cases, which range contains the obtained critical gust gradient through the Pratt method. Fig. 3.8. shows the maximum bending gust for each aircraft velocity. The H is varying 10 to 105m while F_g is 1.0. Although the same gust affects the aircraft, the aircraft response depends on the aircraft velocity because as aircraft velocity increasing, the penetrate gust time is shorter. This leads that the gust affects more critical to the structure.

For determining the maximum bending moment through the transient analysis, the optimization is performed. Table 3.1. shows the comparison Pratt method with

flexible aircraft analysis results for critical gust gradient H and maximum bending moment at R/H main wing root. The critical gust gradient is similar between the two results but critical gust from Pratt method is fixed, otherwise transient analysis case is varying. As the aircraft velocity increase, the critical gust range also increase. The maximum bending moment ratio which is normalized using trim state bending moment is increased as the aircraft velocity is higher both methods. Otherwise, the bending moment ratio from the flexible aircraft analysis is higher than Pratt method. From these results, as the aircraft velocity is higher, critical gust range and bending moment is increased.

Fig.3.9. shows the flexible aircraft flight critical gust cases for each aircraft velocity. The constant pitch assumption seems reasonable for this aircraft because the attitude variation is not extreme. The maximum bending moment is occurred in the gust range, and passed the gust region, the aircraft recover the trim state because of the aircraft stability.

We observed gust load evaluation considering the maneuvering because the gust can affect while the aircraft is pitch-up or pitch-down which is cannot be obtained by Pratt method. In Pratt method, the lift increments of the horizontal tail is negligible in comparison with the wing lift increment. During the maneuvering, the increment tail lift affects the aircraft flight dynamics. When the control surface is operated, the maneuver load is generated and affected to the aircraft and gust effect. Fig.3.10. shows the trajectory the trim, pitch-up and pitch-down. The aircraft flight altitude is 10,000m and velocity is 75m/s. Control surface is operated trim state ± 0.5 degree. During the simulation the thrust is maintained as initial value.

The aircraft structure responses are shown as Fig.3.11. As the aircraft is pitch-up,

the altitude and attitude are increasing, the velocity is decreasing. As apex is reached and the aircraft begins a dive because of the loss of life from insufficient airspeed. The aircraft flights less than trim state. As the aircraft is pitch-down, otherwise, the altitude and attitude is decreased and velocity is increased. The aircraft flights more than trim state. The maneuver load is more or less about 11% comparison with the trim state and the maximum or minimum bending moment is generated about two seconds. The maximum or minimum of aircraft pitch angle more or less about four degree comparison trim state at about seven second. Through these result, as the control surface is manipulated, the aircraft response is different from trim state. The maneuver load is generated and the flight condition is varying. This response make the gust loads be different from trim state.

Considering the maneuver load, we simulate as changing the gust start time. The gust is as same as trim state critical gust—the gust gradient is about 13.7m and the alleviation factor is 1.0. Firstly, the tail control surface is operated when the aircraft entering gust simultaneously. The aircraft is in steady level flight prior to entry into the gust, otherwise, the lift increments of the tail is not be able to neglect. As shown Fig.3.12, the responses are little different from the trim state because the aircraft flight conditions are similar to the trim state and the maneuver load is increased but small. Next, the tail control surface is operated at two seconds when the maneuver loading is around the maximum. The aircraft forward speed, pitch angle and deformation are different from trim state. The aircraft is not in steady level flight prior to entry into the gust. The response is shown as Fig.3.13. Due to the maneuver loading, the maximum bending moments are increased. Table 3.2 shows that the maximum bending moment ratio about the gust start time. The

maximum bending moment is changed due to the aircraft flight state including maneuver. The maximum bending moment is generated due to the gust and maneuver load, the value is similar to the summation of these two value when the fight state is not different from the trim state. Otherwise, the different flight state, for example velocity and aircraft pitch angle, leads the response is changed.

The various case studies are presented regarding to gust parameters and three aircraft velocity to determine the critical gust shape. Although the critical gust parameters are different due to the aircraft velocity, it was found that Pratt and Walker's analysis results were reasonable for the flexible aircraft gust load analysis. The critical gust parameters are similar to the Pratt method although the maximum bending moment higher than Pratt method. Pratt method gust loads analysis for the flexible aircraft slightly under-predicted the maximum loads from transient analysis. Under maneuvering, the flexible aircraft gust load analysis which cannot be analyzed through the Pratt method is different from trim state gust load analysis. The value of the maximum bending moment is similar the value which is the summation of maneuver load and the gust load. Based on these results, it is concluded that the flexible aircraft gust load analysis can be performed efficiently by using the Pratt method critical gust load analysis. Using the maneuver load analysis, the gust load analysis under maneuvering can be obtained efficiently without analysis the all cases.

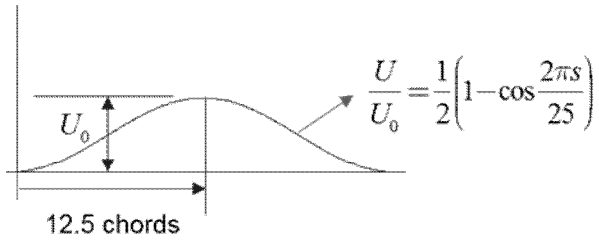

Figure. 3.1. '1-cosine' gust profile in Pratt method

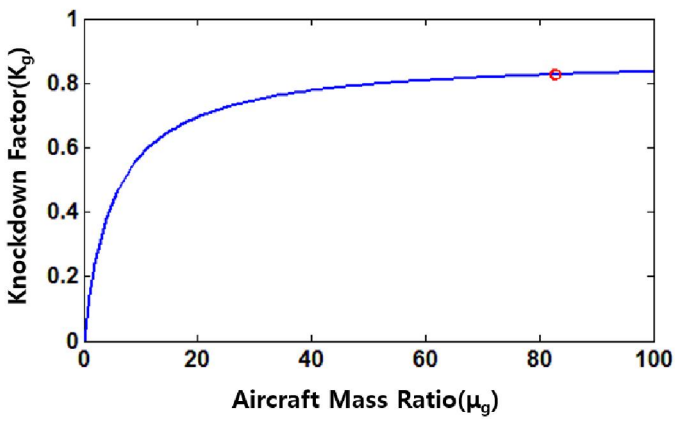

Figure. 3.2. The knockdown factor

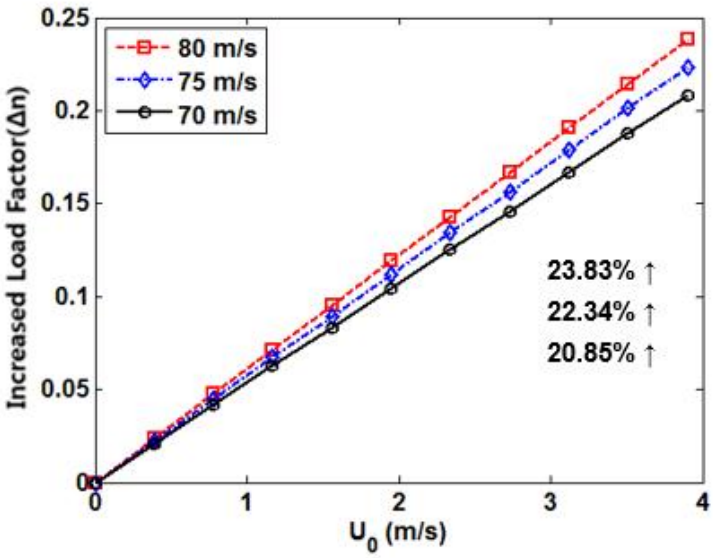

(a) Increased load factor

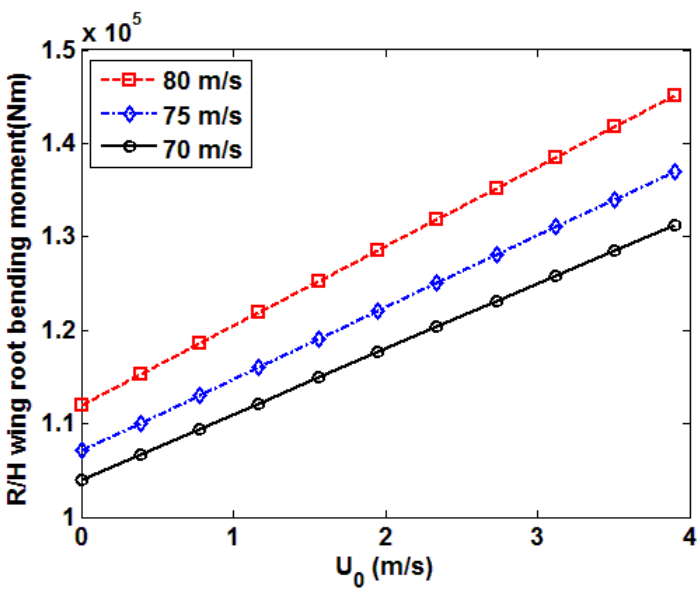

(b) R/H main wing root bending moment

Figure 3.3. The load factor and main wing root bending moment

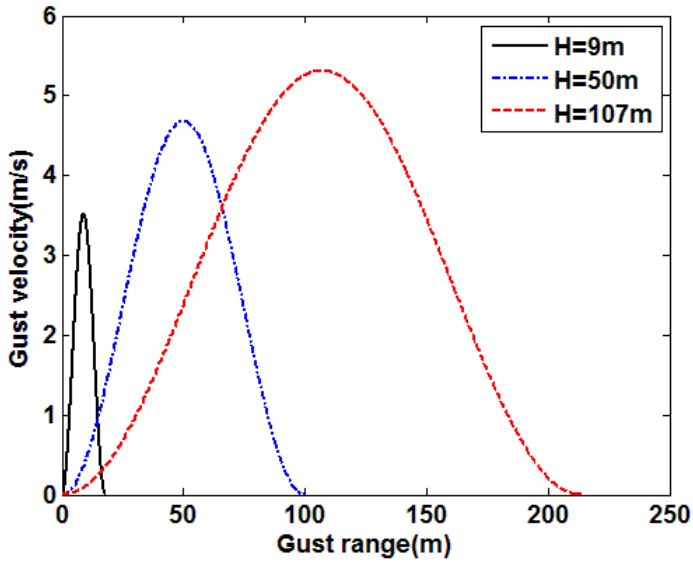

Figure 3.4. Gust shape

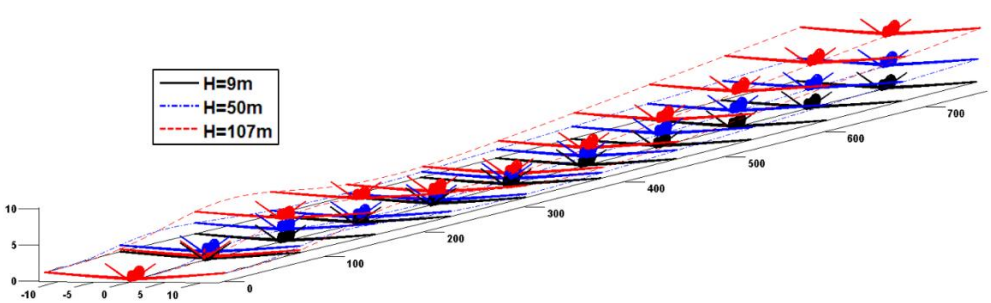

Figure 3.5. Flexible aircraft trajectory varying gust gradient

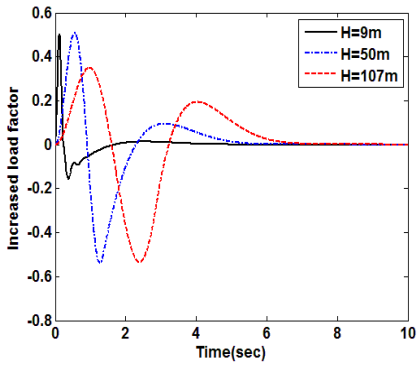

(a) Increased load factor

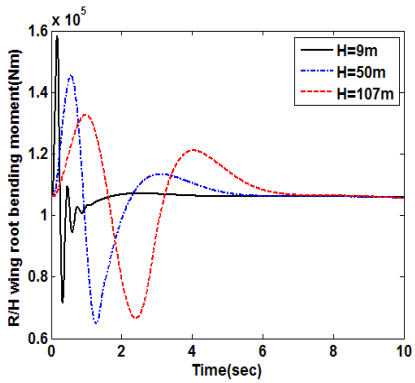

(b) R/H main wing root bending moment

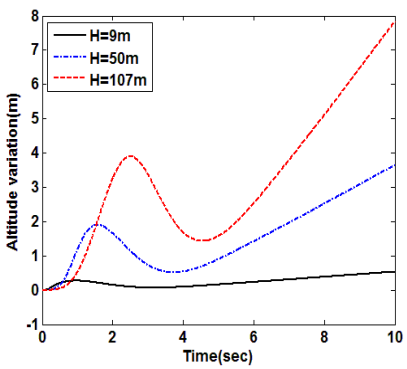

(c) Altitude variation

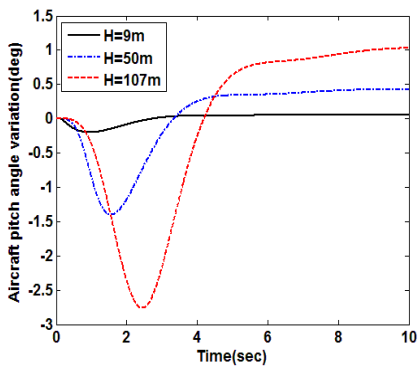

(d) Pitch angle variation

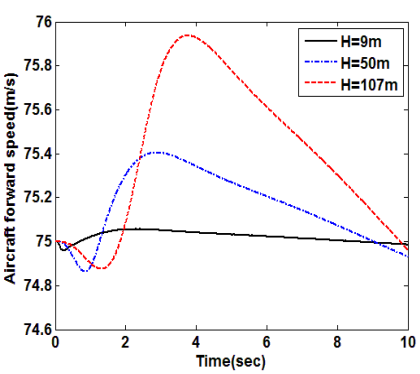

(e) Forward speed

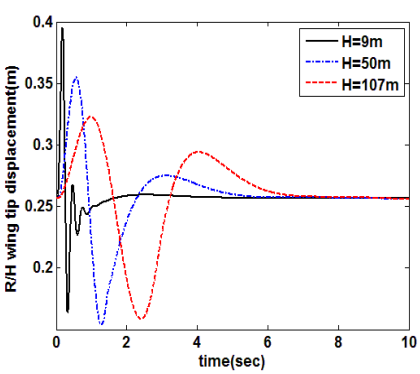

(f) R/H main wing tip displacement (z-axis)

Figure 3.6. Flexible aircraft response varying gust gradient

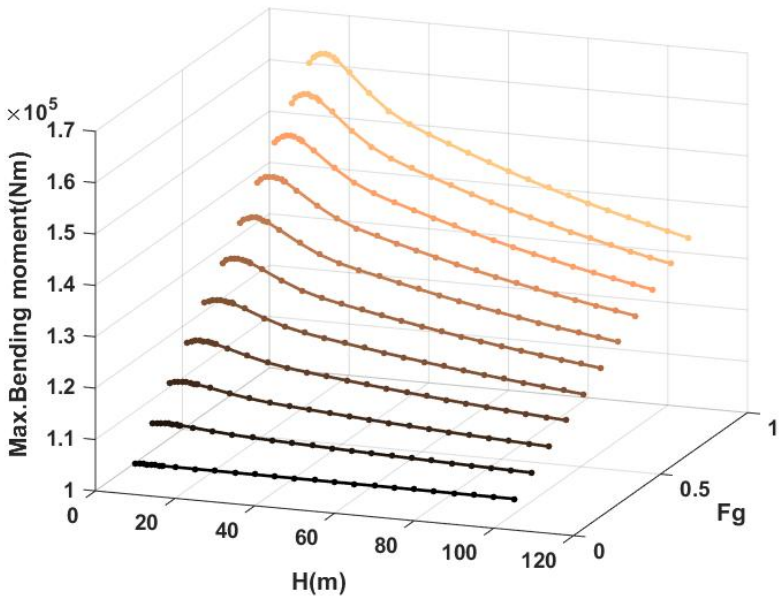

Figure 3.7. Gust parametric response of flexible aircraft

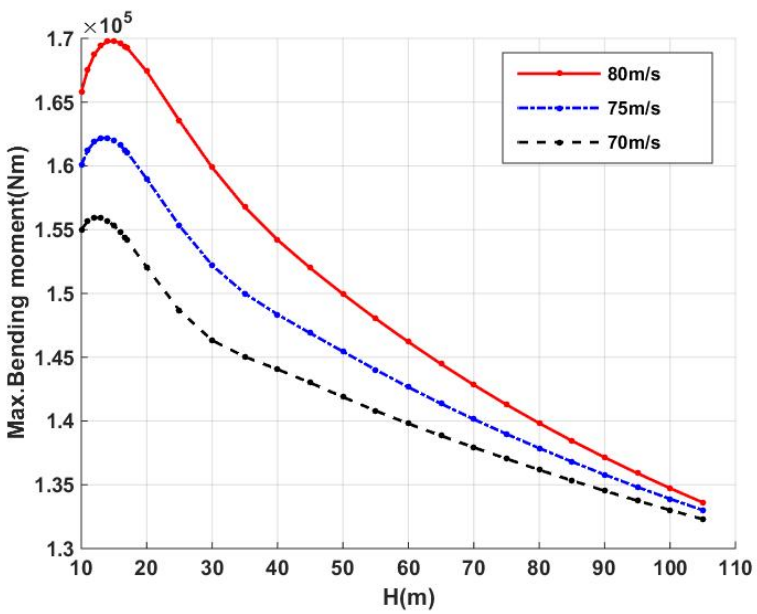

Figure 3.8. Gust parametric response due to the flexible aircraft velocity

Table 3.1. Maximum bending moment from Pratt method and transient analysis

Aircraft Velocity	Pratt (A)		Flexible aircraft (B)		Difference (B-A)	Ratio ((B-A)/A)
	Critical gust(m)	Max.B.M.(Nm)	Critical gust(m)	Max.B.M.(Nm)	B.M.(Nm)	Percent(%)
70	16.7373	1.3129×10^5	11.8145	1.5596×10^5	0.2467×10^5	18.79
75	16.7373	1.3703×10^5	13.6515	1.6227×10^5	0.2524×10^5	18.42
80	16.7373	1.4506×10^5	14.7620	1.6984×10^5	0.2478×10^5	17.08

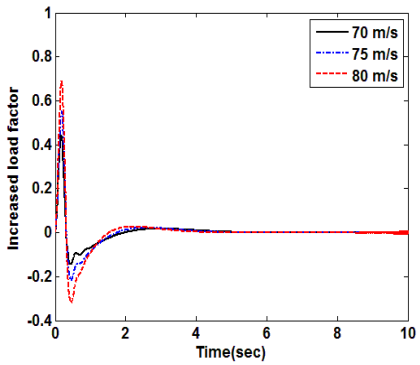

(a) Increased load factor

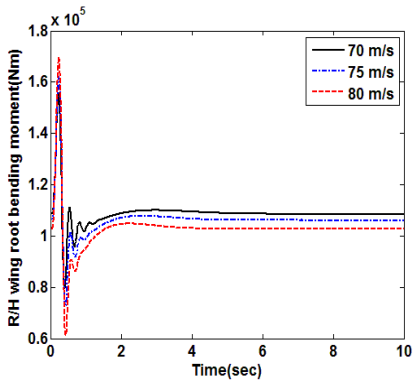

(b) R/H main wing root bending moment

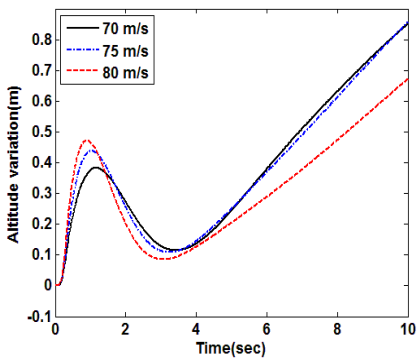

(c) Altitude variation

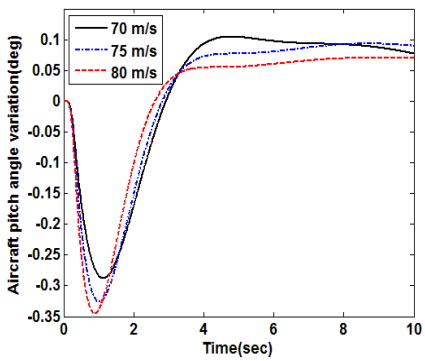

(d) Pitch angle variation

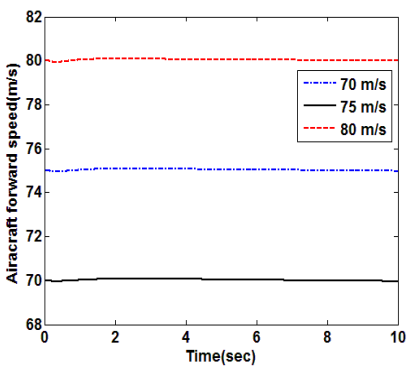

(e) Forward speed

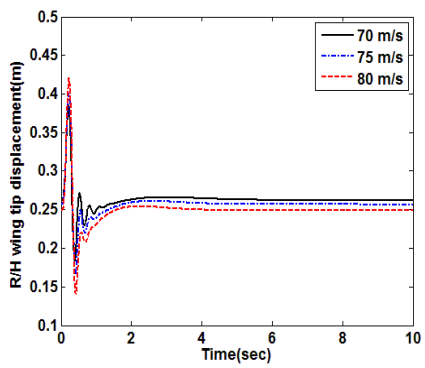

(f) R/H main wing tip displacement (z-axis)

Figure.3.9. Critical gust parametric response

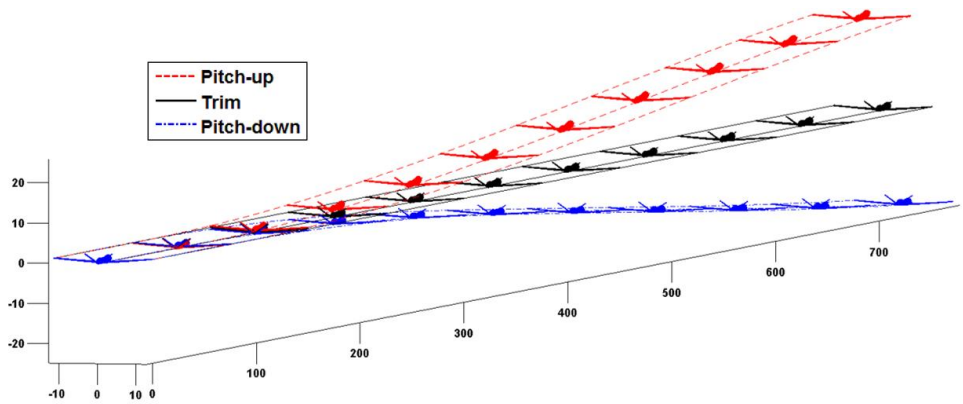

Figure 3.10. Trajectory of the flexible aircraft

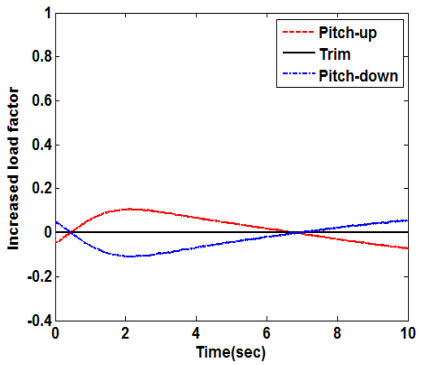

(a) Increased load factor

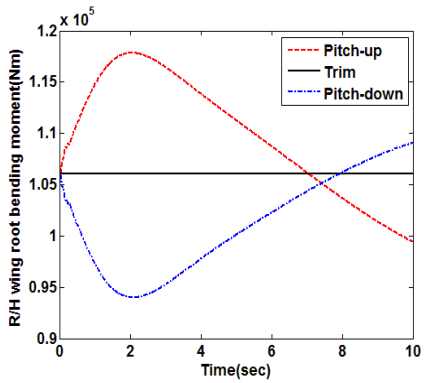

(b) R/H main wing root bending moment

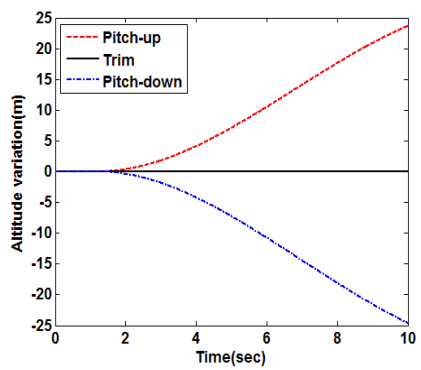

(c) Altitude variation

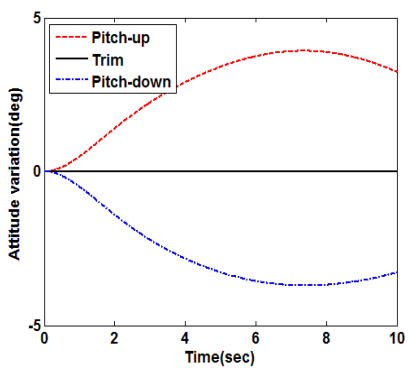

(d) Pitch angle variation

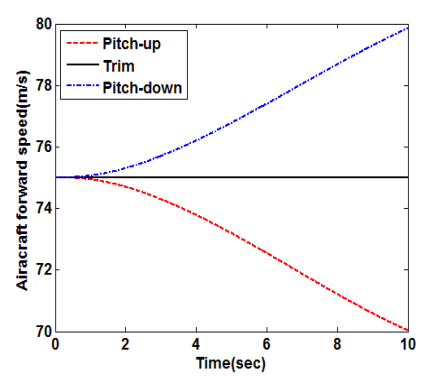

(e) Forward speed

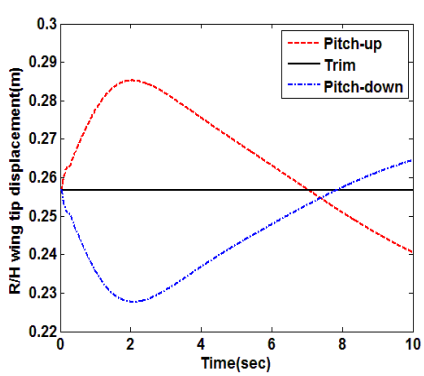

(f) R/H main wing tip displacement (z-axis)

Figure 3.11. Flexible aircraft response under maneuvering

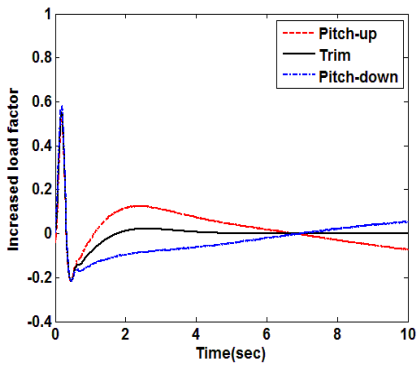

(a) Increased load factor

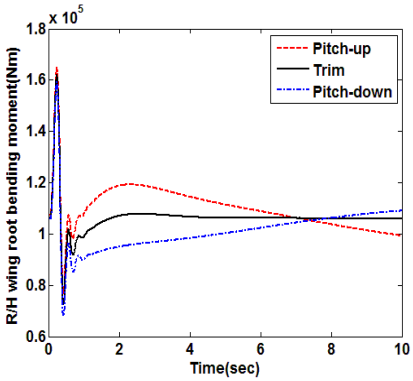

(b) R/H main wing root bending moment

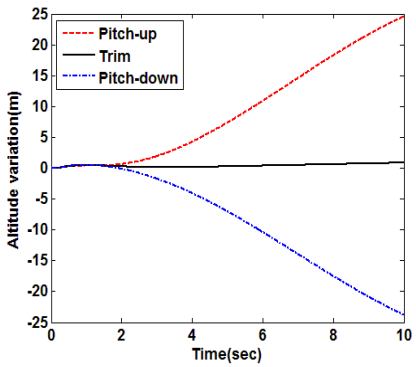

(c) Altitude variation

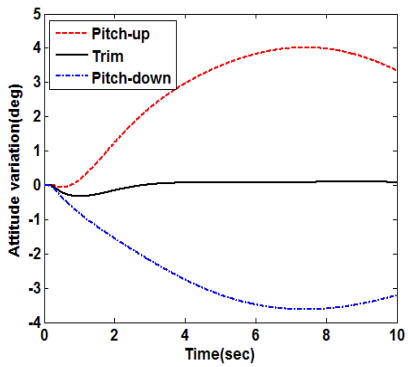

(d) Pitch angle variation

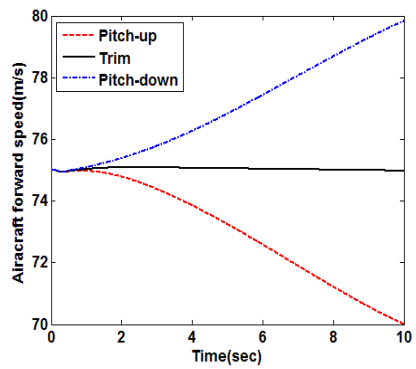

(e) Forward speed

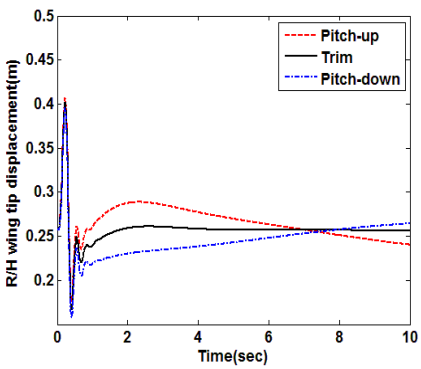

(f) R/H main wing tip displacement (z-axis)

Figure. 3.12. Flexible aircraft response under maneuvering, gust start 0 sec

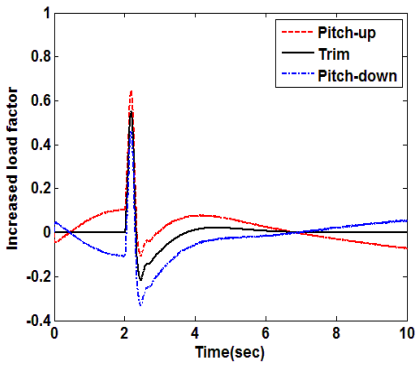

(a) Increased load factor

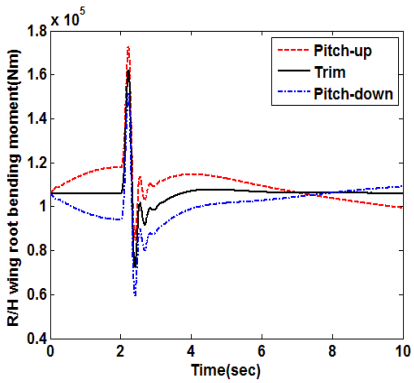

(b) R/H main wing root bending moment

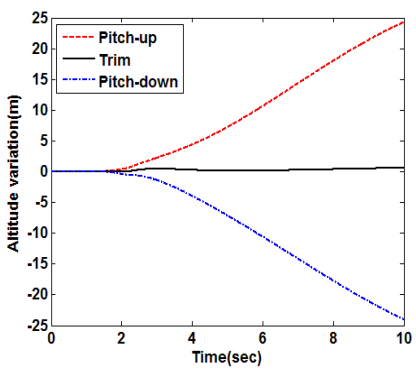

(c) Altitude variation

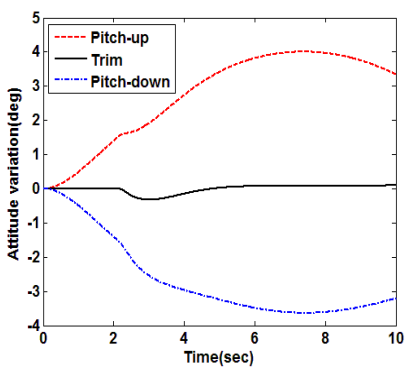

(d) Pitch angle variation

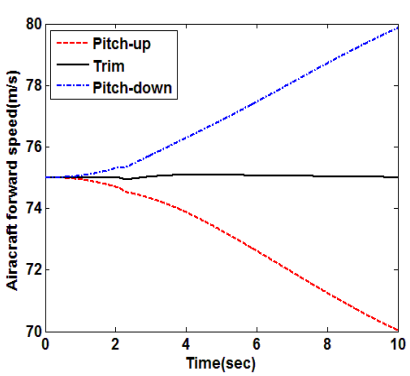

(e) Forward speed

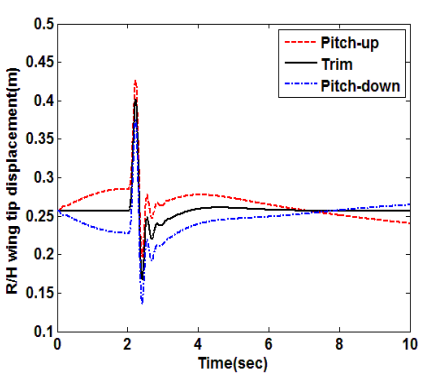

(f) R/H main wing tip displacement (z-axis)

Figure 3.13. Flexible aircraft response under maneuvering, gust start 2 sec

Table 3.2. Maximum bending moment from Pratt method and transient analysis due to gust start time

Flight condition	Pratt	Flexible Aircraft transient analysis		
	Gust	No gust	Gust at 0sec	Gust at 2sec
Pitch-up	-	1.1788×10^5 Nm	1.6522×10^5 Nm	1.7275×10^5 Nm
Trim	1.3703×10^5 Nm	1.0608×10^5 Nm	1.6227×10^5 Nm	1.6227×10^5 Nm
Pitch-down	-	0.9399×10^5 Nm	1.5932×10^5 Nm	1.5142×10^5 Nm

4. FLIGHT LOAD ESTIMATION THROUGH GUST IDENTIFICATION

4.1. Motivation

The objective of this work is force estimation for the flexible aircraft affected by the gust. The flexible aircraft model is coupled with unsteady aerodynamic model with control surface and the parameterized gust model. Some structure responses are used as the reference data under consideration of the measuring device installation, for example, altitude variation and some wing point accelerations. The optimization process is set up to identify the gust parameters which generates the same response as the reference data. Using this identified gust, we can estimate the forces through the forward flexible aircraft analysis.

The forces acting on the aircraft is related on the flight condition and gust. Some forces can be roughly estimated from the aircraft device or the aircraft flight attitude, for example gravity and thrust. However, the aerodynamic force is not easy to estimate especially considering the gust. In this section, we identify the gust parameters using optimization method until getting the same response as the reference data. Using the identified gust parameters, the force acting on the aircraft is reconstructed by the forward analysis.

4.2. Gust Identification based on Inverse Problem Theory

Gust parameter identification is one of the inverse problems, which estimates the gust information by using the flexible structure dynamic response, that is, acceleration, deformation and strain so on. Fig.4.1. shows the gust parameters

identification through the optimization process. The aircraft responses are obtained through the flexible aircraft analysis considering gust parameters and flight condition. Using these responses, the unknown gust parameters are identified. However, only limited response data can be used, for example wing tip acceleration or specific position strain gage data, because only few sensors can be attached during the flight test. We assumed that the available data are three point wing acceleration data set at the right side wing as Fig.2.2 which is based on the real flight test sensor installation information. Aircraft altitude, aircraft body angles and velocity information are acquired from aircraft flight data.

Using these data, we estimate the gust through the optimization method. We defined the cost function as below:

$$J_{gust} = \left[\underbrace{W_a \left\{ \left(\mathbf{R}_{ref}(t) - \mathbf{R}_{cal}(t) \right)^2 + \left(\dot{\boldsymbol{\theta}}_{ref}(t) - \dot{\boldsymbol{\theta}}_{cal}(t) \right)^2 \right\}}_{\text{Aircraft Flight Data}} + \underbrace{W_b \left(\ddot{\mathbf{x}}_{ref}(t) - \ddot{\mathbf{x}}_{cal}(t) \right)^2}_{\text{Wing Sensor Data}} \right] \rightarrow \min \tag{4.1}$$

The foot note *ref* means the reference data and *cal* is the calculated data using the optimized gust parameters. $\mathbf{R}$ is the altitude data and $\dot{\boldsymbol{\theta}}$ is the pitch rate, which are at the aircraft reference point and $\ddot{\mathbf{x}}$ is the acceleration data at right wing data. The aircraft trajectory might be matched, firstly, the detailed response can be matched otherwise the gust parameters are obtained at local minimum. The weighting W_a and W_b are used under considering the order of value. The cost function J_{gust} is minimized using the gust parameters which are the gust gradient H and the flight profile alleviation factor F_g which are same as uniform gust. The radius of the gust region r_0, spanwise adjusting the gust spatial distribution

parameters n_E and the gust center position parameter G_p as mentioned at chap.2.2. and the gust parameter optimization problem is described as

$$\begin{aligned} &\text{minimize} && J_{gust} \\ &\text{with respect to} && H,\ F_g,\ r_0,\ n_E,\ G_p \\ &\text{Subject to} && \begin{aligned} &30\,ft \le H \le 350\,ft, && 0 < F_g \le 1.0 \\ &5m \le r_0 \le 50m, && 0 < n_E \le 5, \\ &-15m \le G_p \le 15m \end{aligned} \end{aligned} \tag{4.2}$$

Fig.4.3 and 4.4 shows trajectory and responses at the trim and non-uniform gust whose parameters are $H = 50\text{m},\ F_g = 0.8,\ r_0 = 15\,\text{m},\ n_E = 2,\ G_p = 5\text{m}$. This non-uniform gust response is used as the reference and the gust parameters are identified through the optimization process as the Fig.4.1. The initial gust parameters are as follows: $H = 40\text{m},\ F_g = 0.9,\ r_0 = 16\,\text{m},\ n_E = 2.2,\ G_p = 8\text{m}$. The initial gust is modeled as the gust range is shorter, maximum velocity is higher and the position is farther than those of reference gust as the Fig. 4.5. Table 4.1 shows the flight dynamic results for reference, initial and optimized gust cases. We can get the optimized gust parameter through this method where the maximum difference between reference and optimized parameters are under 0.01%.

4.3. Reconstruction Flight Loads using Identified Gust

The gust is modeled by using the identified gust parameters, the force on the aircraft can estimate through the forward flexible aircraft analysis. Fig.21. shows each axis force and moment about the aircraft reference point. At the trim condition, the force and moment do not vary. Otherwise, due to the gust, the aircraft goes to the left and rises. After gust region, the flight state recovers due to the stability.

We can estimate also the vertical force at each node and wing root bending moment at the main wing as shown in Fig.4.7. At trim condition, the forces are same as initial both right and left wing. Otherwise, due to the gust, the force is increased due to the gust about 30~40% at each nodes at which the sensor is located the right side wing. At left wing, the nodes are selected as same distance from the center as right wing sensor position. The left wing force is different from the right wing, the maximum bending moment at R/H main wing root is increased about 32% compared to that in trim condition. On the other hand, the maximum bending moment is increased about 5% at left wing.

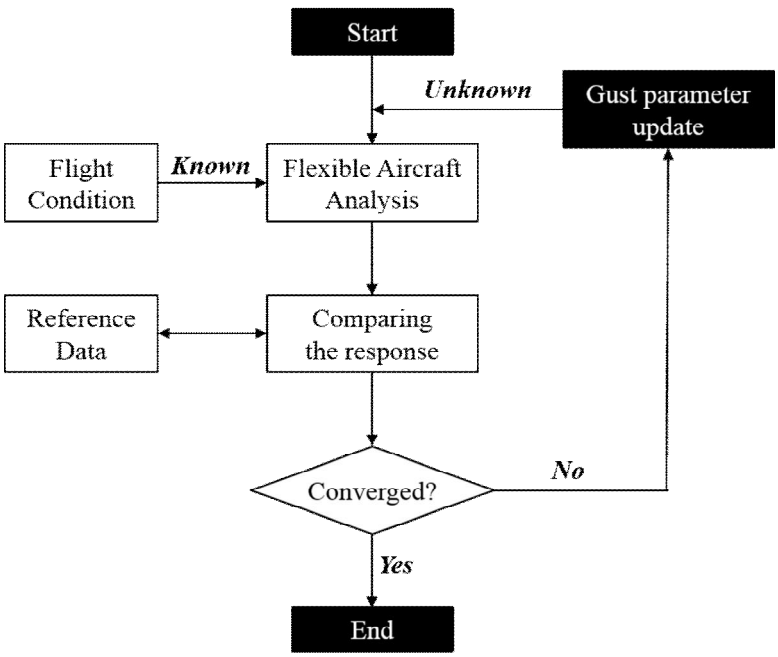

Figure 4.1. Gust parameter identification through the optimization method

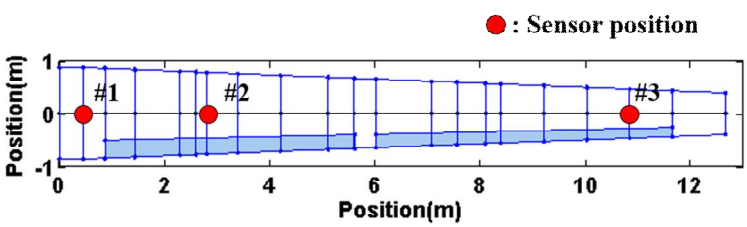

Figure 4.2. Data measure point of R/H wing

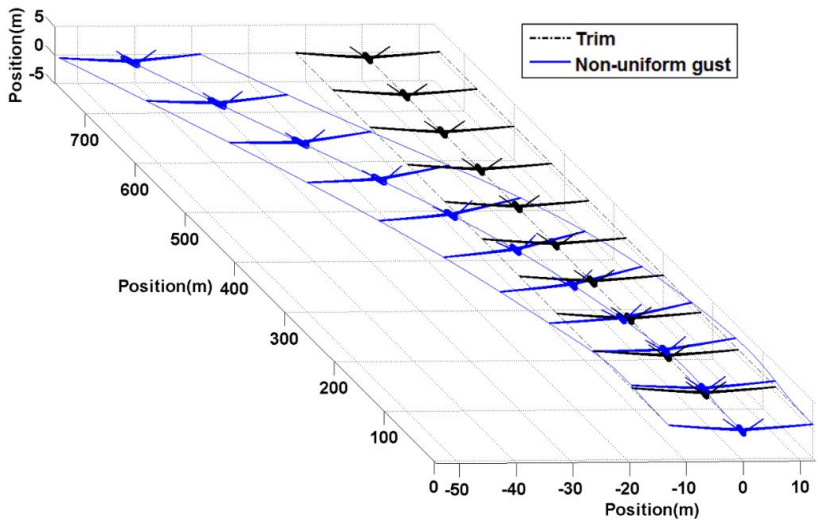

$* H = 50\text{m},\ F_g = 0.8,\ r_0 = 15\,\text{m},\ n_E = 2,\ G_p = 5\text{m}$

Figure. 4.3. Trajectory of flexible aircraft trim and non-uniform gust

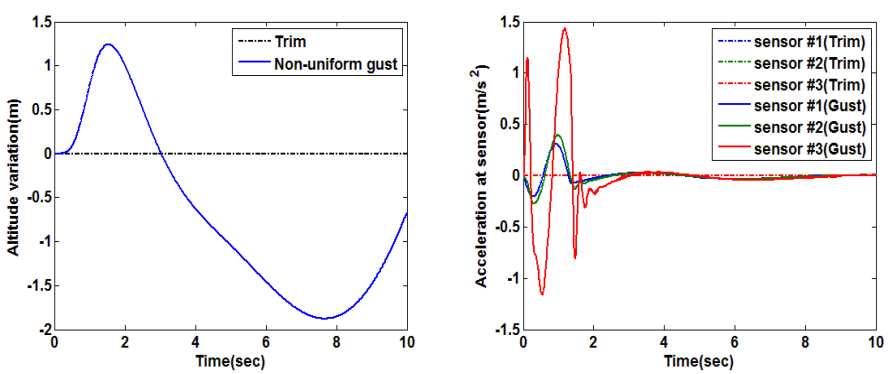

(a) Aircraft lateral velocity variation (b) R/H wing acceleration

Figure 4.4. Dynamic response for trim and non-uniform gust

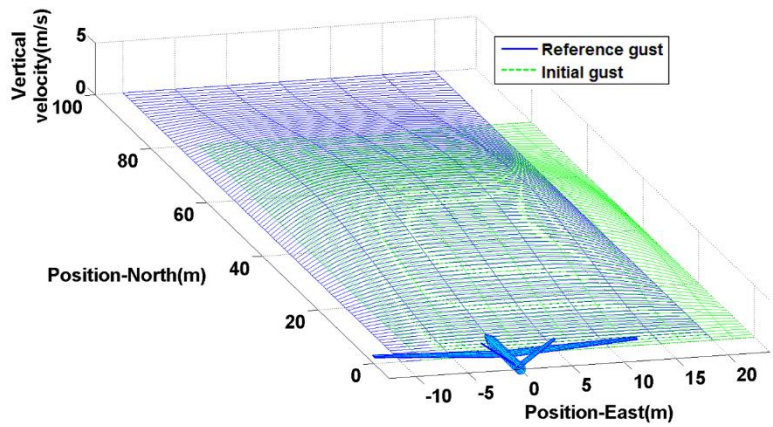

*initial : $H = 40\text{m},\ F_g = 0.9,\ r_0 = 16\,\text{m},\ n_E = 2.2,\ G_p = 8\text{m}$

Figure 4.5. Reference and initial discrete non-uniform gust distribution

Table 4.1. Identified gust parameter

Value	H	F_g	r_0	n_E	G_p
Reference (A)	50	0.8	15	2	5
Initial	40	0.9	16	2.2	8
Optimized (B)	50.00	0.80	15.00	2.00	5.00
Difference (A-B) (%)	-0.1132×10^{-4} (-0.0000)	-0.0112×10^{-4} (-0.0001)	-0.0159×10^{-4} (-0.0000)	0.5234×10^{-4} (0.0026)	0.5517×10^{-4} (0.0011)

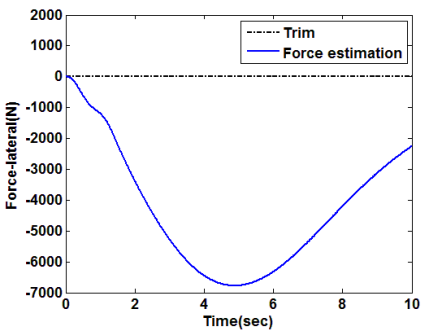

(a) Lateral force

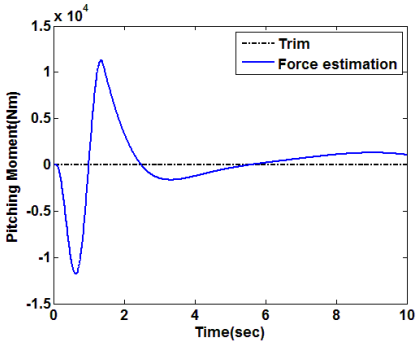

(b) Pitching moment

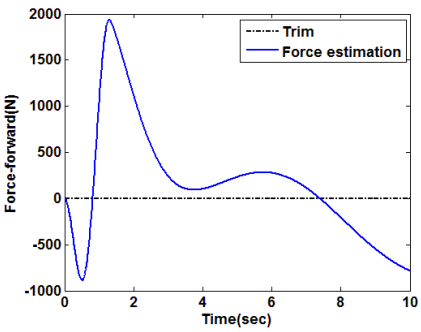

(c) Forward force

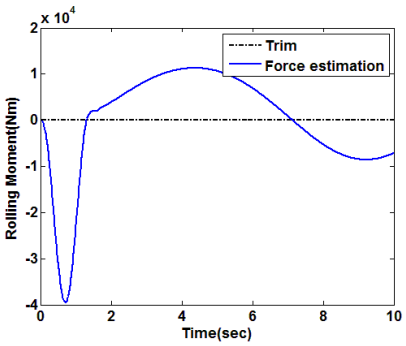

(d) Rolling moment

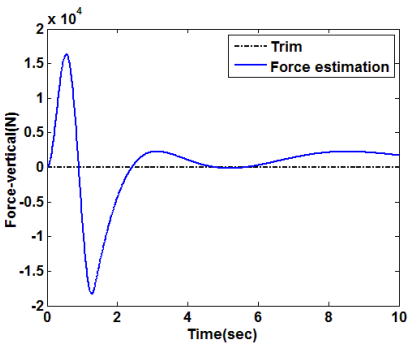

(e) Vertical force

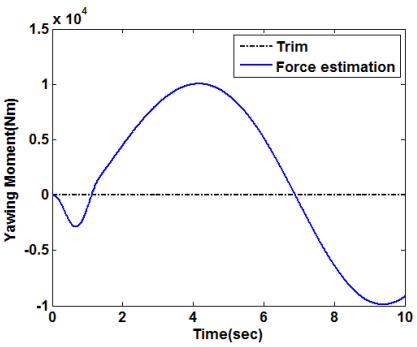

(f) Yawing moment

Figure 4.6. Force estimation at the aircraft reference point

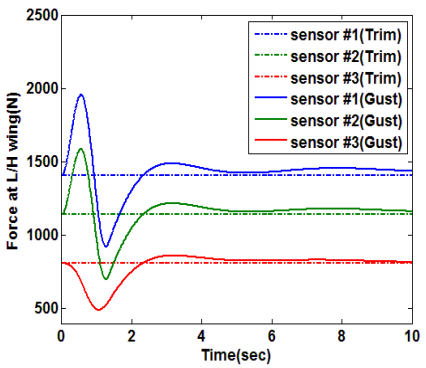

(a) Force at L/H wing

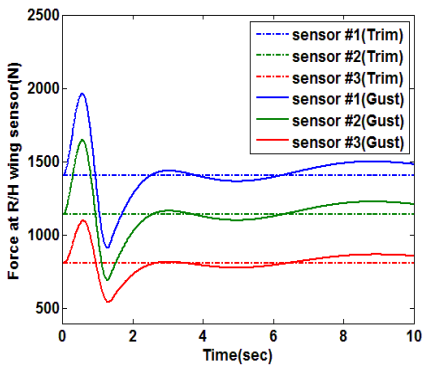

(b) Force at R/H wing sensor

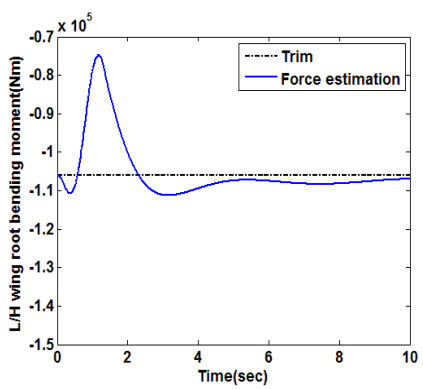

(c) L/H wing root bending moment

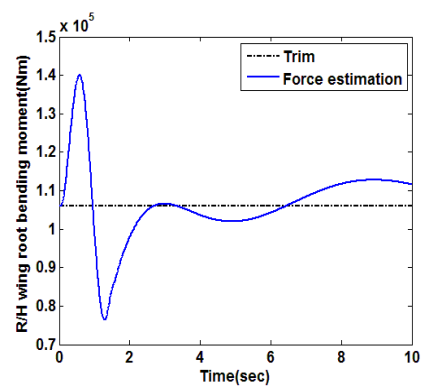

(d) R/H wing root bending moment

Figure 4.7. Force estimation at main wing

5. REDUCED ORDER MODEL FOR FLEXIBLE AIRCRAFT

To increase the efficiency of FFRF simulations, a reduced number of elastic degrees of freedom is required if a solution to be obtained with a reasonable amount of computer time. Sub-structuring, component mode synthesis (CMS) and techniques have been used extensively in structural dynamics, SVD-based reduction with Gramian matrices are applied directly to these second order systems [59-62]. In this chapter, the reduced order model (ROM) based on proper orthogonal decomposition (POD) is presented. This ROM is improved by using surrogate model which is obtained by neural network training.

5.1. ROM using POD

As shown in chap.2.2. FFRF equations of motion can be written a matrix form as

$$\mathbf{M}^i\ddot{\mathbf{q}}^i + \mathbf{K}^i\mathbf{q}^i = \mathbf{Q}_e^i + \mathbf{Q}_v^i \tag{5.1}$$

The generalized coordinates of body *i* that can be written in a partitioned form as

$$\mathbf{q}^i = \begin{bmatrix} \mathbf{q}_r^{iT} & \mathbf{q}_f^{iT} \end{bmatrix}^T \tag{5.2}$$

where $\mathbf{q}_r^i = \begin{bmatrix} \mathbf{R}^{iT} & \boldsymbol{\theta}^{iT} \end{bmatrix}^T$ is the vector of reference coordinates and $\mathbf{q}_f^i$ is the vector of nodal coordinates resulting from finite element discretization. The equations of motion of the deformable body *i* can be written as

$$\begin{bmatrix} \mathbf{m}_{rr}^i & \mathbf{m}_{rf}^i \\ \mathbf{m}_{fr}^i & \mathbf{m}_{ff}^i \end{bmatrix} \begin{bmatrix} \ddot{\mathbf{q}}_r^i \\ \ddot{\mathbf{q}}_f^i \end{bmatrix} + \begin{bmatrix} \mathbf{0} & \mathbf{0} \\ \mathbf{0} & \mathbf{K}_{ff}^i \end{bmatrix} \begin{bmatrix} \mathbf{q}_r^i \\ \mathbf{q}_f^i \end{bmatrix} = \begin{bmatrix} \left(\mathbf{Q}_e^i\right)_r \\ \left(\mathbf{Q}_e^i\right)_f \end{bmatrix} + \begin{bmatrix} \left(\mathbf{Q}_v^i\right)_r \\ \left(\mathbf{Q}_v^i\right)_f \end{bmatrix} \tag{5.3}$$

where subscripts *r* and *f* refer to reference and elastic coordinates, respectively, and $\mathbf{m}_{fr}^{i} = \left(\mathbf{m}_{rf}^{i}\right)^{T}$. If the body I is assumed to vibrate freely, Eqn. (5.3) yields

$$\mathbf{m}_{ff}^{i}\ddot{\mathbf{q}}_{f}^{i} + \mathbf{K}_{ff}^{i}\mathbf{q}_{f}^{i} = \mathbf{0} \tag{5.4}$$

The stiffness matrix $\mathbf{K}_{ff}^{i}$ is positive definite, because of imposing the reference conditions that define a unique displacement field. A reduced order model can be achieved by solving for only a few node shapes. A coordinate transformation from the physical nodal coordinates to the modal elastic coordinates can be obtained as

$$\mathbf{q}_{f}^{i} = \overline{\mathbf{B}}_{m}^{i}\mathbf{p}_{f}^{i} \tag{5.5}$$

where $\overline{\mathbf{B}}_{m}^{i}$ is the nodal transformation matrix which columns are the low-frequency mode shapes. Using eqn. (5.5), the reference and elastic generalized coordinates are written as

$$\begin{bmatrix} \mathbf{q}_{r}^{i} \\ \mathbf{q}_{f}^{i} \end{bmatrix} = \begin{bmatrix} \mathbf{I} & \mathbf{0} \\ \mathbf{0} & \overline{\mathbf{B}}_{m}^{i} \end{bmatrix} \begin{bmatrix} \mathbf{p}_{r}^{i} \\ \mathbf{p}_{f}^{i} \end{bmatrix} \tag{5.6}$$

So, the equations of motion can be expressed as follow:

$$\begin{bmatrix} \mathbf{m}_{rr}^{i} & \mathbf{m}_{rf}^{i}\overline{\mathbf{B}}_{m}^{i} \\ \left(\mathbf{m}_{rf}^{i}\overline{\mathbf{B}}_{m}^{i}\right)^{T} & \overline{\mathbf{B}}_{m}^{i\,T}\overline{\mathbf{m}}_{ff}^{i}\overline{\mathbf{B}}_{m}^{i} \end{bmatrix} \begin{bmatrix} \ddot{\mathbf{p}}_{r}^{i} \\ \ddot{\mathbf{p}}_{f}^{i} \end{bmatrix} + \begin{bmatrix} \mathbf{0} & \mathbf{0} \\ \mathbf{0} & \overline{\mathbf{B}}_{m}^{i\,T}\overline{\mathbf{K}}_{ff}^{i}\overline{\mathbf{B}}_{m}^{i} \end{bmatrix} \begin{bmatrix} \mathbf{p}_{r}^{i} \\ \mathbf{p}_{f}^{i} \end{bmatrix} = \begin{bmatrix} \left(\mathbf{Q}_{e}^{i}\right)_{r} \\ \overline{\mathbf{B}}_{m}^{i\,T}\left(\overline{\mathbf{Q}}_{e}^{i}\right)_{f} \end{bmatrix} + \begin{bmatrix} \left(\mathbf{Q}_{v}^{i}\right)_{r} \\ \overline{\mathbf{B}}_{m}^{i\,T}\left(\overline{\mathbf{Q}}_{v}^{i}\right)_{f} \end{bmatrix} \tag{5.7}$$

In this study, the POD is used to compose the nodal transformation matrix $\overline{\mathbf{B}}_{m}^{i}$. It is known that the POD method yields the best representation of given data sets. The proper orthogonal modes obtained from the POD process are the orthogonal bases for forming the reduced coordinates. The reduction modes are extracted from the displacement data sets stored in chap.2.5 uniform gust cases. If the number of

degrees of freedom exceeds the number of sampling sets, the method of snapshots can be used. For a more detailed explanation, check references [63, 64].

First of all, the performance of the ROM was verified by comparing time responses of the FOM (full order model) and the ROM. The nodal transformation matrix is constructed using six POM (proper orthogonal mode) which is based on the analysis result of using uniform gust parameters as $H = 50, F_g = 0.5$. Using this one case analysis, the POM can be constructed. The total degree of freedom is reduced from 496 to 12 (about 2.42%).

The aircraft is flying 75 m/s in a trim state at 10,000m, and gust parameters are $H = 60, F_g = 0.7$. The trajectory and response of FOM and ROM are shown Fig.5.1 and Fig.5.2. ROM result is similar to FOM results which max difference about vertical position is under 10^{-4}m. Analysis time is reduced from 229.4 sec to 105.3 sec (about 45.9%).

5.2. ROM using POD with Surrogate Model Based on Neural Network

This section describes the development of a surrogate model for obtaining reduced force terms, which is eqn.(5.7) right-hand side. This term consists of gravity, quadratic velocity term, thrust and aerodynamics with gust.

A surrogate model is developed for the nonlinear relationship among aircraft response—aircraft attitude, velocity, deformation—gust velocity and force. In particular, a supervised NN (surrogate model) is considered due to rapid prediction capabilities amenable to real-time applications[65]. In Fig.5.3 and Fig 5.4, the upper dashed region shows the generalized procedure for developing a NN that

predicts updated force as a function of aircraft response and gust velocity. The lower dashed region shows the functionality of the NN in a flight dynamic analysis.

The first step in this type of surrogate model development is typically referred to as design of experiment which is the sampling plan in design variable space[40]. Each data point includes input variable(s) and corresponding known system response(s), called target output. Once the NN has been trained to map the given input to the target output, it becomes a useful tool for predicting system response when presented with new input that is within the training range.

To illustrate the methodology, force matrix is a function of structure response and gust velocity as follow

$$\bar{\mathbf{Q}}^i = fn\left(\dot{\mathbf{p}}^i, \mathbf{p}^i, U_{gust}\right) \tag{5.8}$$

where $\bar{\mathbf{Q}}^i$ is the reduced force matrix. The training data sets are the response using gust parameter 48 cases which are selected within gust parameter ranges as shown Fig.5.5. Neural Network is constructed through a feedforward NN with a backpropagation learning rule, which is a commonly used type of supervised NN, is constructed using MATLAB [66]. Weights and biases of the NN are adjusted at each iteration, or epoch, using the training set and a Levenberg–Marquardt optimization algorithm, as described in [67]. The NN performance metric used here is the mean-squared error (mse), calculated as

$$mse^{(i)} = \frac{1}{Q^{(i)}} \sum_{k=1}^{Q^{(i)}} \left(t_k^{(i)} - p_k\right)^2 \tag{5.9}$$

where the superscript *(i)* corresponds to the training, validation, or test set; Q is the number of data points in the respective set; t_k is target output for the *k*-th input; and p_k is output predicted by the NN for the same *k*-th input. The NN is

trained by using the number of neurons in the hidden layer 25 and size of the training set 70% of the available data as shown Fig. 5.6.

The aircraft is flying 75 m/s in a trim state at 10,000m, and gust parameters are $H = 60, F_g = 0.7$ as same as previous section. The trajectory and response of FOM and ROM with surrogate model are shown Fig.5.7 and Fig.5.8. ROM with surrogate model result is similar to FOM results which max difference about vertical position is under 10^{-3}m. Analysis time is reduced from 229.4 sec to 15.7 sec (about 6.8%).

To construct surrogate model, some analysis results are used. As the responses are more complex, the many results are used and/or hidden layer neurons are adjusted for surrogate model precisions increasing and preventing overfitting. This leads that the construction time for surrogate model, off-line analysis, is increased. Once the surrogate model is constructed, the calculation process can be removed, which makes the real-time analysis. This process can be performed based on real-measurement data.

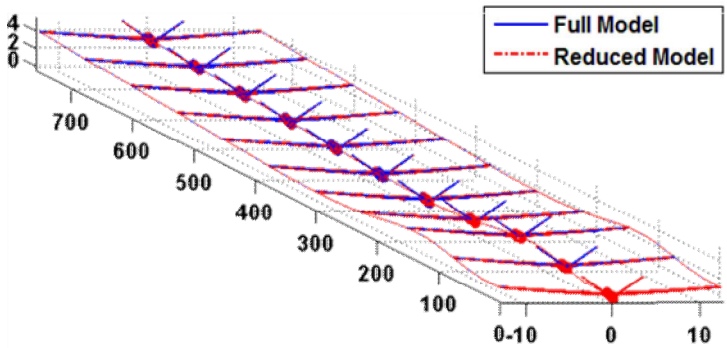

Figure 5.1. Trajectory of full model and reduced order model

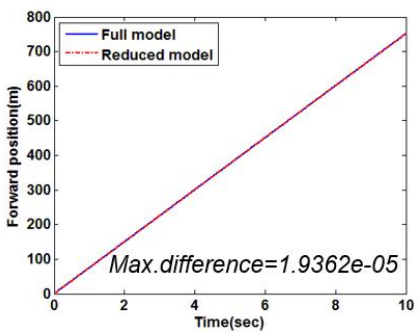

(a) Forward position

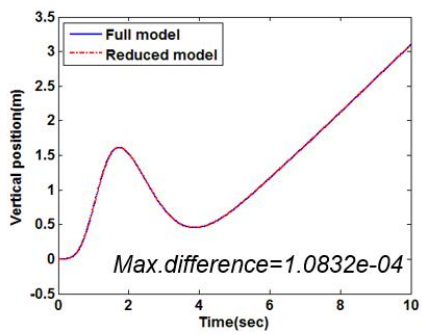

(b) Vertical positon

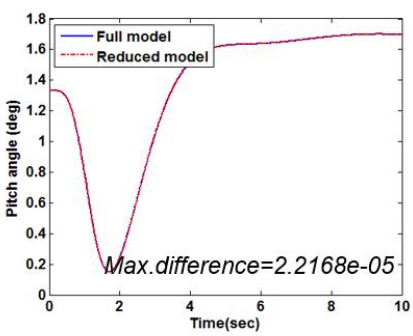

(c) Pitch angle

Figure 5.2. Flight dynamic response for full model and reduced order model

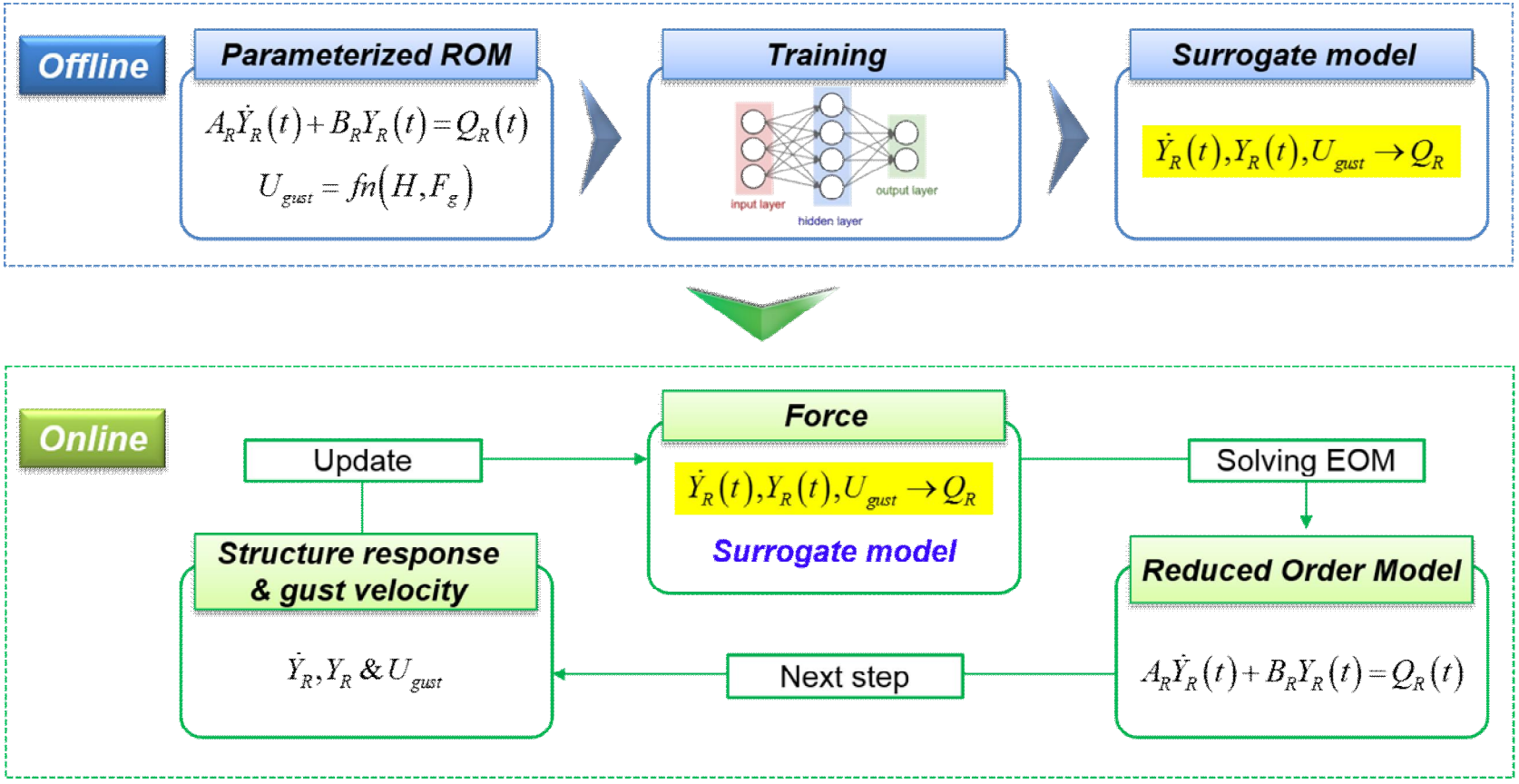

Figure 5.3. Developing surrogate for prediction updated force

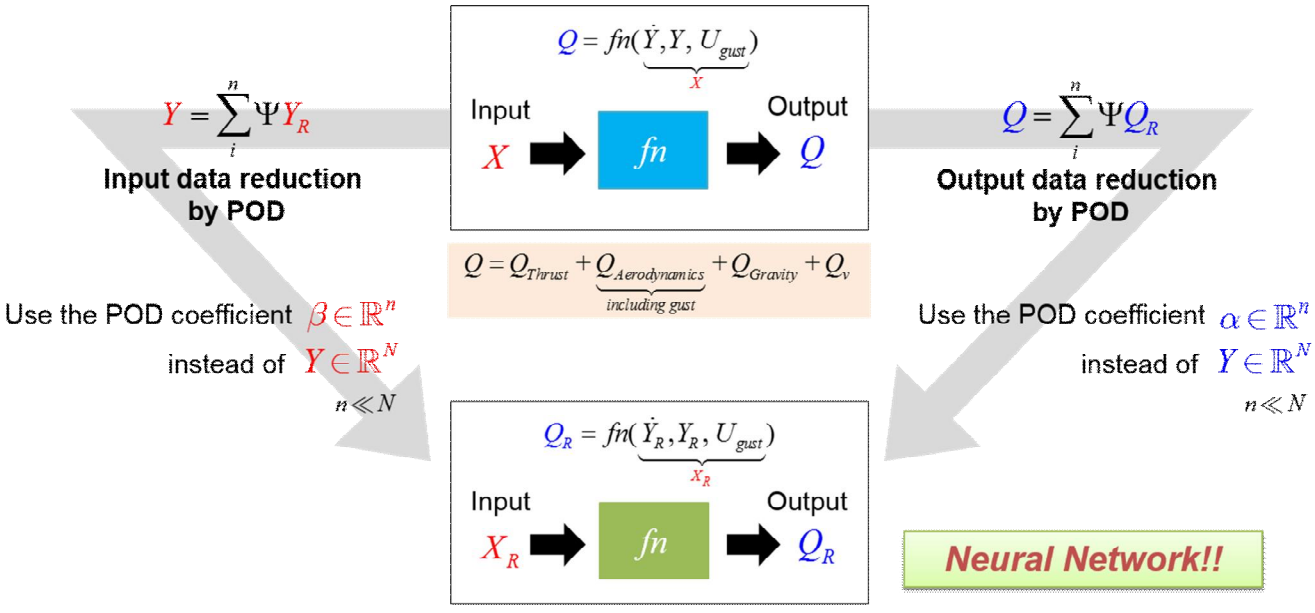

Figure 5.4. Detail of construction surrogate model

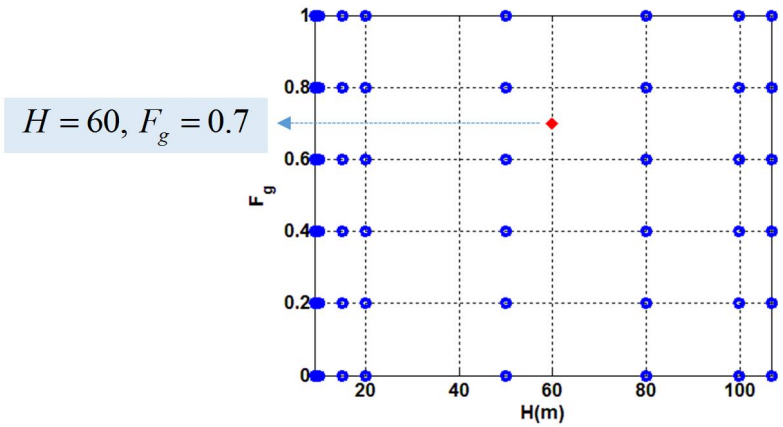

· H = [9, 10, 15, 20, 50, 80, 100, 107]

· Fg= [0, 0.2, 0.4, 0.6, 0.8, 1.0]

Figure 5.5. Training data gust parameters

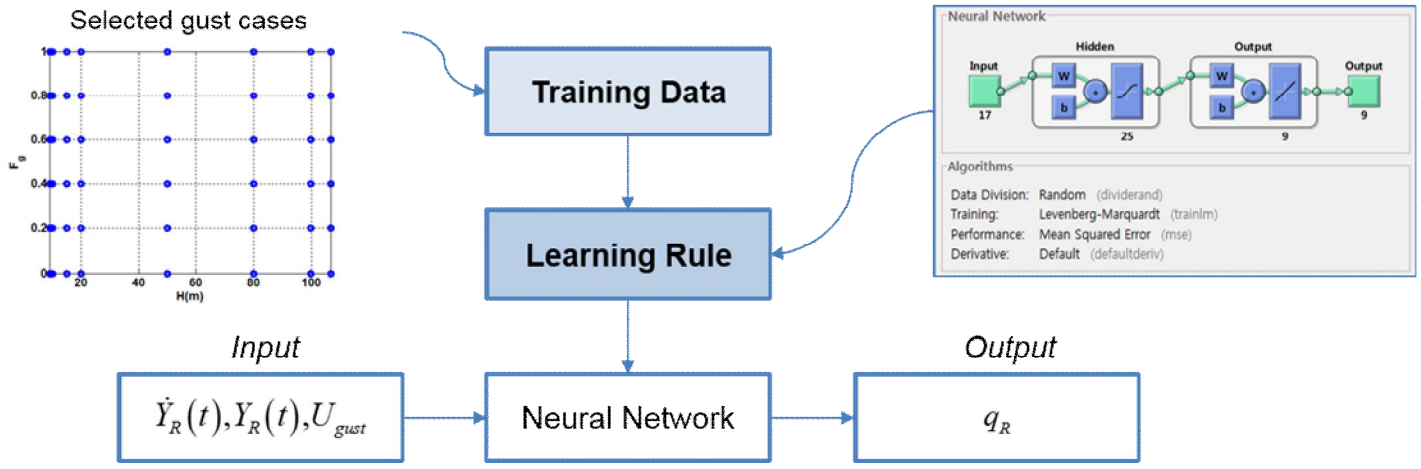

Figure 5.6. Neural Network training

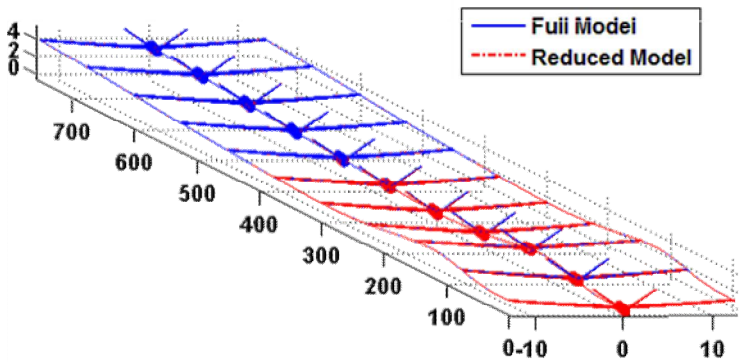

Figure 5.7. Trajectory of full model and reduced order model

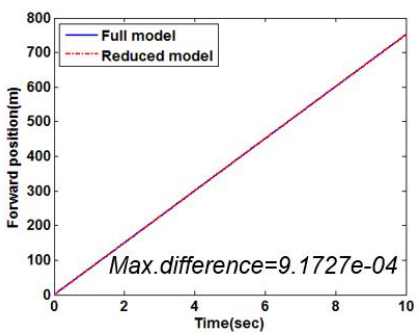

(a) Forward position

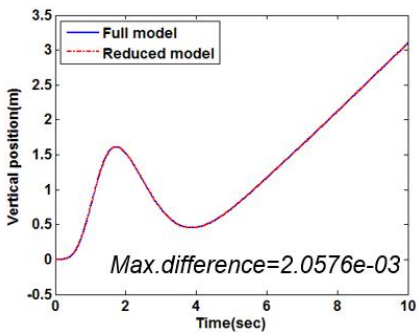

(b) Vertical positon

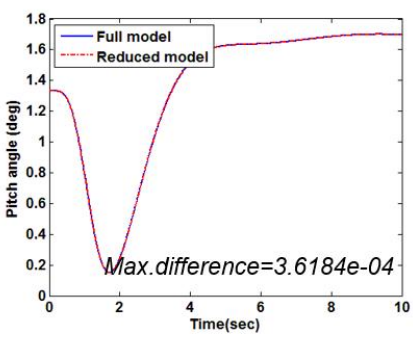

(c) Pitch angle

Figure 5.8. Flight dynamic response for full model and reduced order model

6. CONCLUSION

This research presents a flexible aircraft flight dynamics framework based on floating frame of reference formulation and finite inflow theory. Using this framework, the flexible aircraft trim analysis is conducted through optimization. The flexible aircraft flight dynamics responses are compared with rigid body aircraft response considering control surface input case. Also, '1-cosine' gust model is mounted aerodynamic to reflect the gust effect.

The gust effect for flexible aircraft is evaluated by comparing with quasi-static method (Pratt method) which is one of the low-cost and useful mean to determine gust loads and basis on Federal Aviation Regulation Part 23 gust loads certification requirements. Through this process, the critical gust for flexible aircraft can be determined which might use to estimate aircraft structural integrity.

To reconstruct the flight loads using restrict available flight test data, the optimization process is conducted which is based on inverse problem theory. Considering flight test, the limited responses are used and the aircraft model is under free-free condition. The identified gust is well matched to reference gust. Using this identified gust, the flight load can be reconstructed for all degree-of-freedom.

For reducing the computation time, reduced order model is composed which is based on proper orthogonal decomposition method. This reduced model is improved using surrogate model which is constructed neural network. The aircraft response and gust velocity are used as input and the output is force matrix which is

composed of gravity, aerodynamics with gust, thrust and quadratic velocity vector.

Based on these framework for six-degrees-of-freedom flexible aircraft flight dynamics can be performed considering gust. The framework can be improved if the model calibration is performed using wind tunnel test with gust generation facility and/or flight test data. It is hoped that this framework can be further employed to estimate and evaluate the flexible aircraft development and maintaining.

APPENDIX. A. CENTRIFUGAL AND CORIOLIS INERTIA FORCES EFFECT

In this section, the derivation of the quadratic velocity vectors that appear in chap.2 is presented. The Euler parameters are used as the orientation coordinates. The kinetic energy of the deformable body can be written as

$$T = \frac{1}{2}\left(\dot{\mathbf{R}}^T \mathbf{m}_{RR}\dot{\mathbf{R}} + 2\dot{\mathbf{R}}^T \mathbf{m}_{R\theta}\dot{\boldsymbol{\theta}} + 2\dot{\mathbf{R}}^T \mathbf{m}_{Rf}\dot{\mathbf{q}}_f + \dot{\boldsymbol{\theta}}^T \mathbf{m}_{\theta\theta}\dot{\boldsymbol{\theta}} + 2\dot{\boldsymbol{\theta}}^T \mathbf{m}_{\theta f}\dot{\mathbf{q}}_f + \dot{\mathbf{q}}_f{}^T \mathbf{m}_{ff}\dot{\mathbf{q}}_f\right) \tag{A.1}$$

The expression of the kinetic energy of Eq. (A.1) is used in this section to define the vectors $\left(\mathbf{Q}_v\right)_R$, $\left(\mathbf{Q}_v\right)_\theta$ and $\left(\mathbf{Q}_v\right)_f$. The detailed derivation is following, respectively.

Vector $\left(\mathbf{Q}_v\right)_R$: Using Eq. (A.1), one can show that $\left(\partial T/\partial \mathbf{R}\right) = \mathbf{0}$. Which leads to

$$\left(\frac{\partial T}{\partial \mathbf{R}}\right)^T = \mathbf{m}_{RR}\dot{\mathbf{R}} + \mathbf{m}_{R\theta}\dot{\boldsymbol{\theta}} + \mathbf{m}_{Rf}\dot{\mathbf{q}}_f \tag{A.2}$$

It is follows that

$$\frac{d}{dt}\left(\frac{\partial T}{\partial \mathbf{R}}\right)^T = \mathbf{m}_{RR}\ddot{\mathbf{R}} + \mathbf{m}_{R\theta}\ddot{\boldsymbol{\theta}} + \dot{\mathbf{m}}_{R\theta}\dot{\boldsymbol{\theta}} + \mathbf{m}_{Rf}\ddot{\mathbf{q}}_f + \dot{\mathbf{m}}_{Rf}\dot{\mathbf{q}}_f \tag{A.3}$$

Using this equation, the $\left(\mathbf{Q}_v\right)_R$ can be recognized as

$$\left(\mathbf{Q}_v\right)_R = -\left(\dot{\mathbf{m}}_{R\theta}\dot{\boldsymbol{\theta}} + \dot{\mathbf{m}}_{Rf}\dot{\mathbf{q}}_f\right) \tag{A.4}$$

The $\dot{\mathbf{m}}_{R\theta}\dot{\boldsymbol{\theta}}$ can be expressed as

$$\dot{\mathbf{m}}_{R\theta}\dot{\boldsymbol{\theta}} = -\frac{d}{dt}\left(\mathbf{A}\int_V \rho\tilde{\bar{\mathbf{u}}}dV\bar{\mathbf{G}}\right)\dot{\boldsymbol{\theta}} = -\dot{\mathbf{A}}\int_V \rho\tilde{\bar{\mathbf{u}}}dV\bar{\mathbf{G}}\dot{\boldsymbol{\theta}} - \mathbf{A}\int_V \rho\dot{\tilde{\bar{\mathbf{u}}}}dV\bar{\mathbf{G}}\dot{\boldsymbol{\theta}}$$
$$= \mathbf{A}\tilde{\bar{\boldsymbol{\omega}}}\int_V \rho\tilde{\bar{\mathbf{u}}}dV\bar{\boldsymbol{\omega}} - \mathbf{A}\int_V \rho\dot{\tilde{\bar{\mathbf{u}}}}dV\bar{\boldsymbol{\omega}} = \mathbf{A}\left(\tilde{\bar{\boldsymbol{\omega}}}\right)^2\bar{\mathbf{S}}_t + \mathbf{A}\tilde{\bar{\boldsymbol{\omega}}}\bar{\mathbf{S}}\dot{\mathbf{q}}_f \tag{A.5}$$

where $\bar{\mathbf{u}}$ is the position vector of an arbitrary point on the deformable body, $\mathbf{A}$ is the transformation matrix, $\bar{\boldsymbol{\omega}}$ is the angular velocity vector, $\bar{\mathbf{S}}_t = \int_V \rho\bar{\mathbf{u}}dV$, $\bar{\mathbf{S}} = \int_V \rho\mathbf{S}dV$, $\mathbf{S}$ is the shape function matrix, V is the volume, and ρ is the mass density. The general identity $\dot{\mathbf{A}} = \mathbf{A}\tilde{\bar{\boldsymbol{\omega}}}$ and the Euler parameter identity $\dot{\bar{\mathbf{G}}}\dot{\boldsymbol{\theta}} = \mathbf{0}$ are utilized. $\dot{\mathbf{m}}_{Rf}\dot{\mathbf{q}}_f$ can be expressed as

$$\dot{\mathbf{m}}_{Rf}\dot{\mathbf{q}}_f = -\frac{d}{dt}\left(\mathbf{A}\int_V \rho\mathbf{S}dV\right)\dot{\mathbf{q}}_f = -\mathbf{A}\tilde{\bar{\boldsymbol{\omega}}}\bar{\mathbf{S}}\dot{\mathbf{q}}_f \tag{A.6}$$

Using above equations, one can show that the vector $\left(\mathbf{Q}_v\right)_R$ can be written as

$$\left(\mathbf{Q}_v\right)_R = -\left(\dot{\mathbf{m}}_{R\theta}\dot{\boldsymbol{\theta}} + \dot{\mathbf{m}}_{Rf}\dot{\mathbf{q}}_f\right) = -\mathbf{A}\left(\left(\tilde{\bar{\boldsymbol{\omega}}}\right)^2\bar{\mathbf{S}}_t + 2\tilde{\bar{\boldsymbol{\omega}}}\bar{\mathbf{S}}\dot{\mathbf{q}}_f\right) \tag{A.7}$$

Vector $\left(\mathbf{Q}_v\right)_\theta$: Using Eq. (A.1) and the fact that $\mathbf{m}_{\theta R} = \mathbf{m}_{R\theta}^T$, one can write

$$\left(\frac{\partial T}{\partial\dot{\boldsymbol{\theta}}}\right)^T = \mathbf{m}_{\theta R}\dot{\mathbf{R}} + \mathbf{m}_{\theta\theta}\dot{\boldsymbol{\theta}} + \mathbf{m}_{\theta f}\dot{\mathbf{q}}_f \tag{A.8}$$

It follows that

$$\frac{d}{dt}\left(\frac{\partial T}{\partial\dot{\boldsymbol{\theta}}}\right)^T = \mathbf{m}_{\theta R}\ddot{\mathbf{R}} + \dot{\mathbf{m}}_{\theta R}\dot{\mathbf{R}} + \mathbf{m}_{\theta\theta}\ddot{\boldsymbol{\theta}} + \dot{\mathbf{m}}_{\theta\theta}\dot{\boldsymbol{\theta}} + \mathbf{m}_{\theta f}\ddot{\mathbf{q}}_f + \dot{\mathbf{m}}_{\theta f}\dot{\mathbf{q}}_f \tag{A.9}$$

The use of Eq. (1) also leads to

$$\frac{\partial T}{\partial\boldsymbol{\theta}} = \frac{\partial}{\partial\boldsymbol{\theta}}\left(\dot{\mathbf{R}}^T\mathbf{m}_{R\theta}\dot{\boldsymbol{\theta}} + \dot{\mathbf{R}}^T\mathbf{m}_{Rf}\dot{\mathbf{q}}_f + \frac{1}{2}\dot{\boldsymbol{\theta}}^T\mathbf{m}_{\theta\theta}\dot{\boldsymbol{\theta}} + \dot{\boldsymbol{\theta}}^T\mathbf{m}_{\theta f}\dot{\mathbf{q}}_f\right) \tag{A.10}$$

Using the preceding two equations, the vector $\left(\mathbf{Q}_v\right)_\theta$ can be defined as

$$\left(\mathbf{Q}_v\right)_\theta = -\left(\mathbf{m}_{\theta R}\dot{\mathbf{R}} + \mathbf{m}_{\theta\theta}\dot{\boldsymbol{\theta}} + \mathbf{m}_{\theta f}\dot{\mathbf{q}}_f\right) + \left(\frac{\partial}{\partial\boldsymbol{\theta}}\left(\dot{\mathbf{R}}^T\mathbf{m}_{R\theta}\dot{\boldsymbol{\theta}} + \dot{\mathbf{R}}^T\mathbf{m}_{Rf}\dot{\mathbf{q}}_f + \frac{1}{2}\dot{\boldsymbol{\theta}}^T\mathbf{m}_{\theta\theta}\dot{\boldsymbol{\theta}} + \dot{\boldsymbol{\theta}}^T\mathbf{m}_{\theta f}\dot{\mathbf{q}}_f\right)\right)^T \tag{A.11}$$

This equation cab be reduced to

$$\left(\mathbf{Q}_v\right)_\theta = -\left(\mathbf{m}_{\theta\theta}\dot{\boldsymbol{\theta}} + \mathbf{m}_{\theta f}\dot{\mathbf{q}}_f\right) + \left(\frac{\partial}{\partial\boldsymbol{\theta}}\left(\frac{1}{2}\dot{\boldsymbol{\theta}}^T\mathbf{m}_{\theta\theta}\dot{\boldsymbol{\theta}} + \dot{\boldsymbol{\theta}}^T\mathbf{m}_{\theta f}\dot{\mathbf{q}}_f\right)\right)^T \tag{A.12}$$

$$\mathbf{m}_{\theta R}\dot{\mathbf{R}} = \left(\partial \big/ \partial\boldsymbol{\theta}\left(\dot{\mathbf{R}}^T\mathbf{m}_{R\theta}\dot{\boldsymbol{\theta}} + \dot{\mathbf{R}}^T\mathbf{m}_{Rf}\dot{\mathbf{q}}_f\right)\right)^T \tag{A.13}$$

The each terms can be express as

$$\left(\mathbf{Q}_v\right)_\theta = -\left(\mathbf{m}_{\theta\theta}\dot{\boldsymbol{\theta}} + \mathbf{m}_{\theta f}\dot{\mathbf{q}}_f\right) + \left(\frac{\partial}{\partial\boldsymbol{\theta}}\left(\frac{1}{2}\dot{\boldsymbol{\theta}}^T\mathbf{m}_{\theta\theta}\dot{\boldsymbol{\theta}} + \dot{\boldsymbol{\theta}}^T\mathbf{m}_{\theta f}\dot{\mathbf{q}}_f\right)\right)^T \tag{A.14}$$

One can show that

$$\begin{aligned} &\mathbf{m}_{\theta\theta}\dot{\boldsymbol{\theta}} = \dot{\bar{\mathbf{G}}}^T\bar{\mathbf{I}}_{\theta\theta}\bar{\omega} + \bar{\mathbf{G}}^T\dot{\bar{\mathbf{I}}}_{\theta\theta}\bar{\omega}, \quad \mathbf{m}_{\theta f}\dot{\mathbf{q}}_f = \dot{\bar{\mathbf{G}}}^T\bar{\mathbf{I}}_{\theta f}\dot{\mathbf{q}}_f, \\ &\frac{\partial}{\partial\boldsymbol{\theta}}\left(\frac{1}{2}\dot{\boldsymbol{\theta}}^T\mathbf{m}_{\theta\theta}\dot{\boldsymbol{\theta}}\right) = -\dot{\bar{\mathbf{G}}}^T\bar{\mathbf{I}}_{\theta\theta}\bar{\omega}, \quad \frac{\partial}{\partial\boldsymbol{\theta}}\left(\dot{\boldsymbol{\theta}}^T\mathbf{m}_{\theta f}\dot{\mathbf{q}}_f\right) = -\dot{\bar{\mathbf{G}}}^T\bar{\mathbf{I}}_{\theta f}\dot{\mathbf{q}}_f \end{aligned} \tag{A.15}$$

The identity $\dot{\bar{\mathbf{I}}}_{\theta f}\dot{\mathbf{q}}_f = \mathbf{0}$ and the Euler parameters identities $\dot{\bar{\mathbf{G}}}\dot{\boldsymbol{\theta}} = \mathbf{0}$, and $\bar{\mathbf{G}}\dot{\boldsymbol{\theta}} = -\dot{\bar{\mathbf{G}}}\boldsymbol{\theta}$ are utilized. The vector $\left(\mathbf{Q}_v\right)_\theta$ can be obtained as

$$\left(\mathbf{Q}_v\right)_\theta = 2\dot{\bar{\mathbf{G}}}^T\bar{\mathbf{I}}_{\theta\theta}\bar{\omega} - \bar{\mathbf{G}}^T\dot{\bar{\mathbf{I}}}_{\theta\theta}\bar{\omega} - 2\dot{\bar{\mathbf{G}}}^T\bar{\mathbf{I}}_{\theta f}\dot{\mathbf{q}}_f \tag{A.16}$$

Vector $\left(\mathbf{Q}_v\right)_f$: Eq. (A.1) is used to write

$$\left(\frac{\partial T}{\partial\dot{\mathbf{q}}_f}\right)^T = \mathbf{m}_{fR}\dot{\mathbf{R}} + \mathbf{m}_{f\theta}\dot{\boldsymbol{\theta}} + \mathbf{m}_{ff}\dot{\mathbf{q}}_f \tag{A.17}$$

It follows that

$$\frac{d}{dt}\left(\frac{\partial T}{\partial\dot{\mathbf{q}}_f}\right)^T = \mathbf{m}_{fR}\ddot{\mathbf{R}} + \dot{\mathbf{m}}_{fR}\dot{\mathbf{R}} + \mathbf{m}_{f\theta}\ddot{\boldsymbol{\theta}} + \dot{\mathbf{m}}_{f\theta}\dot{\boldsymbol{\theta}} + \mathbf{m}_{ff}\ddot{\mathbf{q}}_f \tag{A.18}$$

$$\left(\frac{\partial T}{\partial \mathbf{q}_f}\right)^T = \frac{\partial}{\partial \mathbf{q}_f}\left(\dot{\mathbf{R}}^T \mathbf{m}_{R\theta}\dot{\boldsymbol{\theta}} + \frac{1}{2}\dot{\boldsymbol{\theta}}^T \mathbf{m}_{\theta\theta}\dot{\boldsymbol{\theta}} + \dot{\boldsymbol{\theta}}^T \mathbf{m}_{\theta f}\dot{\mathbf{q}}_f\right) \tag{A.19}$$

Using above equations, the vector $\left(\mathbf{Q}_v\right)_f$ can be recognized as

$$\left(\mathbf{Q}_v\right)_f = -\left(\dot{\mathbf{m}}_{fR}\dot{\mathbf{R}} + \dot{\mathbf{m}}_{f\theta}\dot{\boldsymbol{\theta}}\right) + \left(\frac{\partial}{\partial \mathbf{q}_f}\left(\dot{\mathbf{R}}^T \mathbf{m}_{R\theta}\dot{\boldsymbol{\theta}} + \frac{1}{2}\dot{\boldsymbol{\theta}}^T \mathbf{m}_{\theta\theta}\dot{\boldsymbol{\theta}} + \dot{\boldsymbol{\theta}}^T \mathbf{m}_{\theta f}\dot{\mathbf{q}}_f\right)\right)^T \tag{A.20}$$

This equation cab be reduced to

$$\left(\mathbf{Q}_v\right)_f = -\dot{\mathbf{m}}_{f\theta}\dot{\boldsymbol{\theta}} + \left(\frac{\partial}{\partial \mathbf{q}_f}\left(\frac{1}{2}\dot{\boldsymbol{\theta}}^T \mathbf{m}_{\theta\theta}\dot{\boldsymbol{\theta}} + \dot{\boldsymbol{\theta}}^T \mathbf{m}_{\theta f}\dot{\mathbf{q}}_f\right)\right)^T \tag{A.21}$$

$$\dot{\mathbf{m}}_{fR}\dot{\mathbf{R}} = \left(\partial \big/ \partial \mathbf{q}_f \left(\dot{\mathbf{R}}^T \mathbf{m}_{R\theta}\dot{\boldsymbol{\theta}}\right)\right)^T \tag{A.22}$$

One can show that

$$\dot{\mathbf{m}}_{f\theta}\dot{\boldsymbol{\theta}} = \left(-\left[\int_V \rho \mathbf{S}^T \tilde{\bar{\mathbf{u}}} dV\right]\bar{\mathbf{G}}\right)\dot{\boldsymbol{\theta}} = \int_V \rho \mathbf{S}^T \tilde{\bar{\boldsymbol{\omega}}}\dot{\bar{\mathbf{u}}} dV \tag{A.23}$$

$$\begin{aligned}\left(\frac{\partial}{\partial \mathbf{q}_f}\left(\dot{\boldsymbol{\theta}}^T \mathbf{m}_{\theta f}\dot{\mathbf{q}}_f\right)\right)^T &= \left(\frac{\partial}{\partial \mathbf{q}_f}\left(\dot{\boldsymbol{\theta}}^T\left[\bar{\mathbf{G}}^T \int_V \rho \tilde{\bar{\mathbf{u}}}\mathbf{S} dV\right]\dot{\mathbf{q}}_f\right)\right)^T \\ &= -\left(\frac{\partial}{\partial \mathbf{q}_f}\left(\bar{\boldsymbol{\omega}}^T\left[\int_V \rho \dot{\tilde{\bar{\mathbf{u}}}}\bar{\mathbf{u}} dV\right]\right)\right)^T = -\int_V \rho \mathbf{S}^T \tilde{\bar{\boldsymbol{\omega}}}\dot{\bar{\mathbf{u}}} dV\end{aligned} \tag{A.24}$$

$$\begin{aligned}\left(\frac{\partial}{\partial \mathbf{q}_f}\left(\frac{1}{2}\dot{\boldsymbol{\theta}}^T \mathbf{m}_{\theta\theta}\dot{\boldsymbol{\theta}}\right)\right)^T &= \left(\frac{\partial}{\partial \mathbf{q}_f}\left(\frac{1}{2}\bar{\boldsymbol{\omega}}^T \bar{\mathbf{I}}_{\theta\theta}\bar{\boldsymbol{\omega}}\right)\right)^T \\ &= \left(\frac{\partial}{\partial \mathbf{q}_f}\left(\frac{1}{2}\bar{\boldsymbol{\omega}}^T\left[\int_V \rho \tilde{\bar{\mathbf{u}}}^T \tilde{\bar{\mathbf{u}}} dV\right]\bar{\boldsymbol{\omega}}\right)\right)^T = -\int_V \rho \mathbf{S}^T\left(\tilde{\bar{\boldsymbol{\omega}}}\right)^2 \bar{\mathbf{u}} dV\end{aligned}$$

(A.25)

Using the result of above equations, The vector $\left(\mathbf{Q}_v\right)_f$ can be defined as

$$\left(\mathbf{Q}_v\right)_f = -\int_V \rho \mathbf{S}^T\left[\left(\tilde{\bar{\boldsymbol{\omega}}}\right)^2 \bar{\mathbf{u}} + 2\tilde{\bar{\boldsymbol{\omega}}}\dot{\bar{\mathbf{u}}}\right] dV \tag{A.26}$$

In the case of using another set of orientation parameters such as *Euler angles,* one cannot used the identities such as $\dot{\bar{\mathbf{G}}}\dot{\boldsymbol{\theta}} = \mathbf{0}$. The quadratic vector $\mathbf{Q}_v$ can be written as

$$\mathbf{Q}_v = \begin{bmatrix} (\mathbf{Q}_v)_R \\ (\mathbf{Q}_v)_\theta \\ (\mathbf{Q}_v)_f \end{bmatrix} = \begin{bmatrix} -\mathbf{A}\left(\left(\tilde{\bar{\omega}}\right)^2 \bar{\mathbf{S}}_t + 2\tilde{\bar{\omega}}\bar{\mathbf{S}}\dot{\mathbf{q}}_f - \tilde{\bar{\mathbf{S}}}_t\dot{\bar{\mathbf{G}}}\dot{\boldsymbol{\theta}}\right) \\ -\left(2\dot{\bar{\mathbf{G}}}^T\bar{\mathbf{I}}_{\theta\theta}\bar{\omega} - \bar{\mathbf{G}}^T\dot{\bar{\mathbf{I}}}_{\theta\theta}\bar{\omega} - 2\dot{\bar{\mathbf{G}}}^T\bar{\mathbf{I}}_{\theta f}\dot{\mathbf{q}}_f + \bar{\mathbf{G}}^T\bar{\mathbf{I}}_{\theta\theta}\dot{\bar{\mathbf{G}}}\dot{\boldsymbol{\theta}}\right) \\ -\int_V \rho\mathbf{S}^T\left[\left(\tilde{\bar{\omega}}\right)^2\bar{\mathbf{u}} + 2\tilde{\bar{\omega}}\dot{\bar{\mathbf{u}}}\right]dV - \bar{\mathbf{I}}_{\theta f}^T\dot{\bar{\mathbf{G}}}\dot{\boldsymbol{\theta}} \end{bmatrix} \quad \text{(A.27)}$$

Figure A.1 shows the non-uniform gust and fig.A.2 shows the quadratic velocity vector effect under same gust.

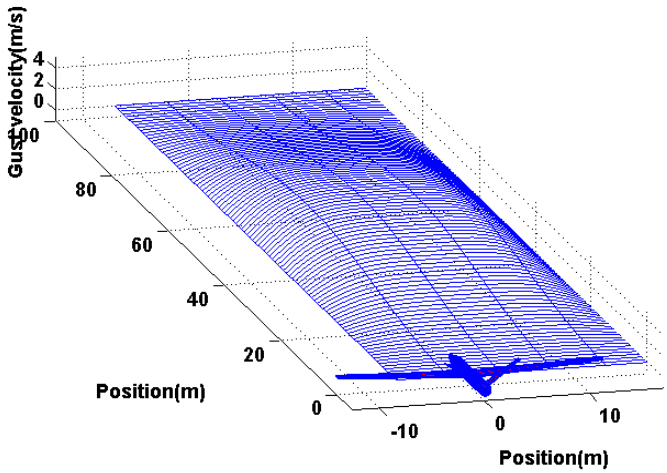

* $H = 50,\ F_g = 0.8,\ r_0 = 12,\ n_E = 2.0,\ G_p = 5$

Figure A.1. Non-uniform gust

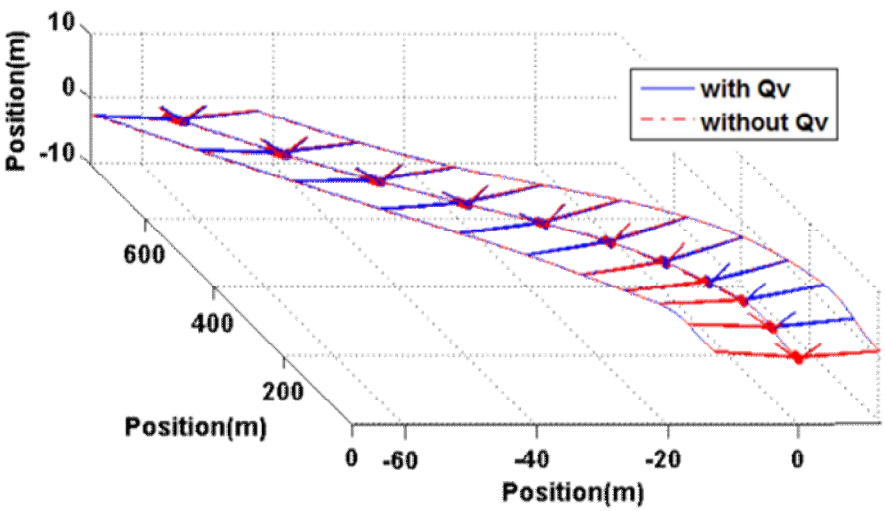

Figure A.2. Trajectory of flexible aircraft under non-uniform gust w/ and w/o Qv

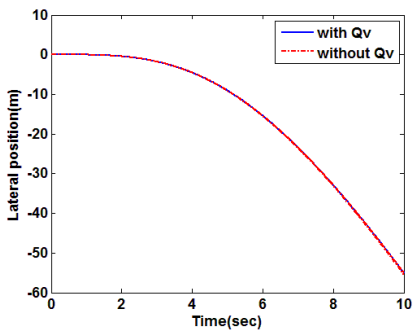

(a) Lateral position

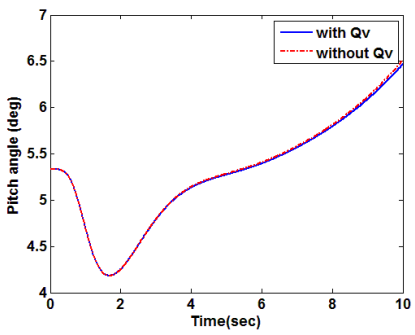

(b) Pitch angle

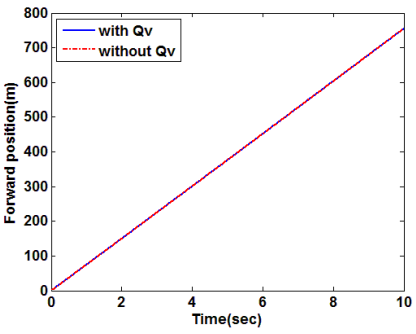

(c) Forward positon

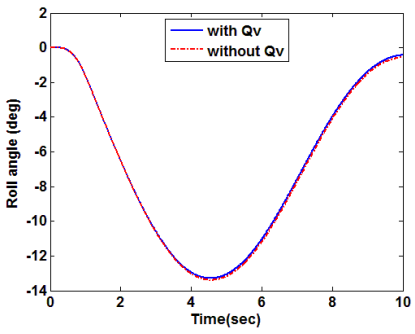

(d) Roll angle

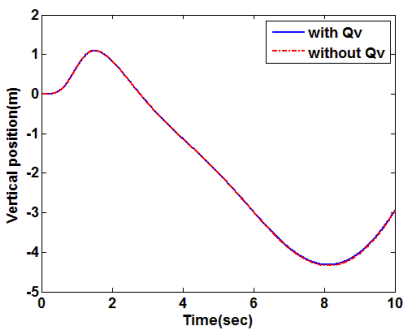

(e) Vertical position

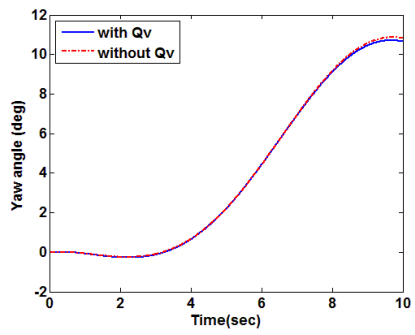

(f) Yaw angle

Figure A.3. Flight dynamic response for w/ and w/o Q_v

APPENDIX. B. FLIGHT DYNAMICS OF DAMAGED AIRCRAFT

Aircraft damage often occurs in the private sector [68, 69], especially when an aircraft is used for military purposes such as reconnaissance, attack, etc., the accident rate increases. The World War II aviation history filled with many stories of aircraft coming back home safely despite suffering major structural damage to their airframes. A flight dynamics model for a damaged aircraft is developed to account for various damage effects including changes in aerodynamics, mass, inertias, and C.G. [70-72]. When aircraft damage may cause the aircraft's center of gravity (C.G.) to shift unexpectedly. The combined loss of aerodynamic force, mass change, and C.G. shift can lead different flight dynamics from undamaged aircraft's even at trim. In this chapter, the wing tip damaged flexible aircraft flight response is compared to undamaged aircraft for trim and non-uniform gust case.

B.1. Damaged Aircraft Model Description

Typically, the aircraft is symmetric with respect to the aircraft fuselage reference line. For a damaged aircraft, the symmetry may no longer be preserved depending on the nature of the damage such as wing damage show as Fig. B.1. The damage is only R/H wing tip loss which do not affect to the control surface as Fig. B.2. Due to the wing loss, the total mass decrease about 9.4 kg which is about 0.2% as Table B.1. This leads that the C.G. is shifted away from fuselage reference line to left about 2.7cm as shown in Fig. B.3.

B.2. Trim Analysis of Damaged Aircraft

The trim analysis of damaged aircraft process is similar to the undamaged aircraft process as described chap.2.3. Otherwise, as the aircraft become asymmetric state, the aileron angle δ_a, roll angle ϕ and yaw angle ψ should be considered as parameters shown as Fig.B.4.

We defined the cost function is as same as Eq. (2.27) which rewrite

$$J_{trim} = \sum_{i=1}^{3} \left(F_i^2 + M_i^2\right), \quad \text{(at reference point)} \tag{B.1}$$

The cost function J_{trim} is minimized using six trim parameters. The trim parameter optimization problem is described below:

$$\begin{aligned} &\text{minimize} && J_{trim} \\ &\text{with respect to} && \theta,\ \phi,\ \psi,\ \delta_a,\ \delta_e,\ \delta_T \\ &\text{Subject to} && -10° \le \phi \le 10°,\ -45° \le \delta_a \le 45° \\ & && -10° \le \theta \le 10°,\ -45° \le \delta_e \le 45° \\ & && -10° \le \psi \le 10°,\quad 0 < \delta_T \le 1 \end{aligned} \tag{B.2}$$

The flight conditions are that the aircraft velocities are 70, 75 and 80 m/s and the altitude is 10,000m. The optimized trim parameters for damaged and undamaged aircraft is as shown Table B.2. As the lift decreases due to wing damage, the angle of attack increases to maintain the trim condition, and the ruddervator angle and thrust increase. Also, trim values for roll angle, yaw angle and aileron are obtained as the aircraft becomes asymmetric. Fig.B.5 shows the deformation about damaged and undamaged aircraft wing tip vertical direction. Damaged wing is deformed less than undamaged wing.

B.3. Damaged Aircraft Flight Dynamics under Discrete Gust

The aircraft damaged wing also affects the gust effect. Fig. B.6 shows the gust velocity distribution due to non-uniform gust which parameters are $H = 50,\ F_g = 0.8,\ r_0 = 12,\ n_E = 2.0,\ G_p = 10$. The gust effect is removed at R/H wing tip. The aircraft flight altitude is 10,000m and velocity is 75m/s. Control surface and thrust are maintained as trim state. Fig. B.7 and B.8 shows the trajectory and response about undamaged and damaged aircraft. The aircrafts go turn left due to the increased lift at right wing which generates roll and yaw moment. The damaged aircraft trajectory and response are different from undamaged aircraft's. And it can be estimated that the aircraft damaged region is small, the damaged aircraft stability is sufficient when the gust exist. The damaged aircraft stability can be estimated through these analysis.

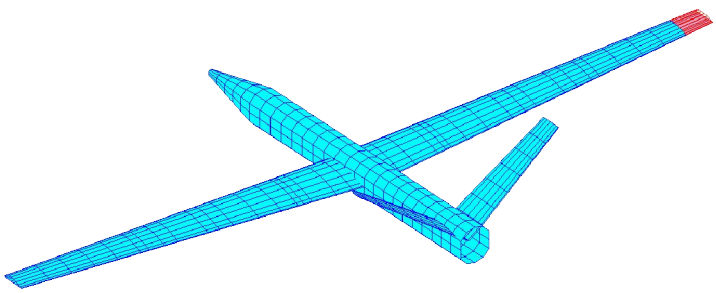

Figure B.1. Damaged aircraft model

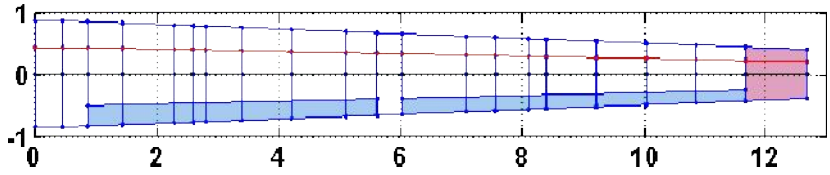

Figure B.2. R/H wing damaged region

Table B.1. Mass distribution

Aircraft	Main wing (kg)	Tail wing (kg)	Body (kg)	Total (kg)
Undamaged(A)	1442.1	217.3	3190.7	4850.1
Damaged(B)	1432.7	217.3	3190.7	4840.7
Gab (A-B)	9.4	0.0	0.0	9.4

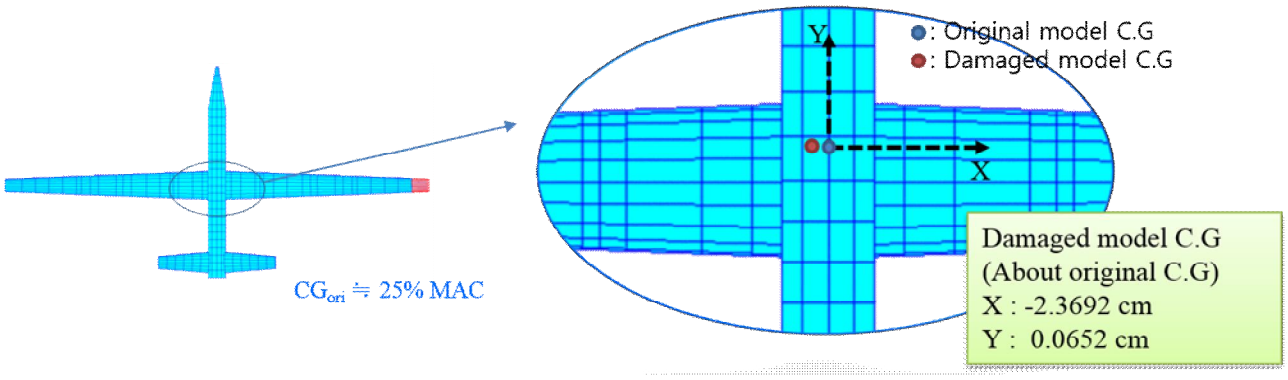

Figure B.3. Center of gravity change due to damage

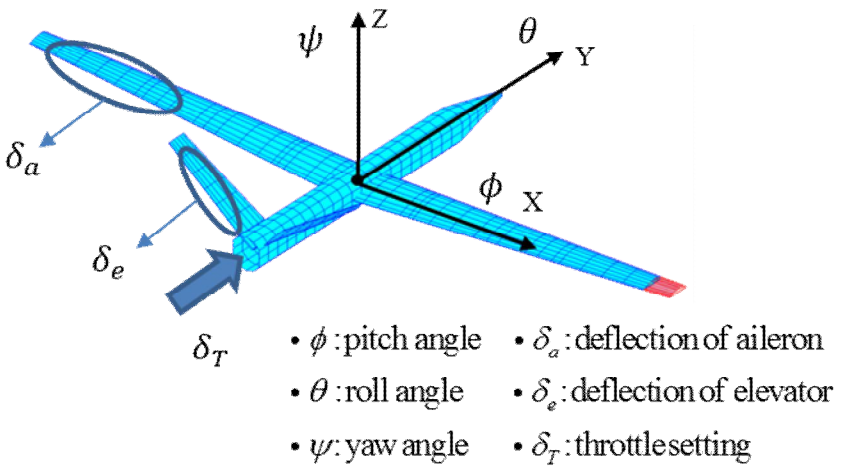

Figure B.4. Trim parameters for damaged aircraft

Table B.2. Optimized trim parameter for damaged aircraft

Parameter	Undamaged model(A)			Damaged model(B)			Gab (A-B)		
	70m/s	75m/s	80m/s	70m/s	75m/s	80m/s	70m/s	75m/s	80m/s
AOA(deg)	7.2016	5.3324	3.8050	7.3135	5.4138	3.8623	-0.1119	-0.0814	-0.0574
Roll angle(deg)	0	0	0	0.0182	0.0131	0.0093	-0.0182	-0.0131	-0.0093
Yaw angle(deg)	0	0	0	0.0226	0.0145	0.0086	-0.0226	-0.0145	-0.0086
Aileron(deg)	0	0	0	-0.0862	-0.0790	-0.0920	0.0862	0.0790	0.0920
Ruddervator(deg)	-2.4638	-1.6694	-1.0236	-2.5166	-1.7129	-1.0699	0.0528	0.0434	0.0463
Thrust(N)	6554.4	4905.0	3522.4	6650.1	4975.2	3572.7	-95.6	-70.2	-50.3

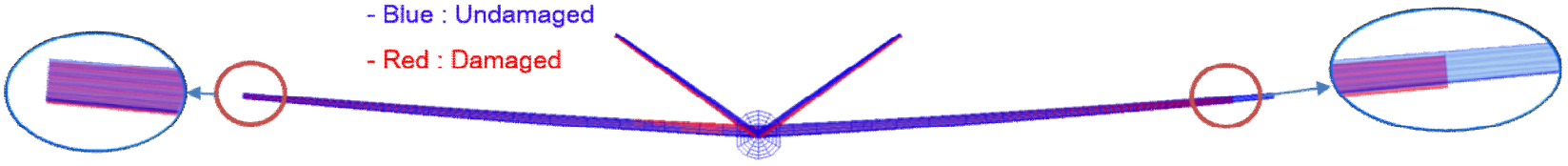

Vel.	Undemaged(A)	Damaged(B)	Gab(A-B)
70m/s	0.2625m	0.2552m	0.0074m
75m/s	0.2568m	0.2496m	0.0072m
80m/s	0.2492m	0.2421m	0.0070m

Vel.	Undemaged(C)	Damaged(D)	Gab(C-D)
70m/s	0.2264m	0.2059m	0.0205m
75m/s	0.2214m	0.2013m	0.0201m
80m/s	0.2148m	0.1952m	0.0196m

Figure B.5. Trim state about undamaged and damaged flexible aircraft

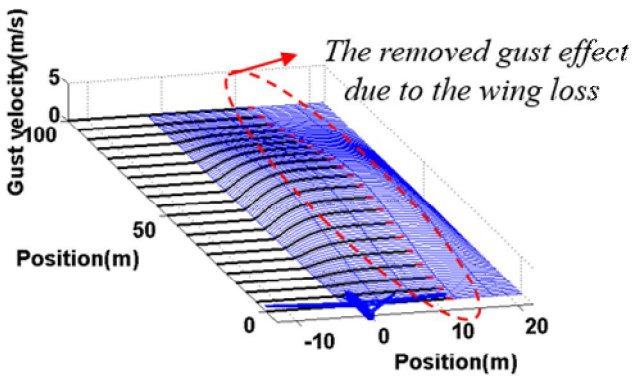

$* H = 50,\ F_g = 0.8,\ r_0 = 12,\ n_E = 2.0,\ G_p = 10$

Figure B.6. Non-uniform discrete gust distribution to damaged aircraft

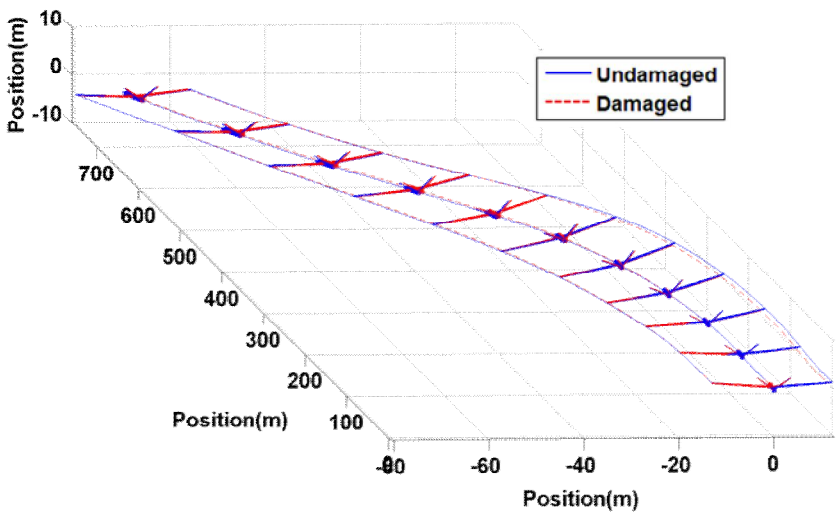

Figure B.7. Trajectory of undamaged and damaged aircraft

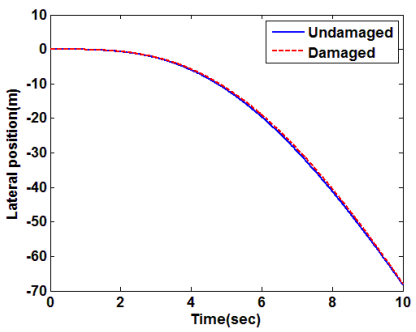

(a) Lateral position

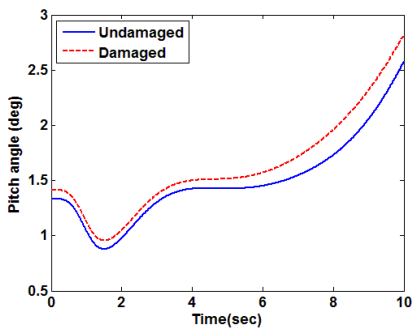

(b) Pitch angle

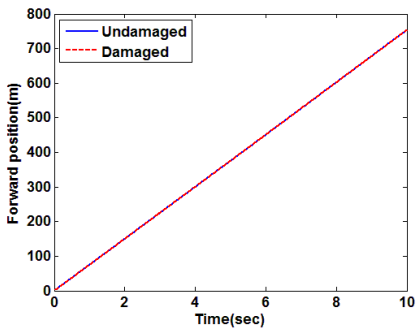

(c) Forward positon

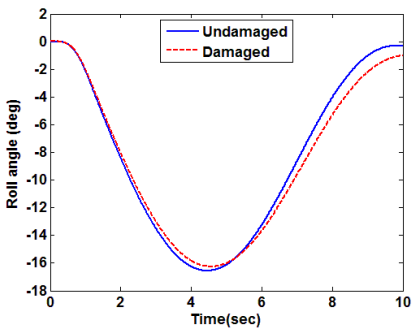

(d) Roll angle

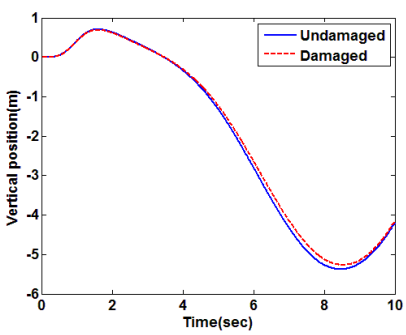

(e) Vertical position

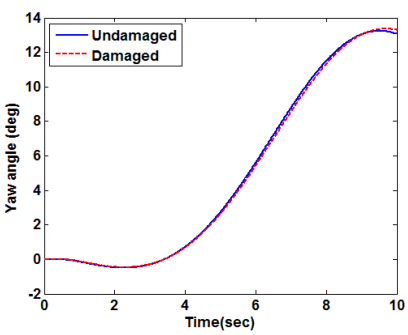

(f) Yaw angle

Figure B.8. Flight dynamic response for undamaged and damaged aircraft

APPENDIX. C. FLIGHT DYNAMICS CONSIDERING BOMB SEPARATION

If the aircraft is used for military purposes, the storage—external fuel tank, rocket, missile, etc.—might be loaded. There are many researches about the ejected store trajectory from the aircraft through numerical simulation and/or experimental test [73-77]. These researches are interesting the store not the dynamic load for aircraft due to the ejection.

Structural design loads, otherwise, in dynamic response to concentrated excitation forces such as in landing and store-ejection impacts are calculated by the mode-displacements (MD), the modal acceleration method (MA) or the summation-of-forces (SOF) approach. In cases of time response to local impulsive excitation, such as store ejection or landing, the MD and MA method performs inaccurate than SOF [78, 79]. The main reason is that concentrated forces cause local deformations that are not represented in the low-frequency vibration modes. The SOF method is less sensitive to local response effects, but is more difficult to apply, especially when time-domain unsteady aerodynamic effects are involved.

In this chapter, the aircraft's center of gravity (C.G) change is observed. The dynamic loads and structure response are conducted considering bomb separation for symmetric drop and asymmetric drop cases in time-domain.

C.1. Aircraft with Bomb Loading Model Description

Typically, the aircraft is symmetric with respect to the aircraft fuselage reference

line and bombs are loaded symmetrically. In this research, bomb is modeled using GBU-12 which is one of the most used weapon. This bomb mass is about 230kg and loading at near wing root. The symmetric and asymmetric bomb loading case is modeled as fig.C.1. Due to the bomb mass, the center of gravity and mass are changed as fig. C.2 and fig C.3. As two bombs are loaded at each side, the C.G is moved forward about 2.9cm. The total mass is increased 460kg which is about 9.48% for without bomb aircraft mass. And one bomb is loaded at L/H, the C.G is shifted forward about 1.52cm and shifted away from fuselage reference line to left about 10.42cm. The total mass is increased 230kg which is about 4.74%.

In this study, trim analysis is conducted for the symmetric loading case. Two cases of bomb separation are simulated. First, the both bomb is ejected at same time. Second, only the R/H bomb is separated. The trim analysis and bomb separation simulation results is presented following section. The loading bomb state affects not only the mass and C.G. but also aerodynamics, for example, vortex, parasitic drag, etc. In this study, the aerodynamics change due to the bomb loading is no considered.

C.2. Trim Analysis considering Symmetric Bomb Loading

The trim analysis considering symmetric bomb loading aircraft is same as described chap.2.3. Because only total aircraft mass is changed and the C.G exists the aircraft fuselage reference line. We defined the cost function is as same as Eqn.(2.27) which rewrite

$$J_{trim} = \sum_{i=1}^{3} \left(F_i^2 + M_i^2 \right), \quad \text{(at reference point)} \tag{C.1}$$

The cost function J_{trim} is minimized using three trim parameters. The trim parameter optimization problem is described below:

$$\begin{aligned} &\text{minimize} && J_{trim} \\ &\text{with respect to} && \delta_e,\ \delta_T,\ \phi \\ &\text{subject to} && -45° \le \delta_e \le 45° \\ & && 0 \le \delta_T \le 1 \\ & && -30° \le \phi \le 30° \end{aligned} \tag{C.2}$$

The flight conditions are that the aircraft velocities are 70, 75 and 80 m/s and the altitude is 10,000m. The optimized trim parameters for without bomb and symmetric bomb loading cases are as shown Table C.1. As the total mass is increased due to bombs, the more lift and thrust are need. So, the angle of attack, the ruddervator angle and thrust are increase than no bomb case. Fig.C.4 shows the deformation of wing tip vertical direction. Bomb loaded wing is more deformed than no bomb case.

C.3. Flight Dynamics considering Bomb Separation

As bomb separation, the aircraft total mass and C.G are changed suddenly. First, the both bombs are separation case is conducted. There is no ejection force only separation. The aircraft damaged wing also affects the gust effect. The aircraft flight altitude is 10,000m and velocity is 75m/s. Control surface and thrust are maintained as symmetric bomb loading trim state. The bombs are separated at one second. Fig. C.5 and C.6 shows the trajectory and flight dynamic response. As both bombs are separated, the aircraft arise due to the mass decrease. The load factor is increased about 8% as the lift is maintained and the weight is decreased. The R/H wing root bending moment is increased as the load factor is increased. The wing

deformation is decreased.

Fig. C.7 and C.8 shows the trajectory and response about only R/H bomb separation case. The aircraft goes turn left due to the decreased R/H weight which generates roll and yaw moment. The pitch, roll and yaw angles are change due to the asymmetric aircraft mass, force condition and mass loss. The load factor is increased about 4%. The wing root bending moment and wing tip displacement are changed. The aircraft flight dynamic response can be estimated through these analysis.

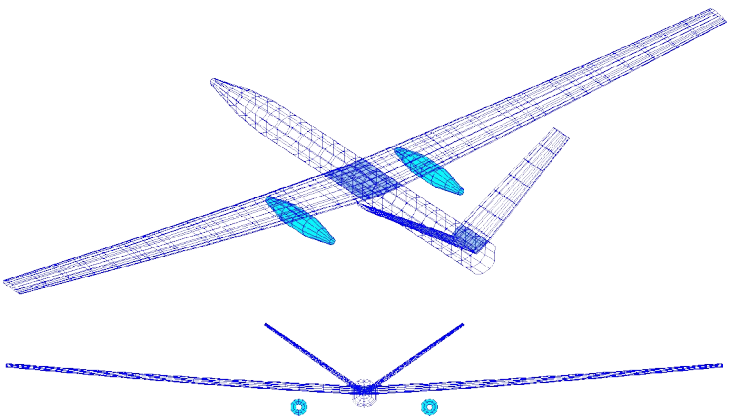

(a) Symmetric bomb loading

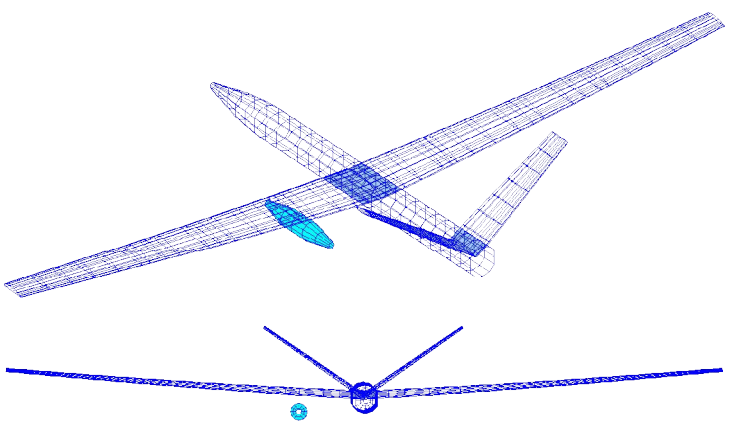

(b) Asymmetric bomb loading

Figure C.1. Bomb loading model

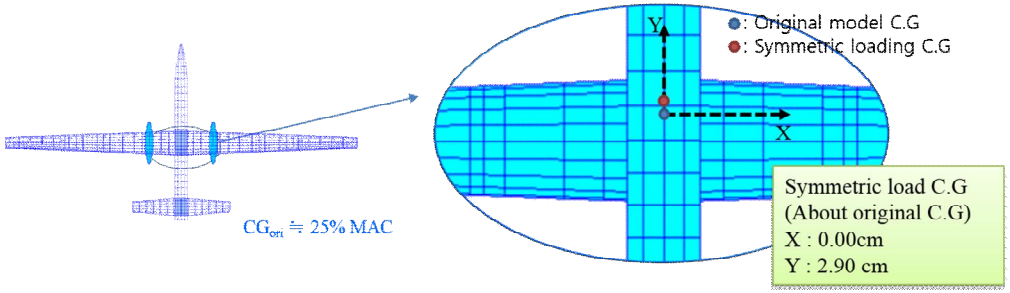

(a) C.G. change for symmetric bomb loading

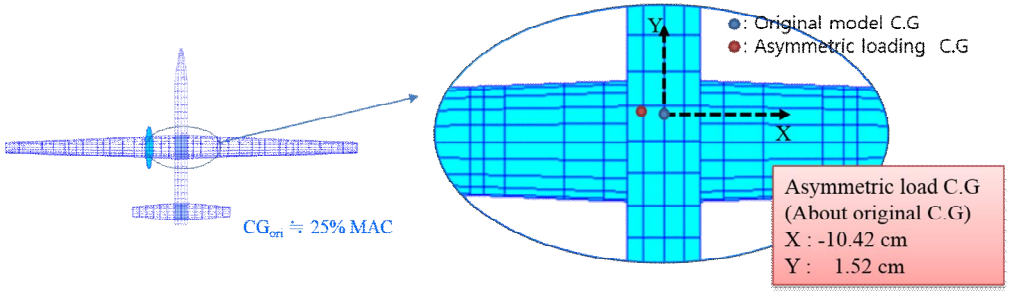

(b) C.G. change for asymmetric bomb loading

Figure C.2. Center of gravity change due to bomb loading

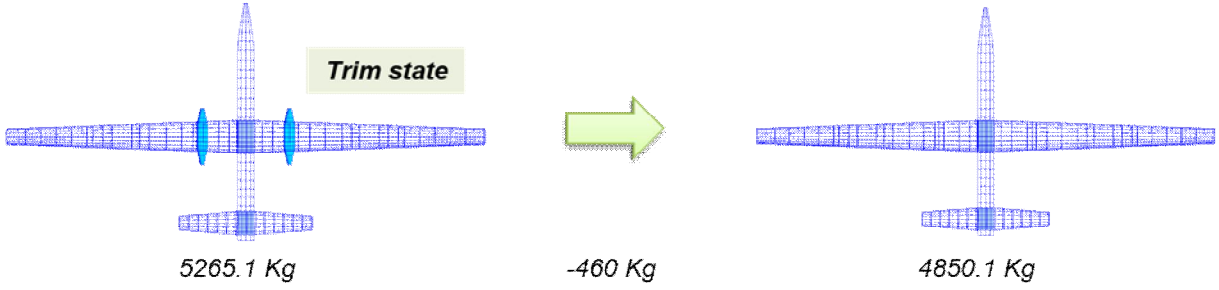

(a) Mass change for symmetric bomb loading

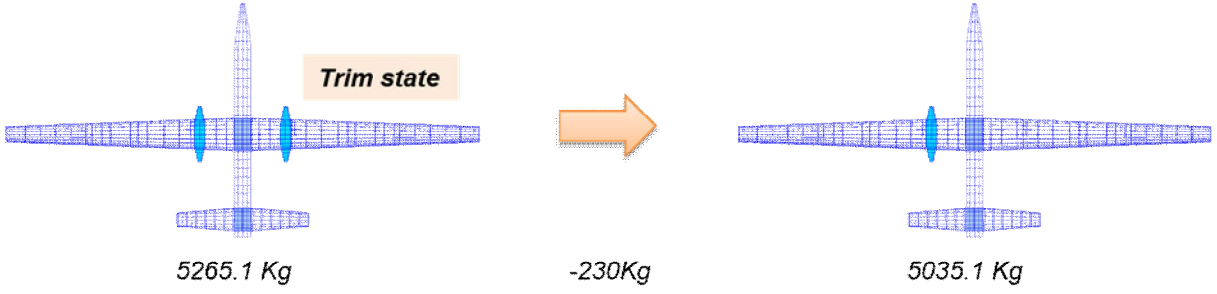

(b) Mass change for asymmetric bomb loading

Figure C.3. Mass change due to bomb loading

Table C.1. Optimized trim parameter (no bomb vs. symmetric bomb loading)

Parameter	No bomb model(A)			Bomb loading model(B)			Gab (A-B)		
	70m/s	75m/s	80m/s	70m/s	75m/s	80m/s	70m/s	75m/s	80m/s
AOA(deg)	7.2016	5.3324	3.8050	7.8737	5.8263	4.1599	-0.6721	-0.4939	-0.3549
Ruddervator(deg)	-2.4638	-1.6694	-1.0236	-2.7836	-1.9207	-1.2865	0.3197	0.2512	0.2629
Thrust(N)	6554.4	4905.0	3522.4	7782.3	5810.3	4173.2	-1227.9	-905.3	-650.8

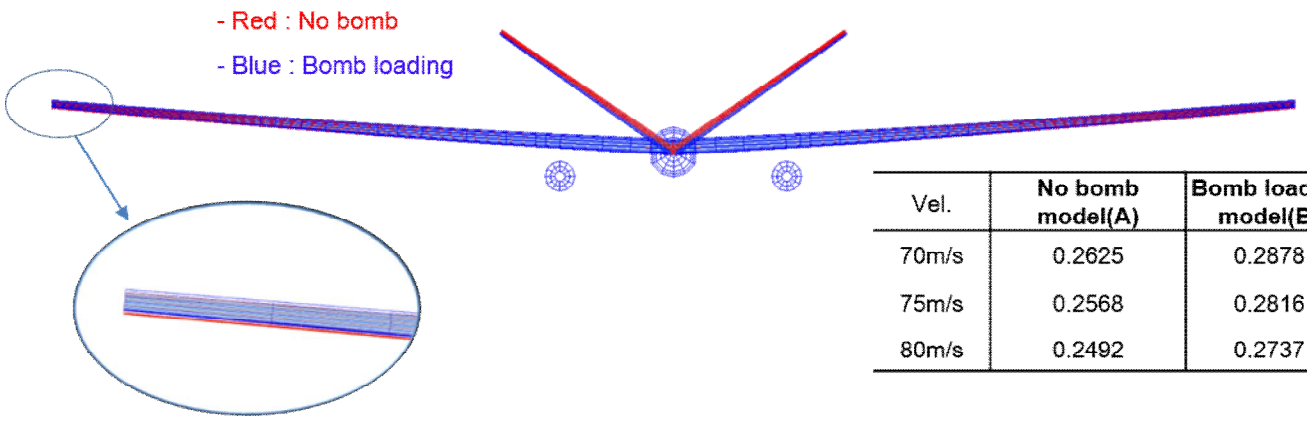

Vel.	No bomb model(A)	Bomb loading model(B)	Gab(A-B)
70m/s	0.2625	0.2878	-0.0253
75m/s	0.2568	0.2816	-0.0248
80m/s	0.2492	0.2737	-0.0245

Figure C.4. Trim state about symmetric bomb loading case

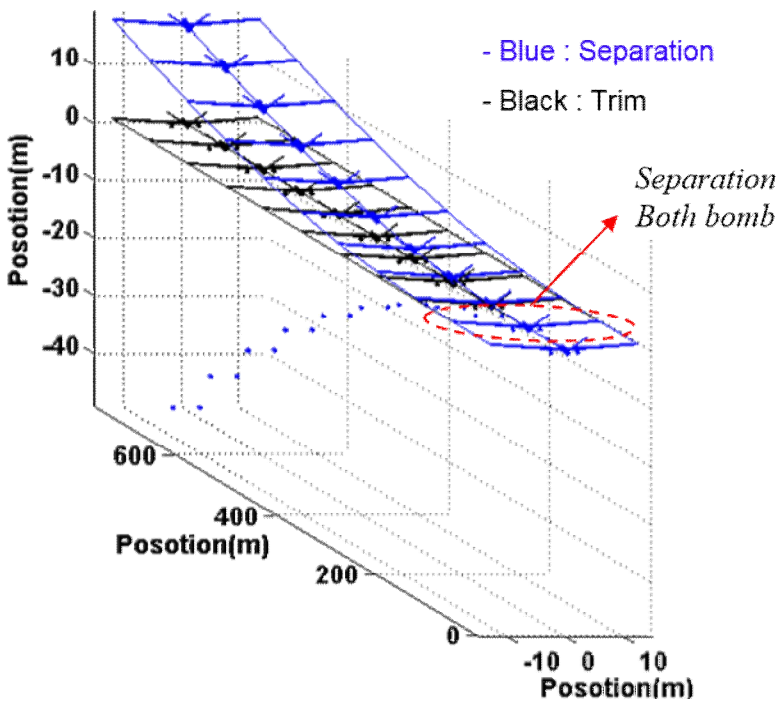

Figure C.5. Trajectory for both bomb ejection

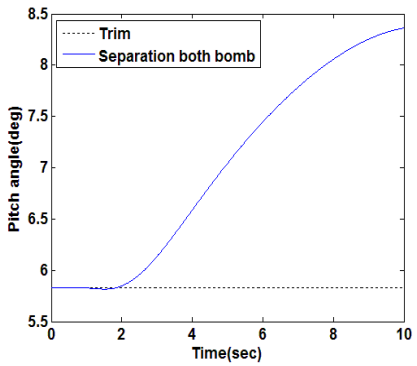

(a) Pitch angle

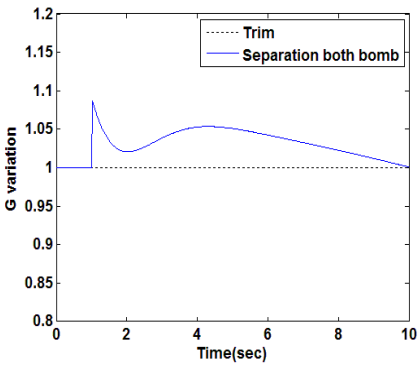

(b) Load factor varication

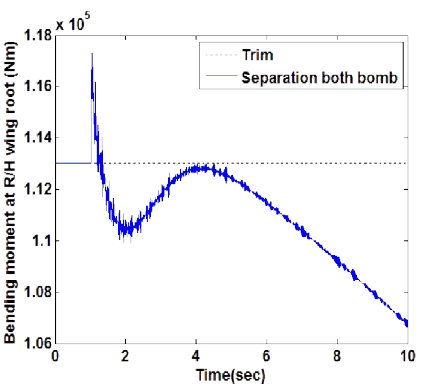

(e) Bending moment at R/H wing root

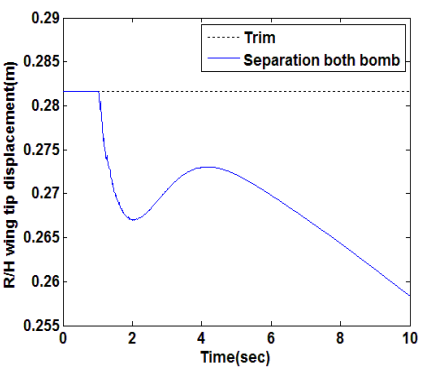

(f) R/H Wing tip displacement

Figure C.6. Flight dynamic response for both bomb ejection

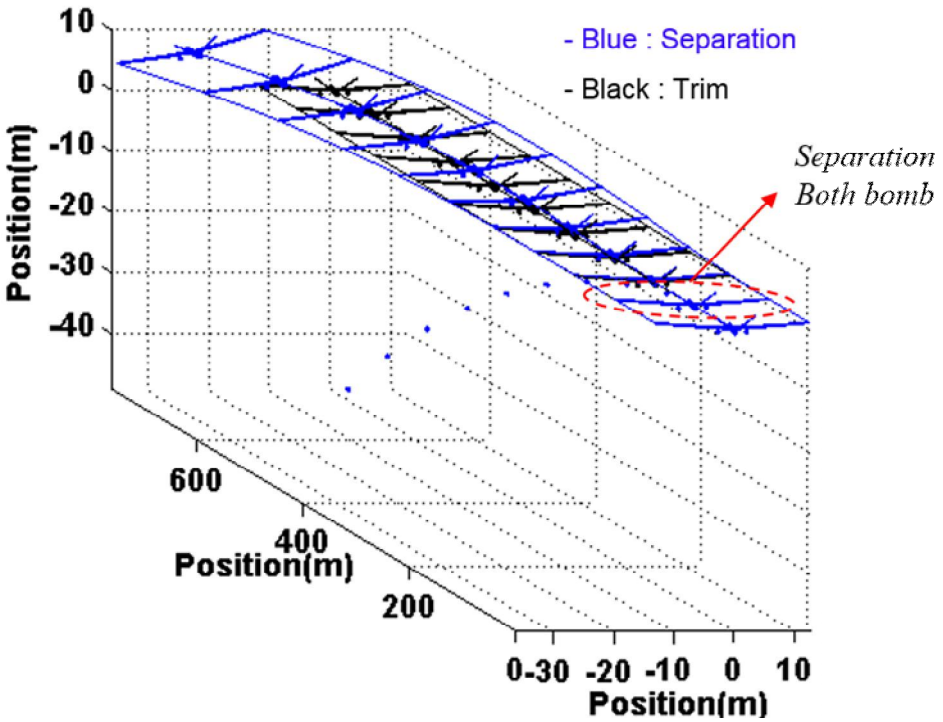

Figure C.7. Trajectory for R/H bomb ejection

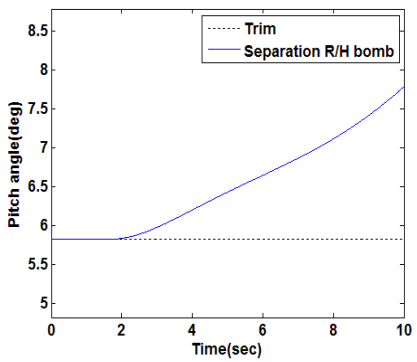

(a) Pitch angle

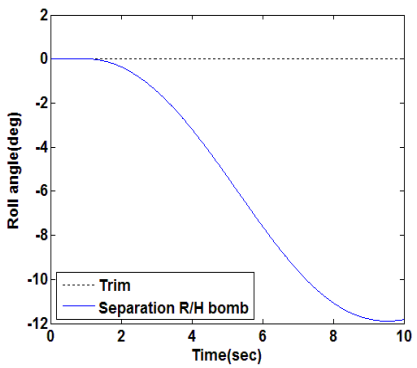

(b) Roll angle

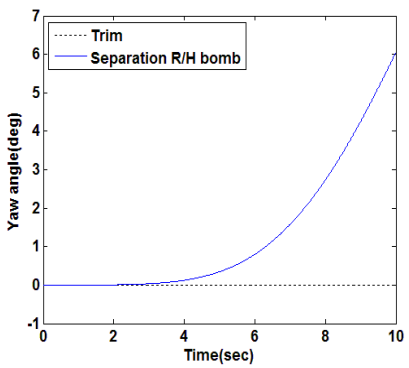

(c) Yaw angle

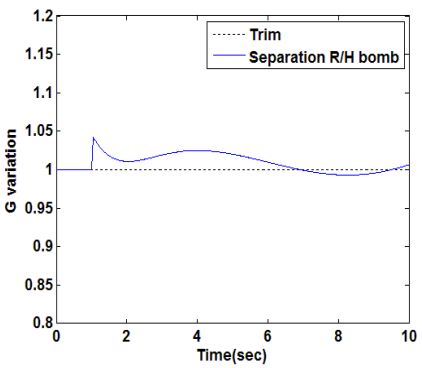

(d) Load factor varication

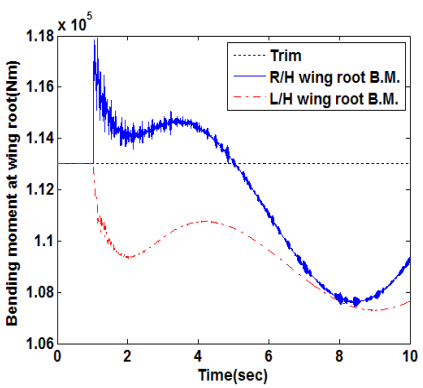

(e) Bending moment at main wing root

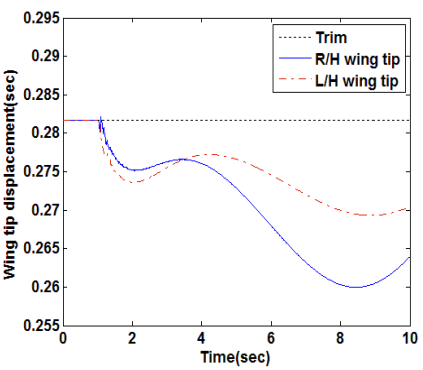

(f) Wing tip displacement

Figure C.8. Flight dynamic response for R/H bomb ejection

REFERENCE

[1] M. Dillsaver, C. Cesnik, and I. Kolmanovsky, "Gust response sensitivity characteristics of very flexible aircraft," in *AIAA Atmospheric Flight Mechanics Conference, AIAA*, 2012.

[2] H. MØller, E. Lund, J. A. Ambrósio, and J. GonÇalves, "Simulation of fluid loaded flexible multibody systems," *Multibody System Dynamics,* vol. 13, pp. 113-128, 2005.

[3] J.-C. Samin, O. Brüls, J.-F. Collard, L. Sass, and P. Fisette, "Multiphysics modeling and optimization of mechatronic multibody systems," *Multibody System Dynamics,* vol. 18, pp. 345-373, 2007.

[4] Z. Zhao and G. Ren, "Multibody dynamic approach of flight dynamics and nonlinear aeroelasticity of flexible aircraft," *AIAA journal,* vol. 49, pp. 41-54, 2011.

[5] M. Castellani, J. E. Cooper, and Y. Lemmens, "Nonlinear Static Aeroelasticity of High Aspect Ratio Wing Aircraft by FEM and Multibody Methods," in *15th Dynamics Specialists Conference*, 2016, p. 1573.

[6] M. Drela, "Integrated simulation model for preliminary aerodynamic, structural, and control-law design of aircraft," *AIAA Paper,* vol. 99, p. 1394, 1999.

[7] C. E. Cesnik and E. L. Brown, "Modeling of high aspect ratio active flexible wings for roll control," in *Proceedings of the 43rd AIAA/ASME/ASCE/AHS Structures, Structural Dynamics, and Materials Conferences, Denver, Colorado*, 2002, pp. 2002-1719.

[8] C. E. Cesnik and E. L. Brown, "Active warping control of a joined-wing airplane configuration," in *Proceedings of the 44th AIAA/ASME/ASCE/AHS/ASC Structures, Structural Dynamics, and Material Conference, Hampton, Virginia*, 2003.

[9] E. L. Brown, "Integrated strain actuation in aircraft with highly flexible composite wings," Massachusetts Institute of Technology, 2003.

[10] D. A. Peters, S. Karunamoorthy, and W.-M. Cao, "Finite state induced flow models. I-Two-dimensional thin airfoil," *Journal of Aircraft,* vol. 32, pp. 313-322, 1995.

[11] C. M. Shearer, "Coupled nonlinear flight dynamics, aeroelasticity, and control of very flexible aircraft," 2006.

[12] C. M. Shearer and C. E. Cesnik, "Nonlinear flight dynamics of very flexible aircraft," *Journal of Aircraft,* vol. 44, pp. 1528-1545, 2007.

[13] C. M. Shearer and C. E. S. Cesnik, "Trajectory control for very flexible aircraft," *Journal of Guidance, Control, and Dynamics,* vol. 31, pp. 340-357, 2008.

[14] W. Su and C. E. S. Cesnik, "Dynamic Response of Highly Flexible Flying Wings," *AIAA Journal,* vol. 49, pp. 324-339, 2011.

[15] M. J. Patil and D. H. Hodges, "Flight dynamics of highly flexible flying wings," *Journal of Aircraft,* vol. 43, pp. 1790-1799, 2006.

[16] D. H. Hodges, "A mixed variational formulation based on exact intrinsic equations for dynamics of moving beams," *International journal of solids and structures,* vol. 26, pp. 1253-1273, 1990.

[17] D. H. Hodges, "Geometrically exact, intrinsic theory for dynamics of curved and twisted anisotropic beams," *AIAA journal,* vol. 41, pp. 1131-1137, 2003.

[18] J. Pedro and C. G. Bigg, "Development of a flexible embedded aircraft/Control system simulation facility," in *Proceedings of the AIAA Modeling and Simulation Technologies, Conference and Exhibit, San Francisco, CA, USA*, 2005, pp. 1-25.

[19] A. A. Shabana, "Flexible multibody dynamics: review of past and recent developments," *Multibody system dynamics,* vol. 1, pp. 189-222, 1997.

[20] R. Rossi, M. Lazzari, and R. Vitaliani, "Wind field simulation for structural engineering purposes," *International journal for numerical methods in engineering,* vol. 61, pp. 738-763, 2004.

[21] C. Casarotti and R. Pinho, "An adaptive capacity spectrum method for assessment of bridges subjected to earthquake action," *Bulletin of Earthquake Engineering,* vol. 5, pp. 377-390, 2007.

[22] L. Sun and F. Luo, "Arrays of dynamic circular loads moving on an infinite plate," *International journal for numerical methods in engineering,* vol. 71, pp. 652-677, 2007.

[23] P. Lou, "Vertical dynamic responses of a simply supported bridge subjected to a moving train with two-wheelset vehicles using modal analysis method," *International Journal for Numerical Methods in Engineering,* vol. 64, pp. 1207-1235, 2005.

[24] H. Inoue, J. J. Harrigan, and S. R. Reid, "Review of inverse analysis for indirect measurement of impact force," *Applied Mechanics Reviews,* vol. 54, pp. 503-524, 2001.

[25] X. Xu and J. Ou, "Force identification of dynamic systems using virtual work principle," *Journal of Sound and Vibration,* vol. 337, pp. 71-94, 2015.

[26] Y. W. Yang, C. Wang, and C. K. Soh, "Force identification of dynamic systems using genetic programming," *International journal for numerical methods in engineering,* vol. 63, pp. 1288-1312, 2005.

[27] D. C. Kammer, "Input force reconstruction using a time domain technique," *Journal of vibration and acoustics,* vol. 120, pp. 868-874, 1998.

[28] C.-H. Huang, "An inverse non-linear force vibration problem of estimating the external forces in a damped system with time-dependent system parameters," *Journal of sound and vibration,* vol. 242, pp. 749-765, 2001.

[29] C.-K. Ma and C.-C. Ho, "An inverse method for the estimation of input forces acting on non-linear structural systems," *Journal of Sound and Vibration,* vol. 275, pp. 953-971, 2004.

[30] X. Cao, Y. Sugiyama, and Y. Mitsui, "Application of artificial neural networks to load identification," *Computers & structures,* vol. 69, pp. 63-78, 1998.

[31] C. Coates, P. Thamburaj, and C. Kim, "An inverse method for selection of Fourier coefficients for flight load identification," in *46th AIAA/ASME/ASCE/AHS/ASC Structures, Structural Dynamics and Materials Conference*, 2005, p. 2183.

[32] C. W. Coates and P. Thamburaj, "Inverse method using finite strain measurements to determine flight load distribution functions," *Journal of*

Aircraft, vol. 45, pp. 366-370, 2008.

[33] T. Nakamura, H. Igawa, and A. Kanda, "Inverse identification of continuously distributed loads using strain data," *Aerospace Science and Technology,* vol. 23, pp. 75-84, 2012.

[34] F. M. Hoblit, *Gust loads on aircraft: concepts and applications*: Aiaa, 1988.

[35] A. Tarantola, *Inverse problem theory and methods for model parameter estimation*: siam, 2005.

[36] D. W. Patterson, *Artificial neural networks: theory and applications*: Prentice Hall PTR, 1998.

[37] J. Kudva, N. Munir, and P. Tan, "Damage detection in smart structures using neural networks and finite-element analyses," *Smart Materials and Structures,* vol. 1, p. 108, 1992.

[38] Y. Ni, B. Wang, and J. Ko, "Constructing input vectors to neural networks for structural damage identification," *Smart Materials and Structures,* vol. 11, p. 825, 2002.

[39] Y. Lu, L. Ye, Z. Su, L. Zhou, and L. Cheng, "Artificial neural network (ANN)-based crack identification in aluminum plates with Lamb wave signals," *Journal of Intelligent Material Systems and Structures,* vol. 20, pp. 39-49, 2009.

[40] N. V. Queipo, R. T. Haftka, W. Shyy, T. Goel, R. Vaidyanathan, and P. K. Tucker, "Surrogate-based analysis and optimization," *Progress in aerospace sciences,* vol. 41, pp. 1-28, 2005.

[41] A. I. Forrester and A. J. Keane, "Recent advances in surrogate-based optimization," *Progress in Aerospace Sciences,* vol. 45, pp. 50-79, 2009.

[42] R. Hambli, A. Chamekh, and H. B. H. Salah, "Real-time deformation of structure using finite element and neural networks in virtual reality applications," *Finite elements in analysis and design,* vol. 42, pp. 985-991, 2006.

[43] R. Pidaparti, S. Jayanti, and M. Palakal, "Residual strength and corrosion rate predictions of aging aircraft panels: neural network study," *Journal of aircraft,* vol. 39, pp. 175-180, 2002.

[44] A. D. Spear, A. R. Priest, M. G. Veilleux, A. R. Ingraffea, and J. D.

Hochhalter, "Surrogate modeling of high-fidelity fracture simulations for real-time residual strength predictions," *AIAA journal,* vol. 49, pp. 2770-2782, 2011.

[45] M. L. Steinberg, "Comparison of intelligent, adaptive, and nonlinear flight control laws," *Journal of Guidance, Control, and Dynamics,* vol. 24, pp. 693-699, 2001.

[46] R. Rysdyk and A. Calise, "Fault tolerant flight control via adaptive neural network augmentation," in *Guidance, Navigation, and Control Conference and Exhibit*, 1998, p. 4483.

[47] B. S. Kim and A. J. Calise, "Nonlinear flight control using neural networks," *Journal of Guidance, Control, and Dynamics,* vol. 20, pp. 26-33, 1997.

[48] V. Singh and K. E. Willcox, "Methodology for Path Planning with Dynamic Data-Driven Flight Capability Estimation," in *17th AIAA/ISSMO Multidisciplinary Analysis and Optimization Conference*, 2016, p. 4124.

[49] W. Yu, "VABS Manual for Users, March 2011," ed, 2013.

[50] W. Yu, V. V. Volovoi, D. H. Hodges, and X. Hong, "Validation of the variational asymptotic beam sectional analysis," *AIAA journal,* vol. 40, pp. 2105-2112, 2002.

[51] I. Ixx, "Various structural approaches to analyze an aircraft with high aspect ratio wings," 2012.

[52] F. A. R. Part, "25: Airworthiness standards: Transport category airplanes," *Federal Aviation Administration, Washington, DC,* vol. 7, 2002.

[53] A. De Marco, E. L. Duke, and J. S. Berndt, "A general solution to the aircraft trim problem," in *AIAA Modeling and Simulation Technologies Conference and Exhibit*, 2007, p. 6703.

[54] J. R. Martins and A. B. Lambe, "Multidisciplinary design optimization: a survey of architectures," *AIAA journal,* vol. 51, pp. 2049-2075, 2013.

[55] K. G. Pratt and W. G. Walker, "A revised gust-load formula and a re-evaluation of VG data taken on civil transport airplanes from 1933 to 1950," 1954.

[56] J. Fuller and J. Fuller, "Evolution and future development of airplane gust

loads design requirements," in *1997 World Aviation Congress*, 1997, p. 5577.

[57] A. Ricciardi, M. Patil, R. Canfield, and N. Lindsley, "Utility of quasi-static gust loads certification methods for novel configurations," in *52nd AIAA/ASME/ASCE/AHS/ASC Structures, Structural Dynamics and Materials Conference 19th AIAA/ASME/AHS Adaptive Structures Conference 13t*, 2011, p. 2043.

[58] A. P. Ricciardi, M. J. Patil, R. A. Canfield, and N. Lindsley, "Evaluation of Quasi-Static Gust Loads Certification Methods for High-Altitude Long-Endurance Aircraft," *Journal of Aircraft,* vol. 50, pp. 457-468, 2013.

[59] A. A. Shabana, *Dynamics of multibody systems*: Cambridge university press, 2013.

[60] M. C. Bampton and J. CRAIG, Roy R, "Coupling of substructures for dynamic analyses," *Aiaa Journal,* vol. 6, pp. 1313-1319, 1968.

[61] P. Holzwarth and P. Eberhard, "SVD-based improvements for component mode synthesis in elastic multibody systems," *European Journal of Mechanics-A/Solids,* vol. 49, pp. 408-418, 2015.

[62] C. Nowakowski, J. Fehr, M. Fischer, and P. Eberhard, "Model order reduction in elastic multibody systems using the floating frame of reference formulation," *IFAC Proceedings Volumes,* vol. 45, pp. 40-48, 2012.

[63] A. C. Antoulas, *Approximation of large-scale dynamical systems*: SIAM, 2005.

[64] Y. Liang, H. Lee, S. Lim, W. Lin, K. Lee, and C. Wu, "Proper orthogonal decomposition and its applications—Part I: Theory," *Journal of Sound and vibration,* vol. 252, pp. 527-544, 2002.

[65] H. B. Demuth, M. H. Beale, O. De Jess, and M. T. Hagan, *Neural network design*: Martin Hagan, 2014.

[66] H. Demuth and M. Beale, "Matlab neural network toolbox user's guide version 6. The MathWorks Inc," 2009.

[67] M. T. Hagan and M. B. Menhaj, "Training feedforward networks with the Marquardt algorithm," *IEEE transactions on Neural Networks,* vol. 5, pp.

989-993, 1994.

[68] D. Hughes and M. A. Dornheim, "DHL/EAT crew lands A300 with no hydraulics after being hit by missile," *Aviation Week & Space Technology,* vol. 8, 2003.

[69] D. Tran and E. Hernandez, "Use of the vertical motion simulator in support of the american airlines flight 587 accident investigation," in *AIAA Modeling and Simulation Technologies Conference and Exhibit*, 2004, p. 5032.

[70] N. Nguyen, K. Krishnakumar, J. Kaneshige, and P. Nespeca, "Dynamics and adaptive control for stability recovery of damaged asymmetric aircraft," in *AIAA Guidance, Navigation, and Control Conference and Exhibit*, 2006, p. 6049.

[71] N. T. Nguyen, K. S. Krishnakumar, J. T. Kaneshige, and P. P. Nespeca, "Flight dynamics and hybrid adaptive control of damaged aircraft," *Journal of guidance, control, and dynamics,* vol. 31, pp. 751-764, 2008.

[72] G. Shah, "Aerodynamic effects and modeling of damage to transport aircraft," in *AIAA Atmospheric Flight Mechanics Conference and Exhibit*, 2008, p. 6203.

[73] L. E. Lijewski and N. E. Suhs, "Time-accurate computational fluid dynamics approach to transonic store separation trajectory prediction," *Journal of Aircraft,* vol. 31, pp. 886-891, 1994.

[74] R. Hua, C. Zhao, Z. Ye, and Y. Jiang, "Effect of elastic deformation on the trajectory of aerial separation," *Aerospace Science and Technology,* vol. 45, pp. 128-139, 2015.

[75] F. J. Wilcox Jr, "Experimental measurements of internal store separation characteristics at supersonic speeds," 1990.

[76] L. Formaggia, J. Peraire, and K. Morgan, "Simulation of a store separation using the finite element method," *Applied Mathematical Modelling,* vol. 12, pp. 175-181, 1988.

[77] R. F. Tomaro, F. C. Witzeman, and W. Z. Strang, "Simulation Of Store Separation For The F/A-18c Using Cobalt," *Journal of Aircraft,* vol. 37, pp. 361-367, 2000.

[78] M. Karpel and E. Presente, "Structural dynamic loads in response to impulsive excitation," *Journal of Aircraft,* vol. 32, pp. 853-861, 1995.

[79] M. Karpel and D. Raveh, "Fictitious mass element in structural dynamics," *AIAA journal,* vol. 34, pp. 607-613, 1996.

국문요약

항공기는 그 임무 목적에 따라 다양한 형태로 설계/제작되는데 장기체공 항공기의 경우 공력 효율을 증가시키기 위하여 가로세로비(aspect ratio)가 큰 날개를 장착한다. 가로세로비가 큰 날개는 비행 중 변형이 발생하며, 이러한 형상변형으로 인해 공력이 변하게 되고, 이러한 공력은 다시 구조 변형을 일으키게 된다.

이러한 유연항공기에 대한 비행동역학 해석을 위해서는 항공기 구조-비행역학-공력의 연계가 필요하다. 또한, 가로세로비가 큰 날개로 인해 비행 중 발생 가능한 돌풍에 대한 영향을 크게 받게 되므로 이를 고려하여야 한다. 본 연구는 구조-비행역학-공력을 연계하기 위하여 다물체 동역학 해석기법인 FFRF (floating frame of reference formulation)와 유한상태변수 동적유입류(finite state inflow theory)를 연계하여 유연항공기 6 자유도 비행동역학 해석 기법을 제안하였다. 또한 돌풍의 영향을 확인하기 위해 공력모델에 1-cosine 돌풍모델을 반영하였으며, 조종면을 고려한 기동해석을 수행하였다.

이러한 해석기법을 기반으로 유연항공기의 트림해석을 위해 트림변수 최적화 기법을 고안하였으며, 유연항공기의 임계돌풍을 산출하여 미연방항공규정(Federal Aviation Regulations)에 정의되어있는 준 정적 돌풍해석기법과의 비교하였다. 또한, 이용 가능한 제한된 비행시험 데이터를 이용하여 하중 재구성기법을 제안하였다. 비행 중 발생하는 예측 불가능한 돌

풍은 역 문제 이론(inverse problem theory)에 기초하여 식별하였으며, 식별된 돌풍을 통해 비행 하중을 재구성 하였다.

다양한 비행조건 및 상태를 반영한 해석을 위해서는 많은 해석이 수행되어야 하는데 이러한 계산효율을 증대시키기 위해 적합 직교 분해 방법(POD; Proper Orthogonal Decomposition)에 기반한 축소 된 차수의 모델을 구성하였다. 이 축소 모델의 효율을 향상시키기 위해 항공기 응답 및 돌풍 속도를 통해 하중을 산출하도록 인공 신경망(Artificial neural network)을 통한 대리모델(surrogate model)을 구성하였다.

제안된 유연항공기 6 자유도 비행동역학 해석기법은 기동, 돌풍, 손상 및 무장투하 등 다양한 비행조건 및 항공기 상태를 반영하여 항공기 안정성 및 구조안전성, 항공기 비행특성 변화 분석 등 활용할 수 있을 것으로 판단되며, 본 해석기법을 통해 유연한 항공기 개발, 유지, 평가에 실제적으로 활용할 수 있을 것으로 기대된다.

주요어: 유연항공기, 돌풍, 유연 다물체 동역학, 축소모델, 뉴럴네트워크

학번: 2014-31035